Dissertation zur Erlangung des Doktorgrades
der Fakultät für Chemie und Pharmazie
der Ludwig-Maximilians-Universität München

Peptide nucleic acid – zirconium coordination nanoparticles

Özgür Öztürk

aus

Tarsus, Türkiye

2022

Erklärung

Diese Dissertation wurde im Sinne von § 7 der Promotionsordnung vom 28. November 2011 von Herrn Prof. Dr. Ernst Wagner betreut.

Eidesstattliche Versicherung

Diese Dissertation wurde eigenständig und ohne unerlaubte Hilfe erarbeitet.

München, 31.10.2022

……………………………………

Özgür Öztürk

Dissertation eingereicht am: 17.11.2022

1. Gutachter: Prof. Dr. Ernst Wagner
2. Gutachter: Ass.-Prof. Dr. Ulrich Lächelt

Mündliche Prüfung am: 21.12.2022

To My Family

Aileme

Table of Contents

1. Introduction

This chapter is a brief introduction into the concept of coordination polymers and peptide nucleic acids to put the experimental data of the following chapters into a broader context. It is not a complete review of the whole scientific area.

1.1 Metal-organic frameworks in a biological context

Metal organic frameworks (MOFs) are inorganic/organic hybrid materials composed of metal ions or metal clusters and organic linkers with Lewis base functions [1]. Coordination driven self-assembly of the organic linkers and metal nodes leads to the creation of highly ordered, in many cases porous, two or three dimensional frameworks which spatial structure highly depends on metal ion and linker (Figure 1) [1-3]. Although MOFs are overwhelmingly crystalline structures, non-crystalline MOFs such as amorphous MOFs, MOF liquids, MOF glasses and other coordination polymers are reported in the literature [4]. Different linkers hosting wide range of functional motives such as carboxylates, amino acids, imidazolates, sulfonates and phenolates have been used for generating MOFs [5-9]. Similarly large number of metals such as zirconium, copper, chromium, iron, zinc, cadmium, gadolinium, and hafnium also used for MOF construction [7, 8, 10-15]. The versatile assembly strategy enables the creation of hybrid materials with a variety of features by selecting suitable building units [16]. It is also worth mentioning that multiple approaches have been developed to control size of the MOFs which is a crucial attribute for any nanomaterial [17-19]. This design flexibility creates an enormous interest with a high number of generated MOFs and coordination polymers for diverse purposes in multidisciplinary areas such as gas storage, catalysis, imaging, separation, energy storage and drug delivery [20-29].

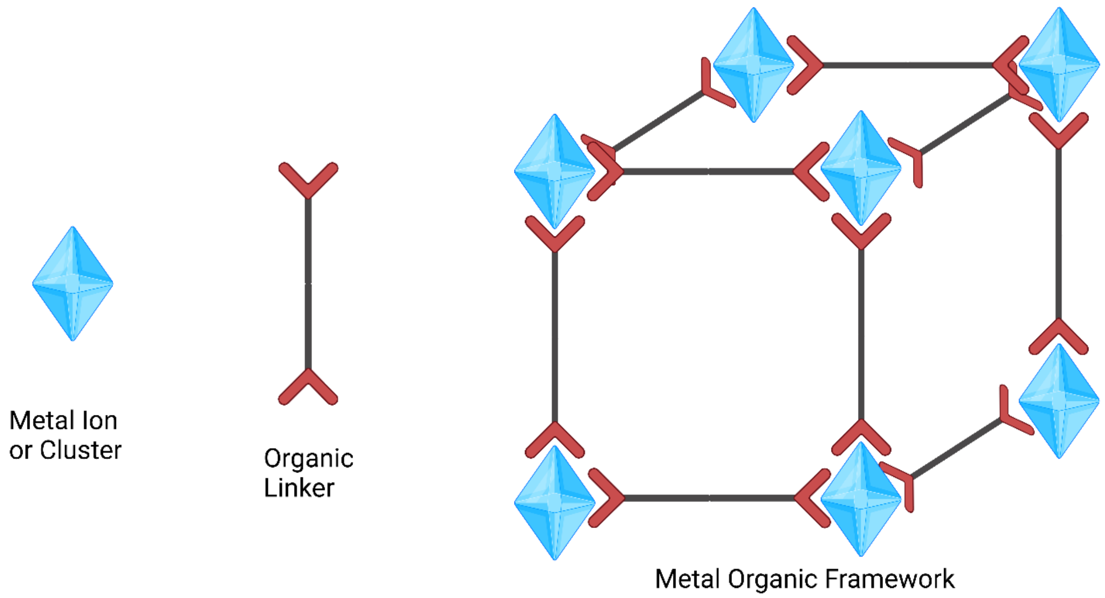

Figure 1 Schematic representation of MOFs. Coordination driven self-assembly of the metal ions or clusters and organic linkers leads to highly ordered framework. Created by BioRender.com (2022).

In the context of biomedical applications, MOFs and coordination polymers have been designed as carriers for small molecular drugs or biomolecules as well as frameworks with photo-sensitizing, radiation-enhancing and bio-imaging properties [30-38]. MOFs are able to be design for specific biological function because of their almost limitless variety that combines beneficial characteristic of metal cluster and organic linkers with structural diversities and tunable chemical properties for many biological applications [39]. This almost limitless variety provides always increasing library of materials with various properties. Of course some features are especially critical for biological applications. For example, most of the medical applications needs MOFs that are stable in aqueous environments otherwise first contact with the blood stream results in rapid disassociation of the material [40, 41]. Being nanosized is a huge adventage for MOFs as they have more surface area to enhance activity and stability or have more surface area for modifications. They also have improved dispensability and biological distribution [42-46]. One generally critical parameter for the application of nanopharmaceuticals is represented by the potential toxicity of the material. In case of MOFs, the tolerability of the individual components as well as the nanotoxicity of assembled particles have to be taken into consideration [47, 48]. Even MOFs that are formed from biologically occurant metals could be toxic [49, 50]. Organic ligands can also cause toxicity, which make finding of biocompatible organic linkers with low toxicity necessary for biological applications [51]. One strategy to overcome some of the toxicity issues is the utilization of well tolerated endogenous organic ligands, such as amino acids, peptides or nucleobases. The MOFs which have been generated based on this principle represent an own subset of the material class, called bio-MOFs [52]. However, even in case of well-tolerated nanomaterials, a high drug loading capacity and minimal exposure of patients with excessive carrier materials is favorable to prevent the risk of adverse reactions. Theoretically, maximal loading capacities could be achieved by nanomaterials which are formed by the bioactive entities themselves. Metal-organic nanopharmaceuticals built from drug molecules with Lewis base functions which assembly into coordination nanoparticles with metal ions approximate the envisioned nanocarriers with maximal loading capacity and minimal passive additives [53, 54]. While this concept has already been realized with low molecular weight therapeutics [55-58], coordination polymers containing linkers based on bioactive biomolecules or synthetic analogs have not been reported.

1.1.1 Bio-MOFs

Bio-MOFs are sub-class of MOFs derived from biological ligands such as amino acids, peptides, nucleobases and saccharides. They are emerging materials since their ligands improve biocompatibility of MOFs while retaining favorable MOF properties [52, 59].

1.1.1.1 Amino acids, peptides and proteins

Amino acids are compounds that contain carboxyl and amino groups as well as an organic side chain. They are a starting point of bio-derived organic ligands because of their various interaction sites for coordination with metal ions [60]. They can form chelates with metal ions via their carboxyl and amino groups. Amino acid side chains can also contain metal binding sites such as imidazoles, carboxylates and phenol rings [61]. Generally, natural amino acids were reported to form chelates with metal ions through O,N-chelation [62]. Use of amino acids alone predominantly leads to one dimensional frameworks, but it is also possible to get three dimensional frameworks with additional multidentate ligands or amino acids modified with additional metal binding sites [63-66]. For example, L-aspartate has been used to form a nickel aspartate oxide ($[Ni_2O(L\text{-}Asp)(H_2O)_2]\cdot4H_2O$). This complex had 1D, homochiral helical chain structure [67]. Then, the same group modified and tuned their framework by addition of $[NiAsp_2]_2$ which works as bridge between helixes to form a three-dimensional chiral material ($[Ni_{2.5}\text{-}(OH)(L\text{-}Asp)_2],6.55H_2O$) with one-dimensional channels [68].

Modified and natural amino acids have been utilized as biological ligands for MOFs and specifically can provide chirality and asymmetry to the framework [69-71].

Peptides are short chains of amino acids linked via amide bonds. They are the rational next step of amino acids as bridging ligands for MOFs. Like their monomers, peptides have both amino and carboxylic acid terminus which can form O,N-chelate with metal ions [62, 72]. Simplest peptides utilized as MOF ligands are dipeptides. They are also most abundant type of peptide linker for MOF synthesis [59, 73]. However, there are also examples of longer peptide linkers [74, 75]. Peptides form different structures based on stereochemical configuration of their amino acid sequence [76]. This feature of peptides is quite useful for asymmetric catalysis and enantioselective separation [77]. Peptide linkers can introduce flexibility to the MOF structure via amide bonds or additional carboxylate groups via use of suitable amino acids such as aspartate or glutamate for polydentate ligands [59, 73, 78-82]. In opposite direction, dipeptide Gly-Thr has been utilized to form $[Zn(Gly\text{-}Thr)_2]CH_3OH$ which has more conformational rigidity by the intralayer hydrogen bonding of the specific sequence of amino acids which enhances stability [83]. Just comparing dipeptide linkers alone shows that use of both rigid and flexible peptides is possible for designing MOFs. It also demonstrates tunability of stability and flexibility of future bio-porous material. In addition to advantages above, amino acids and peptides are cost-efficient and biologically compatible. It is not a surprise that modified and natural amino acids and peptides draw wide spread attention as MOF linkers [84-87].

Proteins are large nitrogenous organic compounds formed by one or more long amino acid sequences with complex and flexible three dimensional structure. Although they have ability to coordinate metal ions and some even require metal ions to properly fold, for a long while there were no examples of extended coordination frameworks constructed with metal ions and proteins [88-90]. Major obstacle for ordered coordination with metal ions are complexity and flexibility of the proteins as well as their heterogeneous surfaces which can unpredictably interact with each other or with metal ions [91]. However, Tezcan et al. were able to generate first protein–metal–organic crystalline framework composed of ferritin engineered with Zn coordination sites, Zn^{2+} metal ions and ditopic linker bearing hydroxamic acid and later expanding their protein-MOF library with various metals and linkers again with ferritin [92, 93].

1.1.1.2 Nucleobases

Nucleobases are basic building blocks of nucleic acids which are essential molecules for information carrying that are present at all known living organisms. Bio-MOFs constructed from nucleobases have been reported [94-97]. Nucleobases have rigid structure, hydrogen bonding capabilities and accessible nitrogen and oxygen to act as multidentate organic ligands [98]. Between nucleobases, adenine was so far most utilized because of its five potential metal-binding sites enabling different binding patterns which even form three dimensional porous structures [96, 99-101]. Unlike amino acids or peptides, there is no MOF structure described containing nucleotides or oligonucleotides as linkers through metal interaction. However, value of incorporating complex nucleic acids to the MOFs can be tremendous for biological applications. To incorporate oligonucleotides in to MOF structures methods for conjugation or adsorption can be used [102]. Several conjugation-based DNA functionalized MOFs have been reported, first example being realized by strain promoted click reaction between DNA with dibenzylcyclooctyne and azide-functionalized UiO-66-N_3 [31, 103, 104]. Oligonucleotide diffusion to MOF interior is also possible due to nucleic acid affinity towards metal centers and MOF inner microenvironment. Moreover, they were already utilized as biosensor with integrated fluorescently modified DNA for human immunodeficiency virus RNA or DNA [105-107]. Interestingly to the subject of the thesis, similarly labeled PNA probes were absorbed into the porous structure of UiO-66 (Figure 2) to monitor miRNAs in living cells [108].

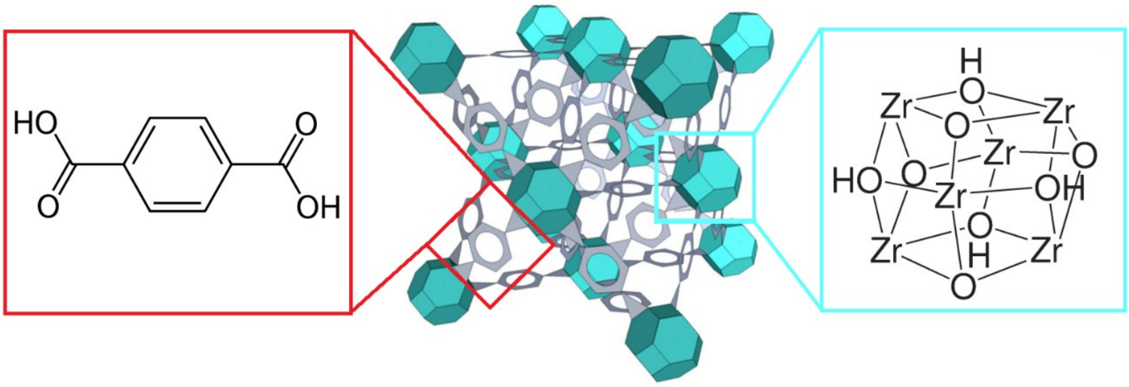

Figure 2 Structure of UiO-66. Adapted from Winarta et al. and DeStefano et al. [109, 110]. Created with BioRender.com (2022).

1.1.1.3 Saccharides

Another major group of bio-molecules is represented by saccharides. They are organic molecules composed of carbon, hydrogen and oxygen atoms which perform numerous roles in living organisms. However, they have not been extensively used as ligands to generate bio-MOFs with several exceptions. For example, γ-cyclodextrin (an oligosaccharide) and KCl have been used to generate edible MOFs according to authors claim [111]. Other saccharides such as mucic acid and glucaric acid were also reported to form three-dimensional frame works [112, 113].

1.1.1.4 Small molecules

There are numerous other acids and bases present in living organisms with potential to be a MOF ligand. Especially small molecules that harbor more than one carboxylate group because of their simpler form and rich coordination chemistry make perfect candidates as bio-MOF linkers. Thus, acids such as formic, fumaric, glutaric, malic, oxalic, succinic and tartaric acid were all extensively used to obtain a wide diversity of MOFs (Figure 3) [94, 114-118]. For example, nickel succinic acid based MOF have been generated by biphasic solvothermal synthesis. Its possesses three-dimensional structure with hydrophobic, one-dimensional channels [116].

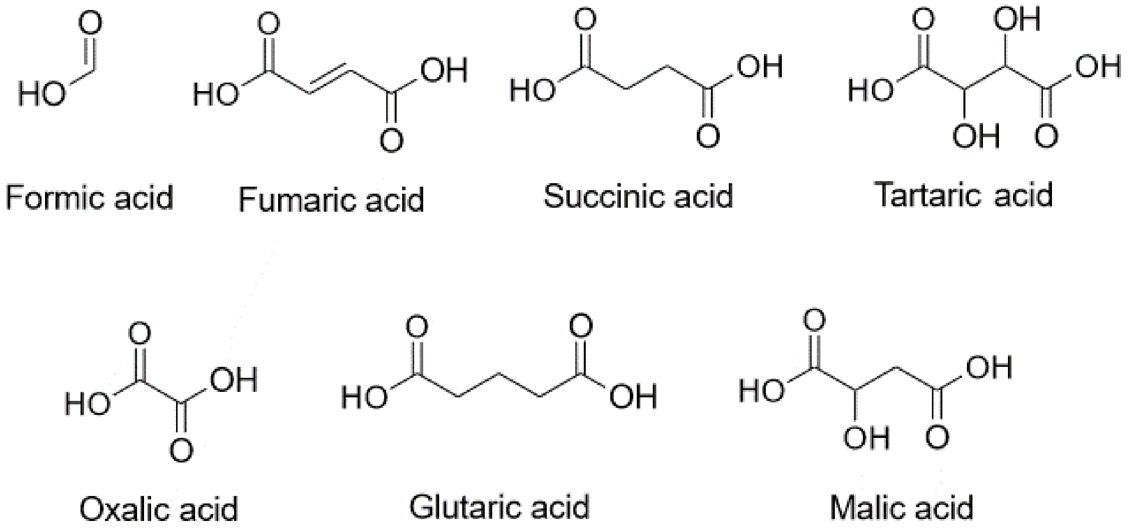

Figure 3 Small linker molecules harboring carboxylate groups.

1.2 Nucleic acid therapeutics

Every day, new information becomes available on various biological functions of nucleic acids and their role in genetic diseases [119, 120]. With elucidated additional roles of noncoding RNAs, microRNAs, short interfering RNAs (siRNA) and ribosomal RNA in transcription and translation regulation, new opportunities opened for therapeutic interventions at the nucleic acid level [121-124]. Given the enormous information available on various nucleic acids and their role in biology as well as genetics, this thesis will only focus on nucleic acid therapeutics.

The quest for modern therapeutic development aims for selective and efficient action on specific targets that are associated with the diseases. Unlike drugs that target proteins which often bind to non-target proteins which can result in unpredictable side effects, nucleic acid therapeutics aims to bypass non-specific effects to modulate gene expression directly. Almost five decades ago with first conceptualization of treating dysfunctional gene products by introducing functional gene copies, nucleic acid therapeutics developed at much slower pace than initially assumed [125]. This slow pace can be explained by unsolved three hard questions; which sequence should be the physical target and how and what should be delivered [126, 127]. Delivery problem itself comes with more questions; “How can nucleic acids be protected against degradation by nucleases?”, “How can stability in circulation be ensured?”, “How can immune reactions be prevented?” and most importantly “How can nucleic acids be transmitted to target locations and into target cells?” [128]. Scientists already developed various strategies such as chemical oligonucleotide backbone modifications, conjugation to transport vehicles, and supramolecular assembly into nanosized formulations to overcome mentioned problems and increase the number of treatable genetic diseases and cancers by elegant nucleic acid therapeutics [129-132]. Therefore, giving a comprehensive introduction to all nucleic acid delivery system is not focus of this thesis. To limit to scope, leading Food and Drug Administration (FDA) and European Medicines Agency (EMA) approved platform technologies; viral vectors, antisense oligonucleotides, ligand-modified small interfering RNA conjugates and lipid nanoparticles as well as promising system polyplex nanoparticles that utilized during this project, will be explained [128].

1.2.1 Viral vectors

Nucleic acid therapeutics holds huge promise for treatment of genetic diseases and cancers if the problem of efficient delivery can be solved. It is not surprising that scientist have been working on the development of viral vectors for decades, since viruses are natural carriers of nucleic acids. Initial clinical trials were as early as 1975 and first successful gene therapy trail has happened at 1989 with recombinant retrovirus carrying human retrovirus adenosine deaminase gene [133, 134]. Use of viral vector platforms mostly divided two groups according to whether their genomes integrate into host chromatin (retroviruses and lentiviruses) or stay and functions as extrachromosomal episomes (adenoviruses, adeno-associated viruses and herpes viruses) [135, 136]. Viral vectors are usually composed of a protein capsid and/or envelope that encapsulate nucleic acid cargo and these capsid and/or envelope define target, cargo of interest, which when expressed in cells, serves to confer a desired effect; and regulatory elements for stable or transient somatic expression such as enhancer and promoter [137]. Gene therapy by these vectors can follow two pathways: direct administration of viral vector carrying therapeutic nucleic acid into the patient or extraction of a patient's cells to carry out viral vector assisted genetic modification, selection and expansion in culture followed by re-introducing the engineered cells back into the patient [137]. Viral vectors possess ability to target specific cell types and actively deliver their cargo to the nucleus unlike most non-viral systems which rely on cell division for nucleus delivery [128, 137]. However viral vectors come with major disadvantages such as limited cargo capacity, immunotoxicities and genotoxicity caused by genome integration as well as risk of reversion into replication-competent virions [138, 139]. Between different viral vectors, adeno-associated viruses popularity increased in recent years [140]. Adeno-associated viruses are non-enveloped small viruses with a protein shell surrounding a single-stranded, 4.8 kb long DNA genome [141, 142]. They hold several advantages such as, non-pathogenic nature, the need of helper virus to replicate and inverted terminal repeats that drive recombination however limited cargo space is the major challenge for adeno-associated virus vectors [142-144]. For example, EMA and FDA approved voretigene neparvovec-rzyl (Luxturna) is an adeno-associated virus vector containing cDNA encoding the human RPE65 gene with cytomegalovirus enhancer and a hybrid chicken β-actin promoter. It remains episomal in the nucleus and facilitate RPE65 expression to introduce wild type gene against autosomal recessive disease inherited retinal dystrophy [145].

1.2.2 Antisense oligonucleotides (ASOs)

ASOs are typically between 13 and 30 nucleotides long single-stranded oligonucleotides that can hybridize with cellular RNA by classic Watson-Crick base pairing resulting in gene expression regulation [146]. They are known to cause competitive inhibition and sterically blockade translational machinery, and cause degradation via endogenous RNA degradation pathways. ASOs are also able to modify pre-mRNA processing and splicing which forms a sub group called splice-switching oligonucleotides (SSOs) [147, 148]. Ability to interact with both mRNA and pre-mRNA dramatically increases available RNA sequences which can be targeted by ASOs. They also show high sequence specificity compared to miRNA [149]. Although ASOs can be administered through multiple ways because of their small size, unmodified ASOs are rapidly degraded by serum nucleases [150]. Because of this reason ASOs are mostly chemically modified. Modifications such as 2′-O-methyl (2′-OMe), 2′-O-methoxyethyl (2′-MOE) and 2′-O-aminopropyl (2′-O-AP) are utilized to improve RNA target binding affinity and increase nuclease resistance [151]. In additionally to chemical modification, ASO can be conjugated to a ligand to control targeting and cellular tropism. For example cholesterol and GalNAc conjugation to ASOs reduces renal accumulation and results in liver targeting [152]. First clinically available example of ASO use was Vitravene, in which phosphorothioate-based ASO binds to the major immediate-early protein messenger RNA of human cytomegalovirus and inhibit the viral replication in the immediate-early stage of the replication [153, 154].

1.2.3 Small interfering RNA conjugates

Small interfering RNAs (siRNAs) are typically between 20 and 30 nucleotides long, noncoding, double-stranded RNAs that can down regulate gene expression via RNA interference pathway [155]. In this pathway effector nucleases form a RNA-induced silencing complex and siRNAs guide that complex to homologous substrates [156]. Similar to ASOs, chemical modification to increase stability in the circulation is essential for siRNA [157]. Ligand conjugation is an efficient way to provide organ or cell targeting and improve cellular uptake for most therapeutics. A prominent example is GalNAc conjugated siRNAs. These conjugated siRNAs can target asialoglycoprotein receptor with GalNAc moiety [157]. This receptor is predominantly present at hepatocytes and can bind carbohydrates with terminal galactose or GalNAc [158]. Engineering triantennary GalNAc structure can further be used to improve ligand affinity and similar chemical modifications as used for ASO therapeutics, such as 2′-OMe, can be applied to siRNA therapeutics [159, 160]. A clinical example for this technology is the EMA and FDA approved RNAi therapeutic Givosiran for the treatment of acute hepatic porphyria [161]. It utilizes a GalNAc ligand to direct covalently attached siRNA against aminolevulinate synthase 1 to hepatocytes . The siRNA reduces and prevents elevated aminolevulinate synthase expression by the RNAi pathway.

1.2.4 Lipid nanoparticles

Nucleic acids do not permeate across plasma membranes because of their large size and charged nature. Lipid nanoparticles (Figure 4) offer an alternative way to deliver a variety of cargos such as hydrophobic or hydrophilic molecules, including small molecules, proteins, and nucleic acids [162]. These nanoparticles generally work by temporarily compromising the permeability barrier and allowing their cargo to enter the cell. First lipid nanoparticles used to deliver DNA were small unilamellar liposomes containing 1,2-di-O-octadecenyl-3-trimethylammonium propane (DOTMA) [163]. Later various lipid nanoparticles such as solid lipid nanoparticles, nanostructured lipid carriers, and cationic lipid–nucleic acid complexes were generated [164-166]. Lipid nanoparticles are the earliest nanomedicine delivery platform used for clinical applications [167]. They are one of the most successful delivery systems, because of several characteristic features: (1) they provide a compartment for their cargo protected from external nuclease activity [162], (2) cargo distribution can potentially be controlled by functionalization with ligands added to the particles [168, 169], (3) they can be coated with inert polymers, such as poly(ethylene glycol) (PEG) to avoid immune response as well as increase circulation time and passive accumulation in cancer tissues by the enhanced permeability and retention effect [170-172]. (4) controlled drug release is possible with modifications resulting in stimuli responsive liposomes which can also improve endosomal escape by pH response [173-175]. A recent example of the relevance and potential of lipid nanoparticles is presented by their role during the global COVID-19 pandemic. The vaccines by Pfizer/BioNTech and Moderna both contain ionizable pH responsive lipids for mRNA complexation and controlled release [162, 176-179]. These ionizable lipids have neutral charge physiological pH and became cationic in lower pH. This makes them less toxic in the blood stream because of neutral charge. Cationic charge at lower pH enabling RNA complexation and facilitates membrane disruption during endosomal escape [166, 180]. The vaccines by Pfizer/BioNTech and Moderna also contain PEGylated lipids to reduce clearance by phagocytes and to achieve longer systemic circulation. The phospholipid distearoylphosphatidylcholine and cholesterol in the vaccine formulation helps mRNA incorporation and improves hydrophobic stability. The vaccines transfers mRNA that encodes for the SARS-CoV-2 spike protein. Translation occurs at the host cells generating the spike protein that acts as antigen resulting in the development of an immune response [162, 176-179].

1.2.5 Polyplex nanoparticles

Another elegant strategy to overcome the therapeutic nucleic acid delivery problem is the use of cationic polymeric carriers. As a result of the entropy-driven ionic interaction between anionic nucleic acids and cationic polymers, the nucleic acid can be compacted and transported in vectors called ‘polyplexes’ (Figure 4) [126, 181, 182]. These compacted nucleic acids are protected against nucleases [183]. The positive charge of polyplexes can enhance transfection efficiency by binding with negatively charged cell surfaces and can mediate endosomal membrane destabilization for endosomal escape [184, 185]. Whereas they can also cause interaction with cells and blood components and nonspecific uptake

[126]. Therefore, PEG is commonly used as shielding agent [186]. PEG molecules come with change in nucleic acid complexation, size and stability of polyplexes [187-189].

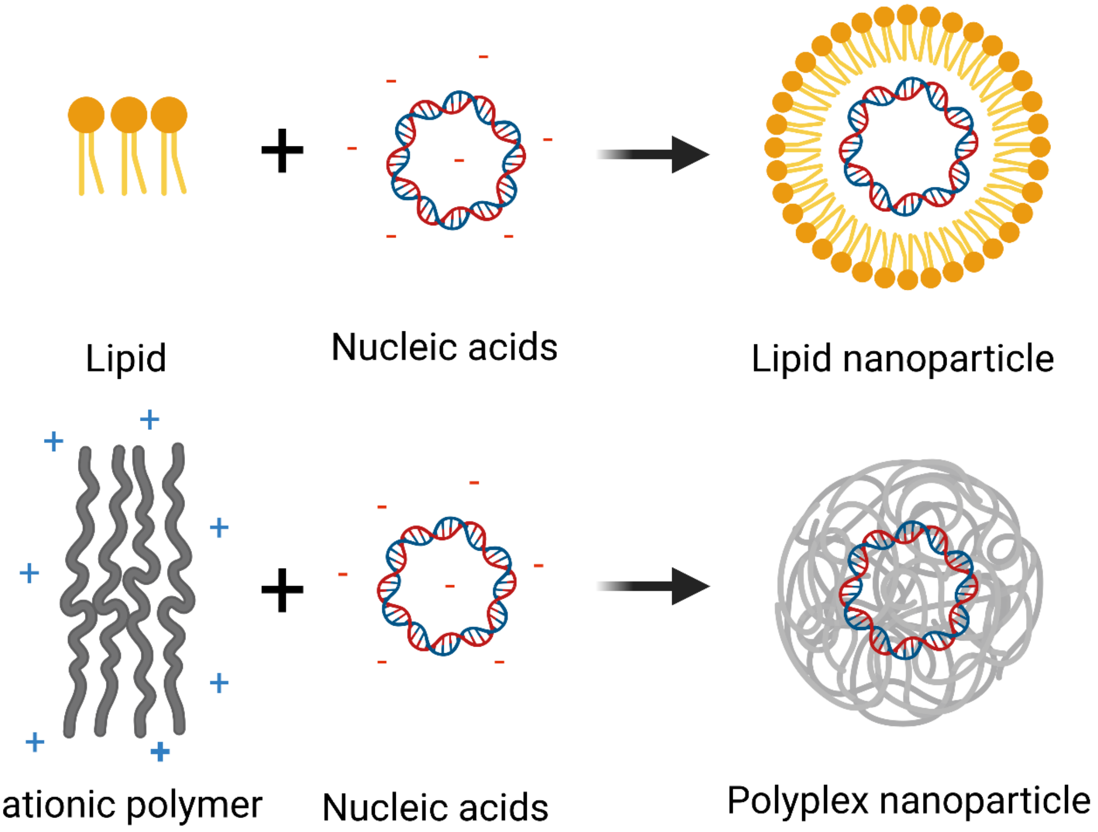

Figure 4 Simple schematic illustration of a lipid nanoparticle and polyplex nanoparticle. Created with BioRender.com (2022).

Polyplexes also provide opportunity of surface design with ligands to increase effective and specific transfection. Generally, receptors which are overexpressed by the target cells are selected [190]. One of the most commonly used peptides for tumor targeting is arginine–glycine–aspartic acid (RGD) to target cell surface integrins [191-194]. Other receptors for tumor targeted delivery are folate receptor (FR) and transferrin receptor (TfR), which are transport proteins for the uptake of nutrients and cofactors. These receptors are overexpressed in tumor cells and can enhance receptor mediated uptake in cancer cells [195, 196].

Polyplexes have to escape from endosomes for effective nucleic acid delivery. Some nucleic acid binding polymers such as polyethylenimine (PEI) show endosomal escape performance and high transfection efficiency [197]. Even after cellular delivery and endosomal escape the fate of the nucleic acid cargo still depends on the carrier. For instance, polyplexes with both linear PEI (LPEI) and branched PEI (BPEI) were capable of endosomal escape, however LPEI polyplexes showed higher and faster expression than BPEI because BPEI were more effective at condensation of pDNA and restricted cytoplasmic release [198]. Polyplex based delivery systems hold promise to become ‘smart carrier systems’ that can dynamically respond to environmental factors.

1.3 Peptide nucleic acids

Peptide nucleic acids (PNAs) are synthetic polymers which combines features of both peptides and oligonucleotides. They are DNA/RNA analogues with peptide backbone composed of N-(2-aminoethyl)-glycine units instead of sugar-phosphate and nucleobases attached to this backbone via carbonyl methylene linkers (Figure 5) [199]. Although they are not naturally present biological compounds, their building blocks peptide backbone and nucleobases are quite essential biological components present at ever organism. Similar to natural nucleic acids, PNA oligomers bind with high affinity and specificity to complementary DNA, RNA or PNA sequences. In fact, the affinity and binding strengths of complementary PNA-PNA, PNA-DNA or PNA-RNA duplexes are higher and less affected by ionic stress then duplexes from analog DNA or RNA sequences [200, 201]. PNAs represent a powerful synthetic nucleic acid technology due to (1) their stable and strong binding ability, (2) good mismatch sequence discrimination, (3) synthetic accessibility and flexibility, and (4) resistance to degradation by nucleases and proteases [202-204]. Besides bioanalytical applications such as nucleic acid probing, *in situ* hybridization and polymerase chain reaction (PCR) modulation [205-208], PNAs can function as antisense oligonucleotides to silence gene expression and modulate cellular mRNA splicing [209, 210]. For instance, a PNA oligomer targeting the collagen gene was found to decrease mRNA and reduced production of type I collagen in fibroblast cells [211]. Another antisense PNA oligomer targeting microRNA-155, which is an oncogenic microRNA, successfully inhibited its overexpression *in vivo* [212]. Accept from their antisense function, sequence-specific interference of the mRNA splicing machinery is also possible with PNA based drugs [209, 210]. Kang et al. generated a HeLa cell reporter system for the detection of correction of aberrant β-globin intron splicing by synthetic oligonucleotides (including PNAs), resulting in upregulated luciferase activity [213, 214]. Similar to other nucleic acid chemistries, cellular delivery represents a major challenge for antisense applications of PNAs. Despite the neutral charge and lipophilic character, peptides do not efficiently cross the cellular membrane. For this reason, PNAs were conjugated to cell-penetrating peptides, formulated in delivery systems, or chemically modified in the backbone to enable cellular delivery. [215-218]

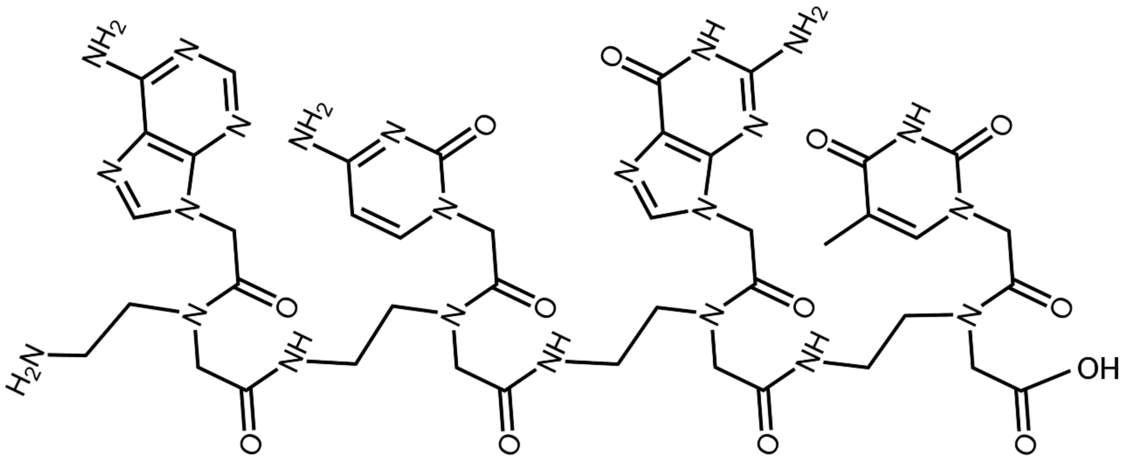

Figure 5 Chemical structure of PNA polimer. From N-terminus to C-terminus; adeninine, cytosine, guanine and thymine [199].

1.4 Aim of the thesis

Nucleic acid therapeutics had been on the spotlight from the first time they had been conceptualized until now and yet there are only a handful of authorized examples on the market. Although enormous amount of information is available on different nucleic acids that can be utilized to treat various diseases, a major limiting factor to develop therapeutics always had been delivery. Development of selective and efficient delivery systems for nucleic acids that specifically target the diseases without causing unwanted side effects is the key to successfully overcome this bottleneck and so revolutionize molecular medicine.

The aim of this thesis was the development of PNA based Zr coordination nanoparticles to combine superior adjustability of coordination polymers with sequence-specific therapeutic effects of oligonucleotide analog PNAs. By doing so, generated nanocarriers will have a low amount of inactive carrier materials and have extremely high content of the therapeutic cargo. For this purpose, the architecture of single- or double-stranded PNAs was systematically varied to identify design criteria for the coordination driven self-assembly with Zr(IV) nodes. After establishing a novel method for generation of coordination nanoparticles, peptide nucleic acid – zirconium coordination nanoparticles (PNA-Zr) were characterized. Then bio-imaging capability was assessed by dye loading and subsequent confocal laser scanning microscopy (CLSM). The thesis further aimed at evaluating the suitability of PNA-Zr particles for therapeutic PNA delivery by generating and formulating particles from an antisense PNA sequence for splicing correction of the β-globin intron mutation IVS2-705.

2. Material and Methods

This chapter has been adapted from:

Öztürk Ö., Lessl A., Höhn M., Wuttke S., Nielsen P., Wagner E., Lächelt, U., Peptide Nucleic Acid – Zirconium Coordination Nanoparticles. Manuscript to be submitted.

2.1 Materials

All reagents were purchased from commercial chemical suppliers. Reagents were used as received without further purification unless otherwise stated. The reagents used for the experiments are summarized in Table 1. Buffers used for the experiments are summarized with their composition in Table 2.

PNA syntheses were carried out with a Biotage Initiator+ SP Wave semiautomatic peptide synthesizer (Biotage, Uppsala, Sweden). Disposable syringe micro reactors were purchased from Multisyntech (Witten, Germany) with pre-fitted polytetrafluoroethylene (PTFE) filters.

Table 1 Reagents used for experimental procedures

Materials	CAS-No./Cat-No.	Supplier
(10x) Trypsin 0.5 %/EDTA 0.2 % in PBS, w/o: Ca and Mg	P10-024100	PAN-Biotech (Aidenbach, Germany)
1,2-Dioleoyl-sn-glycero-3-phosphocholine (DOPC)	4235-95-4	Sigma-Aldrich (Munich, Germany)
1-Hydroxybenzotriazole hydrate	123333-53-9	Sigma-Aldrich (Munich, Germany)
2,6-Lutidine	108-48-5	Sigma-Aldrich (Munich, Germany)

2-Chlorotritylchloride resin	42074-68-0	Iris Biotech (Marktredewitz, Germany)
4-(Fmoc-aminomethyl)benzoic acid	164470-64-8	Iris Biotech (Marktredewitz, Germany)
4-(tert-Butoxycarbonyl)benzoic acid	20576-82-3	BLD Pharmatech GmbH (Mehlingen Germany)
4′,6-Diamidino-2-phenylindole (DAPI)	D9542	Sigma-Aldrich (Munich, Germany)
Acetic anhydride	108-24-7	Sigma-Aldrich (Munich, Germany)
Acetonitrile	75-05-8	VWR Int. (Darmstadt, Germany)
Agarose NEEO Ultra	9012-36-6	Carl Roth (Karlsruhe, Germany)
Beetle luciferin sodium salt	E1605	Promega (Mannheim, Germany)
Calcein	154071	Sigma-Aldrich (Munich, Germany)
CellTiter-Glo®	G7571/2/3	Promega (Mannheim, Germany)
Dichloromethane	75-09-2	Bernd Kraft (Duisburg, Germany)
DMEM	D6046	Sigma-Aldrich (Munich, Germany)
Ethanol absolute	64-17-5	VWR Int. (Darmstadt, Germany)
Fetal bovine serum (FBS)	F9665	Sigma-Aldrich (Munich, Germany)
Flasks and multi-well plates	-	TPP (Trasadingen, Switzerland)
Fmoc-PNA-A(Bhoc)-OH	186046-82-2	ASM Research Chemicals GmbH (Hannover, Germany)
Fmoc-PNA-C(Bhoc)-OH	186046-81-1	ASM Research Chemicals GmbH (Hannover, Germany)
Fmoc-PNA-G(Bhoc)-OH	186046-83-3	ASM Research Chemicals GmbH (Hannover, Germany)

Fmoc-PNA-T-OH	169396-92-3	ASM Research Chemicals GmbH (Hannover, Germany)
GelRed	41003	VWR International GmbH (Darmstadt, Germany)
HEPES	7365-45-9	Biomol (Hamburg, Germany)
H-Rink-Amide-ChemMatrix®	CM-7600	Iris Biotech (Marktredewitz, Germany)
LP LenA	-	In house synthesis [219]
Luciferase cell culture lysis buffer	E1500	Promega (Mannheim, Germany)
Methanol	67-56-1	Fisher Scientific (Schwerte, Germany)
Methyl-tert-butyl ether	1634-04-4	Brenntag (Mülheim/Ruhr, Germany)
***N,N'*-Diisopropylcarbodiimide**	693-13-0	Iris Biotech (Marktredewitz, Germany)
N,N-Diisopropylethylamine	7087-68-5	Iris Biotech (Marktredewitz, Germany)
***N,N*-Dimethylformamide**	68-12-2	Iris Biotech (Marktredewitz, Germany)
***n*-Hexane**	110-54-3	Brenntag (Mülheim/Ruhr, Germany)
***N*-Methyl-2-pyrrolidone**	872-50-4	Iris Biotech (Marktredewitz, Germany)
OxymaPure	3849-21-6	Iris Biotech (Marktredewitz, Germany)
Penicillin-Streptomycin	P4333	Sigma-Aldrich (Munich, Germany)
Piperidine	110-89-4	Iris Biotech (Marktredewitz, Germany)
Pybop®	128625-52-5	Merck KGaA (Darmstadt, Germany)
Rhodamine-Phalloidin	R415	Life Technologies/Thermo Fisher Scientific (Munich, Germany)
Sephadex® G-10	9050-68-4	GE Healthcare (Freiburg, Germany)

Sodium Hyaluronate, HA 20 kDa	028292	Lifecore Biomedical (Minneapolis, USA)
Sodium Hyaluronate, HA 100 kDa	026472	Lifecore Biomedical (Minneapolis, USA)
Terephthalic acid	100-21-0	Sigma-Aldrich (Munich, Germany)
Trifluoroacetic acid	76-05-1	Iris Biotech (Marktredewitz, Germany)
Triisopropylsilane	6485-79-6	Sigma-Aldrich (Munich, Germany)
Trypsin-EDTA	P10-024 100	PAN-Biotech (Aidenbach, Germany)
Zirconium(iv) propoxide solution	23519-77-9	Sigma-Aldrich (Munich, Germany)

The buffers used for the experiments are presented in Table 2.

Table 2 Buffers used for experimental procedures

Buffer	Composition
Freeze-dry solvent	30 % (v/v) acetonitrile in water
HBG	20 mM HEPES, 5 % glucose, pH 7.4
HEPES	20 mM HEPES, pH 7.4
LAR Buffer	20 mM glycylglycine, 1 mM $MgCl_2$, 0.1 mM EDTA, 3.29 mM DTT, 0.548 mM ATP (adenosine 5′-triphosphate), 0.55 mM Coenzyme A stock solution, pH 8.0-8.5
Luciferin	10 mM Luciferin-Na, 1M Glycylclycine, pH 8.0,
Phosphate-buffered saline (PBS)	137 mM NaCl, 2.7 mM KCl, 8.1 mM Na_2HPO_4,1.5 mM KH_2PO_4, pH 7.3-7.5
Size Exclusion Chromatography Mobile Phase	700 mL water, 300 mL acetonitrile
TBE buffer	89 mM Trizma® base, 89 mM boric acid, 2 mM EDTA-Na_2, pH 8.0

2.2 Methods

2.2.1 Resin loading with 4-(Aminomethyl)benzoic acid (PAMBA)

An amount of 1 gr of 2-chlorotrityl chloride resin (approximately 1.6 mmol chloride) was swelled in 10 mL of dry dichloromethane (DCM) for 30 minutes (mins) in a syringe reactor (Multisyntech, Witten, Germany). Then DCM was removed by vacuum filtration. The resin was agitated for 60 mins with mixture of 4 mL of dry DCM, 3 mL of *N,N*-dimethylformamide (DMF), 0.6 mmol of 4-(Fmoc-aminomethyl)benzoic acid (Fmoc-PAMBA-OH) and 1.8 mmol *N,N*-diisopropylethylamine (DIPEA) in order to load PAMBA to the resin. Then solvent was discarded via vacuum filtration and resin was agitated with capping mixture of 4 mL DCM, 3 mL methanol and 500 µL *N,N*-diisopropylethylamine (DIPEA) for 30 mins. This step turns unreacted chlorides to unreactive methoxy ethers. Then the resin was washed three times with DMF and then three times with DCM under vacuum filtration. The resin was dried under high vacuum and stored in airtight container at 4 °C. From the dry resin, three aliquots of approximately 20 mg were taken in order to determine resin loading by Fmoc quantification. Aliquots were agitated with 1 mL of 20 % piperidine in DMF at room temperature (RT) for 1 hour (h) and left for 2 mins for resins to settle at the bottom. 50 µL of the supernatant of each aliquot was diluted with 1.95 mL DMF and absorbance was measured at 301 nm wavelength with Cary 3500 UV-Vis Spectrophotometer (Agilent Technologies, United States of America). As a blank solution 50 µL 20 % piperidine in DMF diluted with 1.95 mL DMF was used. Fmoc quantification was determined by using average absorbance value of samples with following formula: resin load [mmol/g] = (Absorbance (A_{301nm}) x 1000) / (resin mass [mg] x 7800 [$L*mol^{-1}*cm^{-1}$] (molar extinction coefficient) x 0.025 (dilution factor)).

2.2.2 Solid phase synthesis

PNA syntheses were carried out with a Biotage Initiator+ SP Wave semiautomatic peptide synthesizer (Biotage, Uppsala, Sweden) at 30 µmol scales in 10 mL reactors. Several different PNA sequences were produced. If there was PAMBA at C terminal end of the structure, PAMBA loaded 2-chlorotrityl chloride resin was used otherwise H-Rink-Amide-Chemmatrix® was used. Syntheses were usually performed at 30 µmol scale, which corresponded to optimal solvent volumes for 10 mL reactors. Fmoc-PNA-C(Bhoc)-OH solubility was the limiting factor for more concentrated synthesis. First, resin was swelled in 5 mL of DCM for 30 mins. Then, the resin was deprotected by four times incubation with 3 mL of 20 % piperidine in *N*-methyl-2-pyrrolidone (NMP) for 10 mins at RT. Then, the resin was washed five times with 4 mL NMP. After deprotection, the coupling cycle for the first PNA monomer was carried out by incubating 4 equivalents (eq) PNA monomer, 4 eq of Oxyma and 4 eq of DIC with the resin for 6 mins at 75 °C. Coupling reagents were individually dissolved in NMP and mixed just before the coupling manually. After first coupling, the resin was washed three times with NMP. Then, the second coupling step was performed exactly the same way as the first one. After double couplings, acetylation was carried out by 3 mins incubation at RT with 2.25 mL of a mixture containing NMP, 2,6-lutidine and acetic anhydride at the ratio 89/6/5 (v/v/v) to block residual free amines. Afterwards, the resin was washed five times with 2.4 mL NMP. Double coupling steps and acetylation steps are optional for short PNA sequences but recommended for sequences longer than 12 monomers. Finally, the first cycle was finished with deprotection of the first monomer. Deprotection was performed by four times incubation with 2.4 mL of 20 % piperidine in NMP for 10 mins at RT, followed by five times resin wash with 2.5 mL NMP. Same coupling, acetylation, deprotection cycles were performed until all PNA monomers were added to the structure. It is important to make sure that washing steps have slightly higher volume then previous steps. After each coupling and deprotection step, presence of free amine groups was determined by the Kaiser test. A small amount of resin sample was taken into a 1.5 mL reaction tube with help of a spatula. Inside the tube, single drops of 80 % phenol in ethanol (w/v), 5 % ninhydrin in ethanol (w/v) and 20 µM potassium cyanide in pyridine were added with help of glass pipettes. The mixture was vortexed and agitated at 99 °C for 4 mins. The Kaiser test indicates presence of free amines by change of the yellow solution to a deep blue color, otherwise the color does not change. The resin was washed three times with DCM and dried under high vacuum to be stored in airtight container at 4 °C or modifications were performed to N terminal end of the structure.

2.2.2.1 N terminal end modification

After the PNA sequence has been completed, N-terminal modification was accomplished with a slightly modified coupling procedure. First, resin was swelled in 5 mL of dry DCM for 30 mins. The resin was incubated with a mixture of 4 eq of mono-*tert*-butyl terephthalate, 4 eq 1-Hydroxybenzotriazole (HOBt), 4 eq benzotriazol-1-yloxy-tripyrrolidinophosphonium hexafluorophosphate (PyBOP) and 8 eq DIPEA dissolved in DMF for 10 mins at 70 °C. After washing three times with 3 mL DMF and three times with DCM, resin was stored in airtight container at 4 °C.

2.2.3 Cleavage and purification of the PNA product

PNA products were cleaved from previously dried resins by addition of cleavage cocktail composed of 2.85 mL trifluoroacetic acid (TFA), 75 µL triisopropylsilane (TIS) and 75 µL double distilled water. The resin was agitated for 90 mins with cleavage cocktail. The cleavage solution was added into 45 mL of a pre-cooled mixture of methyl-*tert*-butyl ether (MTBE) and *n*-hexane 1/1 (v/v) in a 50 mL reaction tube. Formed precipitate was centrifuged for 5 mins at 4000 rpm (Megafuge 1.0 R, Heraeus, Hanau, Germany) and the supernatant was removed. The formed pellet was dried under nitrogen flow. Then, the dry product was dissolved in 30 % acetonitrile in water and snap-frozen by liquid nitrogen. Freeze drying was performed with a Christ Alpha 2–4 LD plus (Martin Christ Gefriertrocknungsanlagen GmbH, Osterode, Germany). The product was purified by size exclusion chromatography using 30 % acetonitrile in water as mobile phase through Sephadex G-10 column. Äkta purifier system (GE Healthcare Bio-Sciences AB, Uppsala, Sweden) was used to perform size exclusion chromatography. It is important to avoid any additional acid in the mobile phase because particle formation experiments are sensitive to presence of the acids.

2.2.4 MALDI mass spectrometry

Samples were spotted on a MTP AnchorChip (Bruker Daltonics, Bremen, Germany) by first crystallizing 1 µL of saturated Super-DHB matrix solution (2,5-dihydroxybenzoic acid and 2-hydroxy-5-methoxybenzoic acid), followed by addition of 1 µL of sample solution. After drying in a dust free environment, mass spectra were recorded in positive mode with a Autoflex II mass spectrometer (Bruker Daltonics, Bremen, Germany). MALDI-TOF mass spectrometry measurements were performed by Teoman Benli-Hoppe, Simone Berger and Tobias Burghardt (LMU Pharmaceutical Biotechnology)

2.2.5 Particle synthesis

PNA-Zr particle synthesis required a two-step process to enable the assembly at RT and avoid melting of PNA duplexes. A previously reported method for the synthesis of UiO-66 at RT served as basis for particle synthesis [110]. First step was the formation of Zr nodes. Nodes were formed by mixing 71 µL of a 70 wt. % zirconium(IV) propoxide solution in 1-propanol (0.0519 g, 0.158 mmol), 7 mL of DMF, and 4 mL of acetic acid in a glass sealed container. The solution was heated 130 °C for 2 h. Then, a noticeable change in solution color from colorless to yellow was observed. The solution was allowed to cool to RT before continuation with the second step. Scaling down the node formation is possible, however storage of the node solution for later use is not recommended. Nodes were freshly synthesized and used just after cooling to RT. PNA linkers were subjected to an aneling process if they were double stranded structures or palindromic. PNA strands were completely dissolved in double distilled water, concentrations were determined photometrically by using the formula: µmolar amount = A_{260nm} / extinction coefficient of specific PNA (µmole). Measurements were performed with a Cary 3500 UV-Vis Spectrophotometer (Agilent Technologies, United States of America). After concentration determination, equal molar amounts of complementary strands were added together and slowly heated up to 90 °C over 30 mins and cooling to RT over 30 mins. Annealing step was skipped for single stranded, non-palindromic PNA linkers. Then acetonitrile was added to the aqueous PNA solution until 30 % (v/v) of acetonitrile. Samples were snap-frozen in liquid nitrogen and freeze-dried. PNA linkers were re-dissolved in DMF at concentrations of 1-4 mg/mL, depending on the solubility. Finally, the pre-formed Zr node solution was mixed with the PNA linker solution at equimolar ratio. It is important to note that, palindromic PNA strands form double-stranded linkers and their molar ratio should be calculated accordingly. This mixture was incubated for 24 h at RT with magnetic stirring. The formed Zr-PNA particles were separated from the supernatant by centrifugation for 5 mins at 4000 rpm and were washed three times by resuspending the pellet in DMF and centrifugation. Then solvent was exchanged with ethanol and particles were washed two times by resuspending the pellet in ethanol and centrifugation. Finally, the pellet was resuspended at 1 mL ethanol and stored at 4 °C.

2.2.6 X-ray diffraction of the PNA-Zr particles

Previously dried approximately 2 mg of PNA-Zr particles was used for X-ray diffraction (XRD) measurements with a STOE transmission diffractometer system Stadi MP with Cu Kα1 radiation (λ = 1.54060 Å) and a Ge (111) single crystal monochromator. Diffraction patterns were recorded with a DECTRIS solid-state strip detector MYTHEN 1K (step size of 4.71°, counting time of 120 s per step). Generated data was analyzed with WinXPOW RawDat v3.0.2.5.

2.2.7 Nitrogen sorption measurements

Approximately 20 mg of dry PNA-Zr particles was degassed at RT under high vacuum for 38 h. Nitrogen sorption isotherm was determined with Autosorb iQ Station 1 at 195.8 °C and generated data evaluated via the ASiQwin^{TM} software (Version 3.0, Quantachrome Instruments). Surface area of the samples was calculated by linearized Brunauer–Emmett–Teller equation (BET). Pore size was calculated according to quenched solid density functional theory carbon model (at 195.8 °C, nitrogen and relative pressure between 0 to 1 atm).

2.2.8 Determination of Zr content of PNA-Zr particles

Inductively coupled plasma atomic emission spectroscopy (ICP-AES) was performed with three independent samples. Samples were first vacuum dried for 24 h followed by 4 h drying at 90 °C. Digestion was performed with 69 % HNO_3 in water until no undissolved material was left. Then the samples were diluted with 3 % HNO_3 in double distilled water and Zr content was measured by ICP-AES (CCD simultaneous ICP AES Vista RL by Agilent, wavelengths 257.2, 327.3, 339.2, 343.8 and 349.7, suction time 35 seconds, stabilization time 45 seconds, power 1.25 kW). The average ratio of Zr to total mass of three samples was calculated.

2.2.9 Dynamic light scattering (DLS) and zeta potential

Size and zeta potential measurements were performed with a Zetasizer Nano ZS with backscatter detection (Malvern Instruments, Worcestershire, UK). PNA-Zr particles were sonicated for 5 mins before the measurement. Approximately 2.5 µg of PNA containing particles (2-3 µL) was added to 125 µL of distilled water.

Samples were placed in folded capillary cuvettes (DTS1070). Hydrodynamic size and polydispersity index (PDI) were measured by DLS. Samples were measured three times at RT with 1 min equilibration time and at least 6 subruns. Refractive index (1.330) and a viscosity (0.8872 cP) of water were used for the calculations. After size and PDI measurements, 835 µL of 10 mM NaCl was added to the samples and mixed for zeta potential determination by electrophoretic light scattering (ELS). Samples were measured three times at RT with 1 min equilibration time and at least 12 subruns. Smoluchowski equation was used for zeta potential calculations.

2.2.10 Scanning electron microscopy (SEM)

Stock solutions of PNA-Zr particles were vortexed and 5 µL of samples were further diluted with 45 µL ethanol. Diluted solutions were spotted onto the hydrophobic surface of a SEM sample holder. Ethanol from the samples was evaporated by overnight incubation in a dust free environment. Dried samples were coated with a carbon layer by three cycles of carbon vacuum deposition. SEM measurements were carried out with a Dual beam FEI Helios G3 UC SEM operated at 3 kV. Measurements were carried out by Dr. Steffen Schmidt (LMU Munich, Germany).

2.2.11 Particle stability

The stability of PNA-Zr in presence of HBG and HEPES was investigated by photometric measurement of the optical density of particle suspensions. For this purpose, approximately 50 µL of PNA-Zr particles solutions was added into quartz cuvettes with 2 mL of HBG or HEPES. The same volume of ethanol was added into separate cuvettes with HBG or HEPES as blank controls. Absorbance values of the samples at 400 nm wavelength were determined each min for 1 h. Data collection was performed with an automated program by Cary 3500 UV-Vis spectrophotometer under constant stirring.

For thermal stability assessments, approximately 50 µL of PNA-Zr particles was added into 2 mL water. Same volume of ethanol was added into water as blank control. A temperature probe was placed on top of quartz cuvettes while making sure that the temperature reader was completely submerged by liquid and cuvette was sealed. Samples were exposed to a temperature gradient between 25 °C to 70 °C with an increase rate of 1 °C per min. Absorbance values of the samples at 400 nm wavelengths were collected for each half degree celsius increase of the temperature. Data collection was performed with an automated program by Cary 3500 UV-Vis spectrophotometer under constant stirring.

Particle stability at different dilutions of PBS and 20% FBS was investigated similarly by photometric measurement of the optical density of particle suspensions. Different PBS dilutions were prepared and approximately 50 µL of PNA-Zr particle suspension was added into quartz cuvettes to 2 mL of solution. The same volume of ethanol was added into separate cuvettes with PBS dilution as blank control. For the stability determination in presence of serum, 20% FBS in water was prepared and 50 µL of PNA-Zr particle suspension was added into 2 mL of 20% FBS. As blank 2 ml 20% FBS with 50 µL of ethanol was used. Absorbance values of the samples at 400 nm wavelength were determined each min for 1 h. Data collection was performed automatically with a Cary 3500 UV-Vis spectrophotometer under continuous stirring.

2.2.12 Particle coating

For 1,2-dioleoyl-sn-glycero-3-phosphocholine (DOPC) coating, the amount of 1 mg PNA-Zr particle was redispersed in 100 µL water/ethanol mixture (20/80, v/v). 100 µL solution of 7.2 mM DOPC in water/ethanol mixture (20/80, v/v) was mixed with particles. Then on top of the mixture, 1800 µL water was rapidly added and vortexed. Particles were isolated via centrifugation (5 min, 13000 rpm) and dispersed in 100 µL water.

For hyaluronic acid (HA) coating, 20 mg/mL HA (20 or 100K) solution in water was prepared. Approximately 1 mg particle in 100 µL water and 100 µL 20 mg/mL HA solution were mixed and vortexed. Particles were isolated via centrifugation (5 min, 13000 rpm) and dispersed in 100 µL water.

2.2.13 Cell culture

The HeLa pLuc/705 and wild type cell lines were cultured in low glucose (1 g/L glucose) Dulbecco's Modified Eagle Medium (DMEM). DMEM medium was supplemented with 10 % FBS, 100 U/mL penicillin and 100 µg/mL streptomycin. Both cells lines were cultivated in ventilated flasks at 37 °C and 5 % CO_2 in a humidified atmosphere (relative humidity of 95 %).

2.2.14 Splice-switching and luciferase activity assay in vitro

HeLa pLuc/705 cells were seeded in 96-well plates with $5x10^3$ cells per well 24 h prior to transfection. A lipopeptide LP LenA (Y3-Stp2-K-ε[G-K-α,ε(linolenic acid)2]αStp2-Y3-K-ε(N3)) was used for coating of PNA-Zr nanoparticles which was previously used for conjugation with splice-switching phosphorodiamidate morpholino oligomers (PMOs) [219]. PNA-Zr particles were formed by same splice-switching PNA sequence and formulated with several stoichiometric amounts of LP LenA by 40 mins incubation in HBG before further dilution in HBG for application. The PNA content of nanoparticles was determined by disassembly of a small sample via competition with phosphate buffer (PBS) and photometric quantification of released PNA at 260 nm. The cell treatment was initiated by replacement of the medium with 90 µL fresh serum-containing DMEM and 10 µL PNA-Zr particles. As control 10 µL HBG was used. Cells were placed in an incubator with a relative humidity of 95 % at 37 °C and 5 % CO_2. After 48 h (or alternative incubation times as stated in kinetic studies), medium was removed and 100 µL of lysis buffer (12.5 mM tris(hydroxymethyl) aminomethane buffer (pH 7.8) with phosphoric acid, 1 mM dithiothreitol (DTT), 2 mM 1,2-diaminocyclohexane-N,N,N',N'-tetraacetic acid, 5 % glycerol, 0.5 % Triton® X-100; Promega, Mannheim, Germany) was added to each well. Cells were incubated in lysis buffer for 45 min at RT. From toughly mixed cell lysate, 35 µL was placed in measurement plates and luciferase activity was measured with addition of LAR buffer solution (20 mM glycylglycine, 1 mM $MgCl_2$, 0.1 mM EDTA, 3.29 mM DTT, 0.548 mM ATP (adenosine 5′-triphosphate), 0.28 mM coenzyme A stock solution, pH 8.0-8.5) with 10 % (v/v) of 10 mM luciferin and 29.375 mM glycylglycine. Measurements were performed with a Centro LB 960 plate reader luminometer (Berthold Technologies, Bad Wildbad, Germany). The relative light units (RLU) were normalized to HBG-treated cells and the results are presented as 'fold increase in luminescence'. All experiments were carried out in triplicates.

2.2.15 Metabolic activity

Cell viability of HeLa wild type cells were investigated via CellTiter-Glo® assay after treatment with PNA-Zr particles. HeLa pLuc/705 cells were seeded in 96-well plates with $5x10^3$ cells per well 24 h prior to transfection. Then, the medium was replaced with 90 µL fresh serum-containing DMEM and 10 µL of PNA-Zr particles was added to each well. After 48 h, medium was removed and 25 µL of DMEM and 25 µL of CellTiter-Glo® Reagent (Promega, Mannheim, Germany) were added to each well. Then, cell plates were incubated on a shaker for 30 mins at RT and viability was measured with a Centro LB 960 plate reader luminometer (Berthold Technologies, Bad Wildbad, Germany). Relative cell viability calculated by the following formula: cell viability [%] = mean(sample) / mean(control) × 100. All experiments were carried out in triplicates.

2.2.16 Reverse-transcription PCR (RT-PCR)

HeLa pLuc/705 cells were seeded in 24-well plates with $5x10^4$ cells per well 24 h prior to transfection. Then, the medium was replaced with 900 µL fresh serum-containing DMEM and 100 µL of particle suspensions with varied concentrations was added to each well. Cells were incubated for 48 h then medium was removed and total RNA isolation was performed with Tri-Reagent® (Sigma-Aldrich, Munich, Germany) according to the manufacturer's protocol. Then cDNA synthesis was done with 200 ng of the isolated RNA via cDNA synthesis with the High-Capacity cDNA Reverse Transcription Kit (Applied Biosystems, Munich, Germany) again according to the manufacturer's protocol. Standard PCR was carried out with 300 ng of cDNA using the HotStarTaq Plus DNA polymerase kit (QIAGEN, Hilden, Germany) and the following primers: 5'-

TTGATATGTGGATTTCGAGTCGTC-3' (forward) and 5'-TGTCAATCAGAGTGCTTTTGGCG-3' (reverse). PCR program was composed of an initial cycle at 95 °C for 5 mins, followed by 29 cycle of 95 °C for 30 seconds, 55 °C for 30 seconds, 72 °C for 30 seconds and finally one cycle at 72 °C for 10 mins. The RT-PCR product was analyzed via agarose gel electrophoresis (1.25 % agarose in TBE buffer containing GelRed®) at 90 V for 45 mins and was imaged on a Biostep Dark Hood DH-40 (Biotec-Fischer, Reiskirchen, Germay) with biostep argus onesoftware (Biotec-Fischer, Reiskirchen, Germay).

2.2.17 Calcein loading to PNA-Zr particles

PNA-Zr particles in ethanol were centrifuged and supernatants were removed. Then particles were resuspended in 1 mL 0.25 mM calcein in water and were incubated on a shaker for 15 mins at RT. Afterwards, the particles were centrifuged and washed three times with water, three times with ethanol and stored in ethanol. The amount of 50 to 100 µL of calcein labeled PNA-Zr suspensions were disassembled via competition with 1 mL PBS. Concentration of PNA and calcein content were determined photometrically by using extinction coefficient of specific PNA at 260 nm wavelength and extinction coefficient calcein at 515 nm. Data collection were performed with a Cary 3500 UV-Vis spectrophotometer.

2.2.18 Confocal laser scanning microscopy (CLSM)

To investigate calcein loaded particles, $2x10^4$ HeLa pLuc/705 cells in 300 µL DMEM medium were seeded in 8 well-Ibidi µ-slides (Ibidi GmbH, Munich, Germany). Cells were incubated at normal cell culture conditions (37 °C and 5 %

CO_2) for 24 h. Then medium was removed and 240 µL fresh medium and 60 µL calcein loaded PNA-Zr particle solution was added to each well. Cells were incubated for 4 h with particles then solution was removed and incubation was continued with fresh medium for 4 h. Then, cells were washed with PBS and fixated with 300 µL/well 4 % paraformaldehyde for 45 mins at RT. After fixation, wells were washed again twice with PBS and stored in PBS at 4 °C. Cell staining was performed by incubation for 30 mins (at RT light protected environment) with 300 µL PBS solution containing DAPI (2 µg/mL) for staining of nuclei and phalloidine-rhodamine (1 µg/mL) for staining of actin cytoskeleton. Staining solution was removed and replaced with 300 µL PBS.

To assess the effect of LP LenA coated particles on endosomal membrane integrity, HeLa mRuby3/gal8 cells were used, which are based on the plasmid PB-CAG-mRuby3-Gal8-P2A-Zeo provided by Jordan Green (Addgene plasmid # 150815 ; http://n2t.net/addgene:150815 ; RRID:Addgene_150815). For the experiment, $2x10^4$ HeLa mRuby3/gal8 cells in 300 µL DMEM medium were seeded in 8 well-Ibidi µ-slides. Cells were incubated at 37 °C and 5 % CO_2 for 24 h. Then medium was removed and 270 µL fresh medium and 30 µL of LP LenA coated (1/1.25 molar ratio) and uncoated 705 SSO-Zr particle suspensions containing 25 µM PNA were added to each well. Cells were incubated for 8 h with particles then the solutions were removed and incubation was continued with fresh medium for 4 h. Then, cells were washed with PBS and each well was fixated with 300 µL 4 % paraformaldehyde for 45 mins at RT. After fixation, wells were washed again twice with PBS and stored in PBS at 4 °C. Staining of nucleic was performed by incubation for 30 mins (at RT light protected environment) with

300 µL PBS solution containing DAPI (2 µg/mL). Staining solution was removed and replaced with 300 µL PBS.

Images were taken by Leica-TCS-SP8 CLSM equipped with an HC PL APO 63x 1.4 objective with LAS X software from Leica (Leica Microsystems, Wetzlar, Germany). Emissions were recorded at following wavelengths: DAPI at 460 nm, calcein at 530 nm, phalloidine-rhodamine at 580 nm and mRuby3 at 585 nm. CLSM imaging was performed by Miriam Höhn (LMU Pharmaceutical Biotechnology).

2.2.19 Statistical analysis

Results are presented as arithmetic mean ± standard deviation. If not otherwise stated, significance levels were evaluated by two-tailed t-test (unpaired). The following symbols were used to indicate significance levels (*p ≤ 0.05, **p ≤ 0.01, ***p ≤ 0.001 and ****p ≤ 0.0001) and not significant was labeled as ns.

3. Results and Discussion

This chapter has been adapted from:

Öztürk Ö., Lessl A., Höhn M., Wuttke S., Nielsen P., Wagner E., Lächelt, U., Peptide Nucleic Acid – Zirconium Coordination Nanoparticles. Manuscript to be submitted.

3.1 Design of Peptide nucleic acid – zirconium coordination nanoparticles (PNA-Zr)

The design and selection of suitable organic linkers is a key step in MOF synthesis and critically impacts the MOF properties and characteristics after assembly. The linkers require Lewis base functions containing N- or O-donor atoms such as carboxylic acids or aromatic N-heterocycles. Most established MOF linkers possess a rigid structure with constricted flexibility due to unsaturated bonds, cycles or arenes connecting the separated Lewis base functions. In order to establish a platform for the creation of PNA based coordination nanoparticles, different PNA linker architectures were designed to mimic characteristics of established MOF linkers: (1) aromatic carboxylic acids were attached at the PNA termini to provide Lewis base functions at distant positions; (2) single- and double-stranded PNAs were used to modulate the linker rigidity. Unfortunately, most common MOF syntheses under solvothermal conditions were not found compatible with double-stranded PNAs, since PNA duplexes melt and dissociate at the required high temperatures. Therefore, a strategy for MOF synthesis at room temperature had to be chosen. The group of Omar Farha developed a RT synthesis of UiO-66, which is constructed from hexanuclear zirconium oxide clusters ($Zr_6O_4(OH)_4$) and terephthalic acid (TPA) [110]. In this strategy, classical one-pot solvothermal MOF synthesis is dissected into the sequential steps of (1) preforming secondary building units from zirconium propoxide [$Zr(OnPr)_4$] at high temperatures in presence of excessive acetic acid, followed by (2) addition of the TPA linker and incubation at RT. This work served as basis for the adaption towards Zr-coordination nanoparticles with temperature sensitive PNA linkers.

The strategy for the formation of the particles is illustrated in Figure 6A. Analog to the work by DeStefano et al.[110], coordination particles are formed in a two-step process. First, Zr nodes are generated by incubating the solution containing $Zr(OnPr)_4$, DMF and acetic acid at 130 °C for 2 h. Then the solution of metal nodes was cooled to RT and added to a PNA linker dissolved in DMF solution at a 1/1 molar ratio of linker to Zr. In case of double-stranded or palindromic PNA linkers, an initial annealing step (Heating to 90 °C then cooling to RT in water and freeze-drying with acetonitrile) was carried out to ensure duplex formation. The assembly mixture was incubated for 24 h at RT and the formed PNA-Zr particles were separated by centrifugation as a white precipitate.

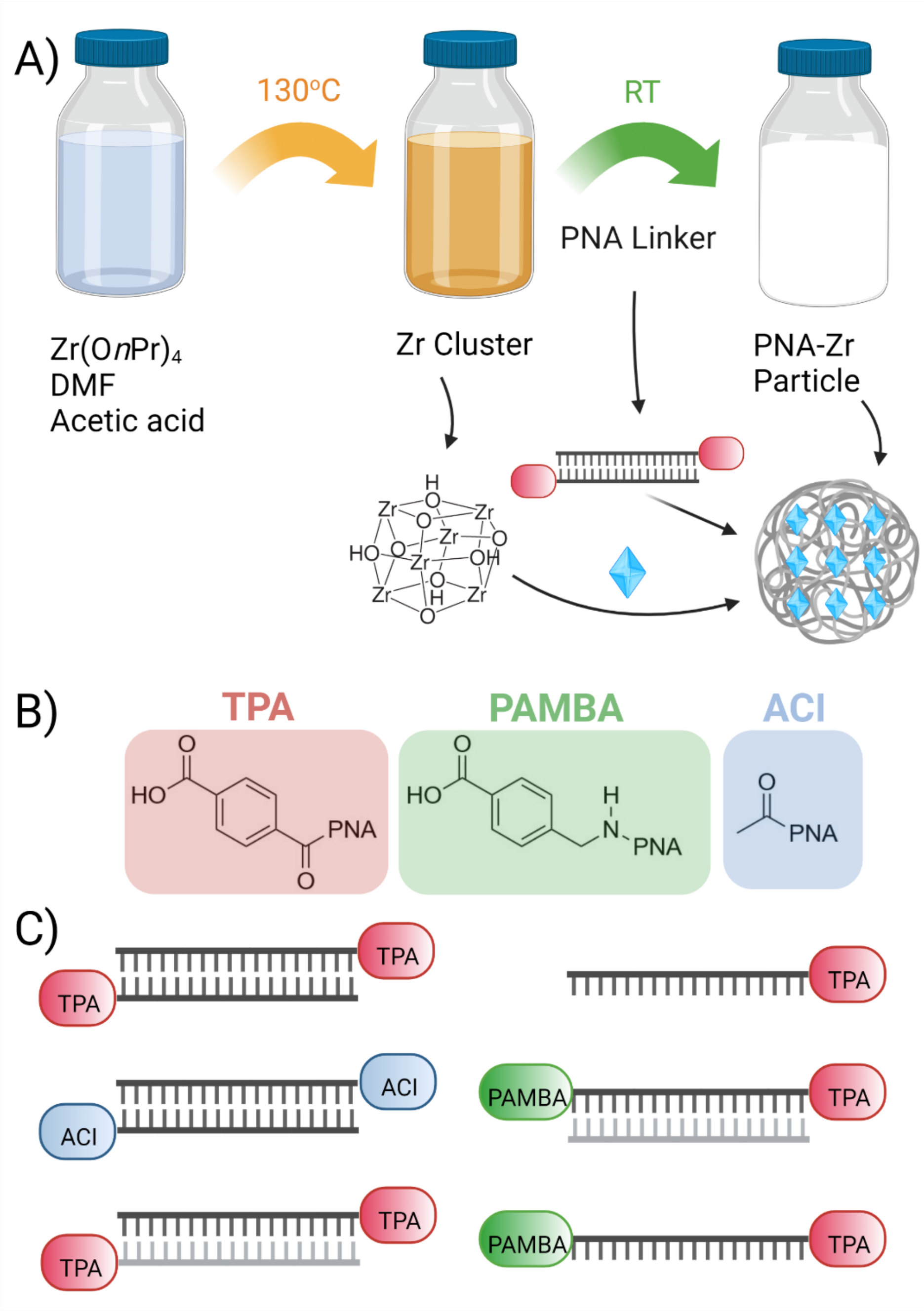

Figure 6 Synthesis process, modifications and architectures. **A)** Synthesis of PNA-Zr particles via a two-step process. **B)** PNA end-modifications: left terephthalic acid (TPA, red), center para-aminomethylbenzoic acid (PAMBA, green) and right acetic acid (ACI, blue). **C)** PNA linker architectures. Created by BioRender.com (2022).

As illustrated by Figure 6C, several PNA linkers with different modifications were designed; *para*-aminomethylbenzoic acid (PAMBA) and terephthalic acid (TPA) end modifications were introduced at the C- (PAMBA) and N- (TPA) termini of PNA sequences to serve as aromatic carboxylic acid functions for coordinative interactions with metal nodes. In contrast, acetylated (ACl) N-termini served as controls without Lewis base function. Table 3 summarizes the PNA sequences that were evaluated and the capability to serve as linkers for particle formation with Zr nodes. It is important to note, that PNA linkers generally were purified by size exclusion chromatography without acid additives in the solvent, since it was observed, that HCl salts of PNAs negatively affect particle formation. Palindromic PNA sequences with modification of the N-terminus (TPA or ACl), which assemble into duplexes due to self-complementarity, served as simple models of double-stranded linkers. The shortest palindromic sequence that formed particles with Zr nodes exhibited a length of 6 PNA monomer units, but only if the N-terminus was modified with TPA. In contrast, palindromic 4- and 2-mers did not form particles regardless of TPA or ACl end-modifications. It is suggested, that the low melting temperature (lower than room temperature) of the shorter PNA sequences is responsible for a lack of dimerization and formation of linkers with two coordinative end functionalities [220]. The observation, that acetylation generally prevented particle formation with Zr nodes indicates the need of TPA as Lewis base end modification. Consistently, the combination of two complementary, non-palindromic 6-mer PNAs with TPA at the N-termini was also able to form particles, but an exact 1/1 molar ratio of both PNAs was essential.

Table 3 Summary of investigated PNA linkers. The linkers are composed of either double-stranded (ds) or single strand (ss) PNA architectures. Successful particle formation is indicated by 'YES' (observed) or 'NO' (not observed).

PNA Linker	Description	Architecture	Particle Formation
GC-ACI	palindromic	ds	NO
GC-TPA	palindromic	ds	NO
CATG-ACI	palindromic	ds	NO
CATG-TPA	palindromic	ds	NO
GCATGC-ACI	palindromic	ds	NO
GCATGC-TPA	palindromic	ds	YES
CAGTACTG-ACI	palindromic	ds	NO
CAGTACTG-TPA	palindromic	ds	YES
CGTGAC-TPA + GTCACG-TPA	non-palindromic	ds	YES
CGTGAC-TPA + GTCACG	non-palindromic	ds	minor formation
PAMBA-CGTGAC-TPA + GTCACG	non-palindromic	ds	YES
PAMBA-CGTGAC-TPA	non-palindromic	ss	YES
PAMBA-GCAGCT-TPA	non-palindromic	ss	YES
PAMBA-CCTCTTACCTCAGTTACA-TPA	non-palindromic (705 SSO)	ss	YES

PNA sequences equipped with two metal coordination sites at the N- (TPA) and C- (PAMBA) terminus were suitable for particle formation, independent whether it was used as duplex with an additional complementary strand (without PAMBA and TPA) or as single-stranded linker alone. Interestingly, the combination of a PNA sequence with one TPA at the N-terminus and the complementary PNA without modification, which theoretically leads to a double-stranded PNA with only one aromatic carboxylic acid end function, caused a slight particle formation. Although in this case the particle yield was low compared to linkers with two TPA or PAMBA and TPA, this result could eventually be explained by a certain extent of PNA triplex formation, which again could lead to linkers with two TPA functions at both sides [221].

3.2 Characterization of PNA-Zr particles

The obtained PNA-Zr particles were characterized by a set of physicochemical analytics. Particle size, appearance and surface charge were determined by SEM and DLS. Representative SEM images (Figure 7) show small (between 150-250 nm diameter) and mostly spherical particles formed with different PNA linkers. DLS measurements (Figure 8) showed larger particles with z-averages between 500 nm to 1000 nm. The deviation can be explained by a high sensitivity of DLS towards aggregates and larger particles as well as the fact that DLS detects particle hydrodynamic diameter in solution, whereas SEM measurements are carried out with dried samples.[222] Electrophoretic light scattering measurements determined negative zeta potentials between -5 to -10 mV. Having negative zeta potential was a good indicator for proper particle formation. Failed particle formations were observed to have neutral zeta potential.

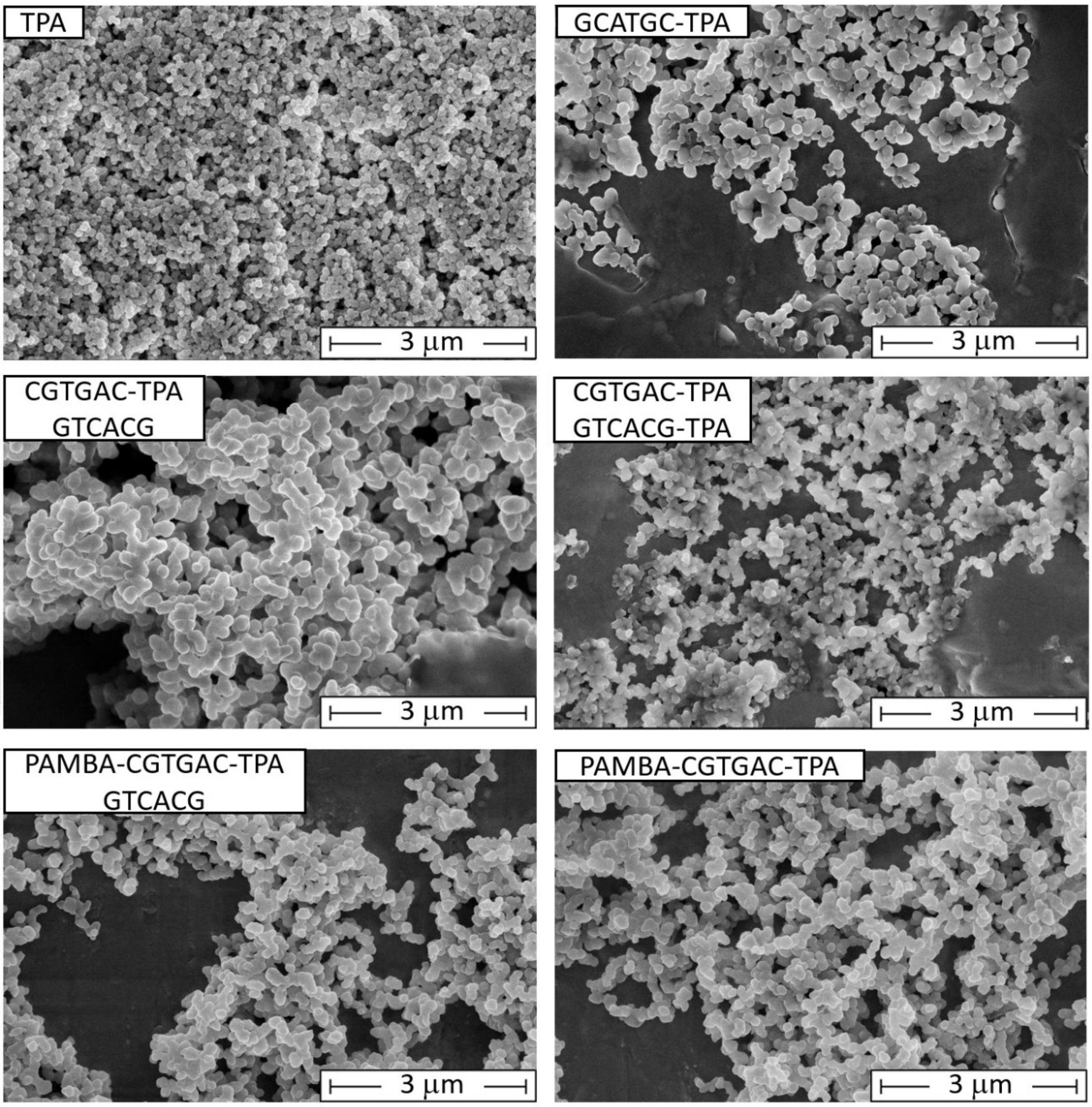

Figure 7 Representative SEM images of PNA-Zr nanoparticles. The sequences of individual PNA linkers is specified in the upper left corner of the images. TPA leading to the formation of UiO-66 was used as a reference (Scale bars = 3 µm). Images were taken by Dr. Steffen Schmidt (LMU Munich, Germany).

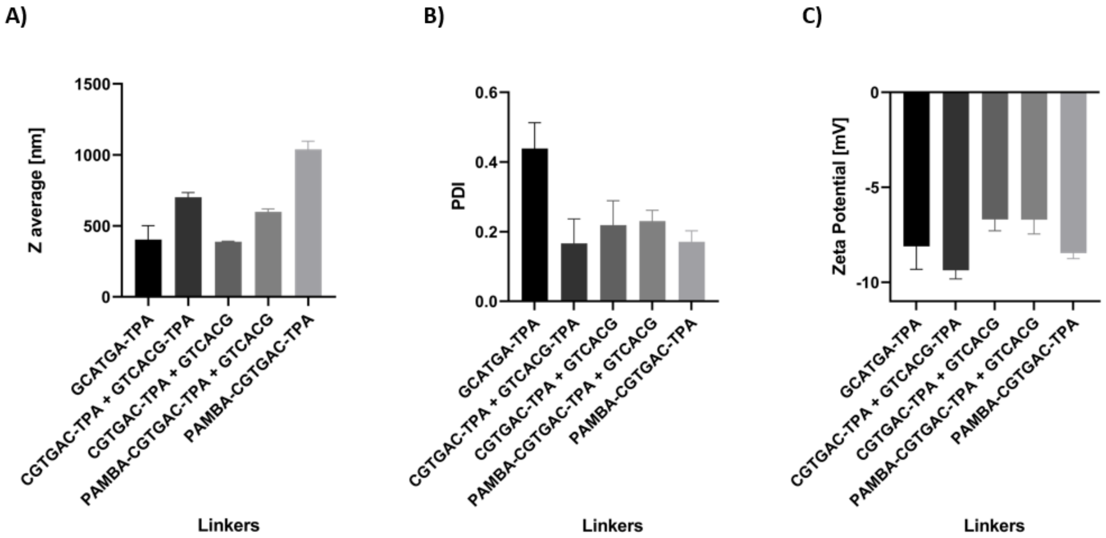

Figure 8 DLS and ELS of PNA-Zr particles. Linkers are specified below each bar. **A)** Z-average in nanometers (measured in water). **B)** Polydispersity index (measured in water). **C)** Zeta potential in millivolt (measured in 10 mM NaCl).

Thermal stability of PNA-Zr particles were investigated by monitoring the optical density (400 nm) of nanoparticle suspensions exposed to a temperature gradient in water. Particles formed a turbid suspension that scatters light at a variety of wavelengths. Any wavelength between 300 nm to 600 nm can be used. In general, turbidity or light scattering measurements are carried out at a wavelength in the visible spectrum (400 nm), which does not overlap with absorption maxima of individual components. PNAs, similar to other nucleic acid analogs, have an absorption maximum in the UV spectrum at 260 nm [223, 224]. As seen in Figure 9A, PNA-Zr particles are stable at RT regardless of the PNA linker architecture. At higher temperatures, particles assembled from double-stranded linkers with single TPA modifications on both strands disassemble at elevated temperatures, which can be recognized as drop of the optical density. A reasonable explanation is, that the PNA duplexes melt at the increased temperatures, which results in disassembly of the linkers with TPA function on both ends. In contrast, particles containing linkers with PAMBA and TPA in a single strand did not show similar temperature sensitivity. These results suggest three key characteristics of the PNA-Zr nanoparticles: (1) two aromatic carboxylic acid functions, located at both ends of the PNA linkers, are essential; (2) linker can be composed of double or single strand of PNA as long as two carboxylic acid functions were present; and (3) double-stranded linkers with two aromatic carboxylic acid functions separated on both strands are sensitive towards linker disassembly via duplex melting. The stability of PNA-Zr particles in biological buffers, isohydric HEPES (20 mM, pH 7.4) as well as isohydric and isotonic HBG (20 mM HEPES, pH 7.4, 5% glucose), was investigated with the same approach (Figure 9B and C). PNA-Zr particles were added to either HBG or HEPES and the optical density was monitored at 400 nm over time. Similar to the results of the thermal stability study, particles containing linkers with two aromatic carboxylic acid functions in a single PNA strand exhibited higher stability, whereas particles composed of double-stranded linkers with TPA modifications in separate strands dissociated.

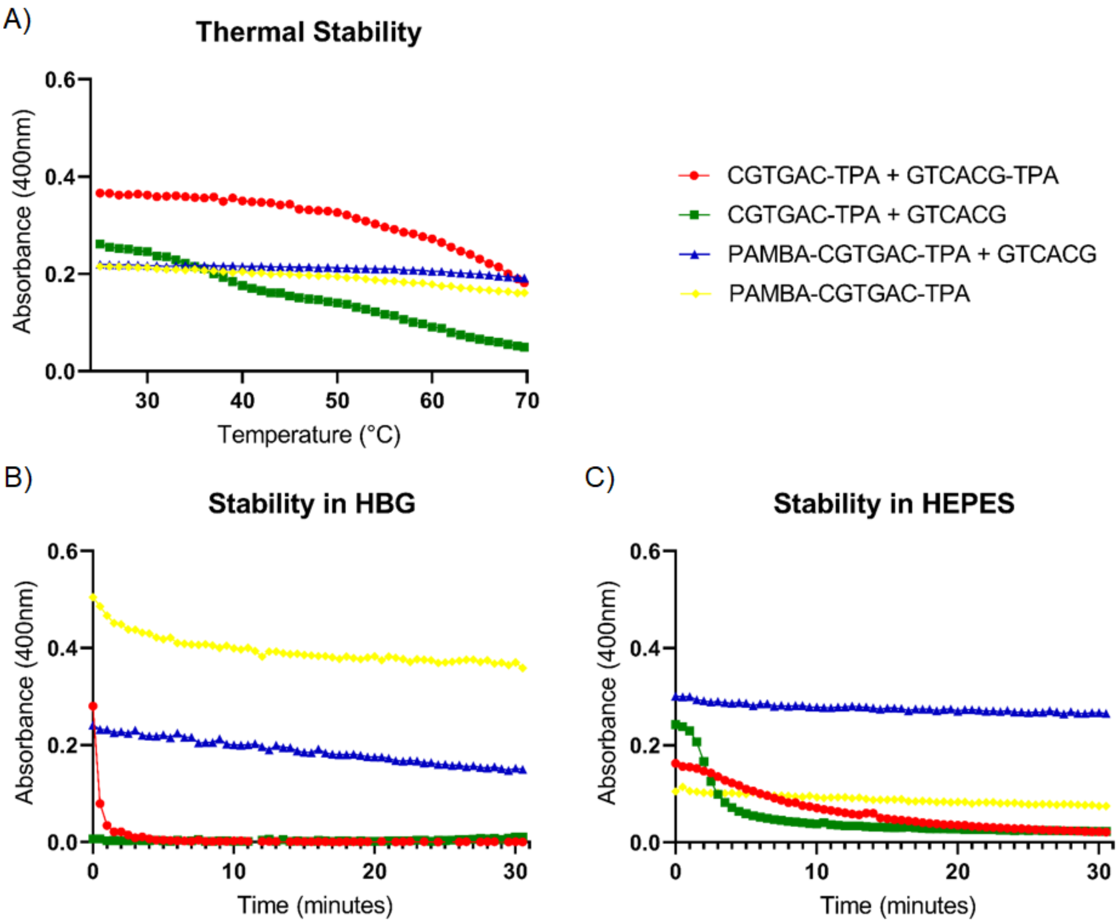

Figure 9 Stability of PNA-Zr particles determined by measurement of optical density (400nm) **A)** at increased temperatures or after incubation in **B)** HBG, **C)** HEPES. PNA linker architectures are indicated by colors.

The utilization of coordination modulators is an effective way to adjust crystallinity or size of the particles and one such competing modulator TPA can be used to regulate crystallinity and size of UiO-66 MOFs [225, 226]. In similar way concentration of starting martials also affects MOF morphology [227]. To investigate possible ways to improve stability without changing architecture of the linker, representative palindromic GCATGC-TPA linker was utilized with one eq of TPA as modulator or at lower linker concentration during particle formation (10-

fold dilution in DMF). As seen in Figure 10, SEM images showed that both modulation and dilution methods had a significant effect on particle size, decreasing size from approximately 200 nm to 150 nm. This was expected as both methods slowdown the particle formation. However, possible stability improvement caused by slower formation was not observed. The differently formed PNA-Zr particles showed similar stability characteristic in HBG as the regularly formed particles (Figure 11A).

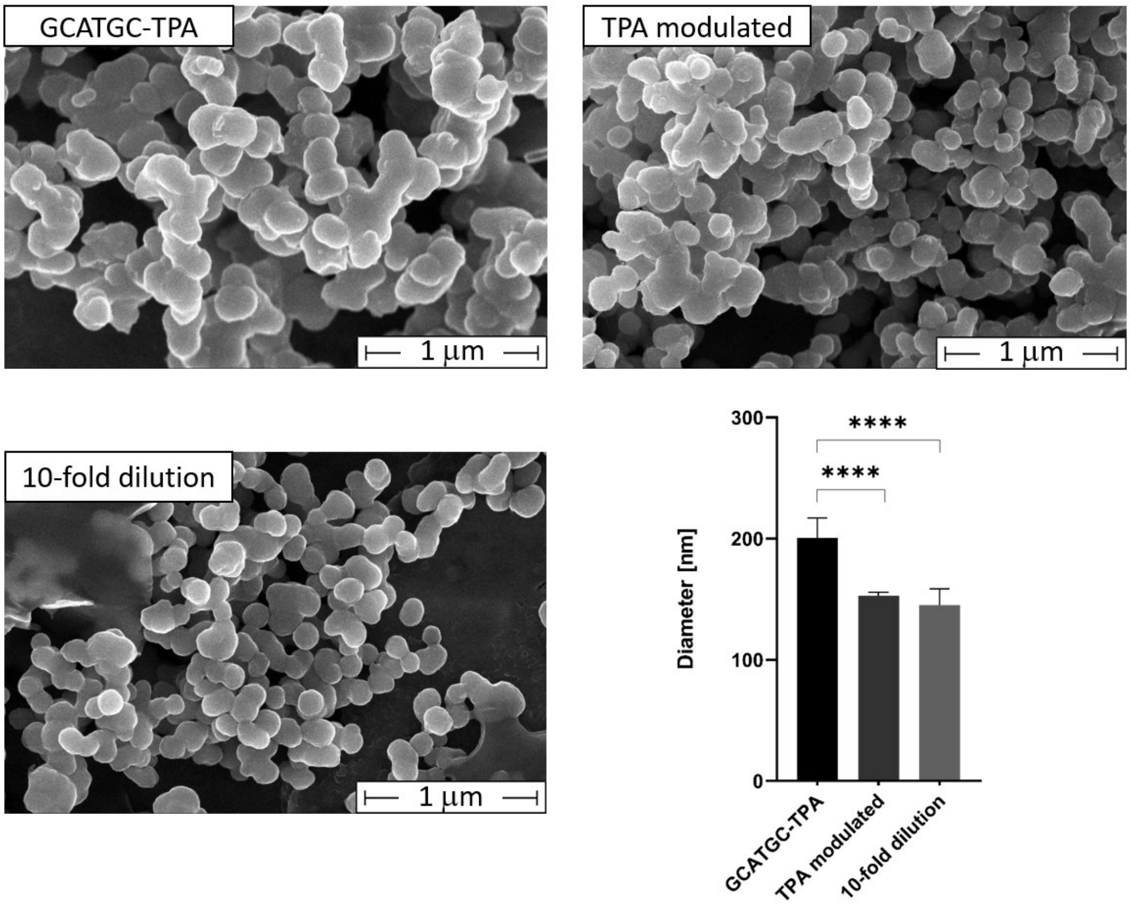

Figure 10 Representative SEM images of PNA-Zr nanoparticles with different particle formation methods (Top left corner; standard protocol, top right corner; additional 1 eq TPA in solution; bottom left corner, 10 fold increased solvent volume). For all cases GCATGC-TPA linker was utilized (scale bars = 2 µm). Images were taken by Dr. Steffen Schmidt (LMU Munich, Germany). The graph shows

evaluation of particles sizes obtained from SEM imaging (diameter, nm). n=40 random particles were evaluated for the determination.

Particle coating is another way to increase stability of coordination polymers. Both DOPC and HA coating have previously been shown to increase stability of coordination polymers against physiological conditions [228-230]. Effects of different coating strategies on stability in HBG was investigated with palindromic GCATGC-TPA linker (Figure 11B). Unfortunately, both HA (20 kDa) and HA (100 kDa) did not improve particle stability. DOPC coating on the other hand lead to slightly more stable particles in HBG. However, neither particle coating strategies nor modified particle formation methods, resulted in stability improvements comparable to the stability of particles generated from linkers possessing two aromatic carboxylic acid functions in one single PNA strand.

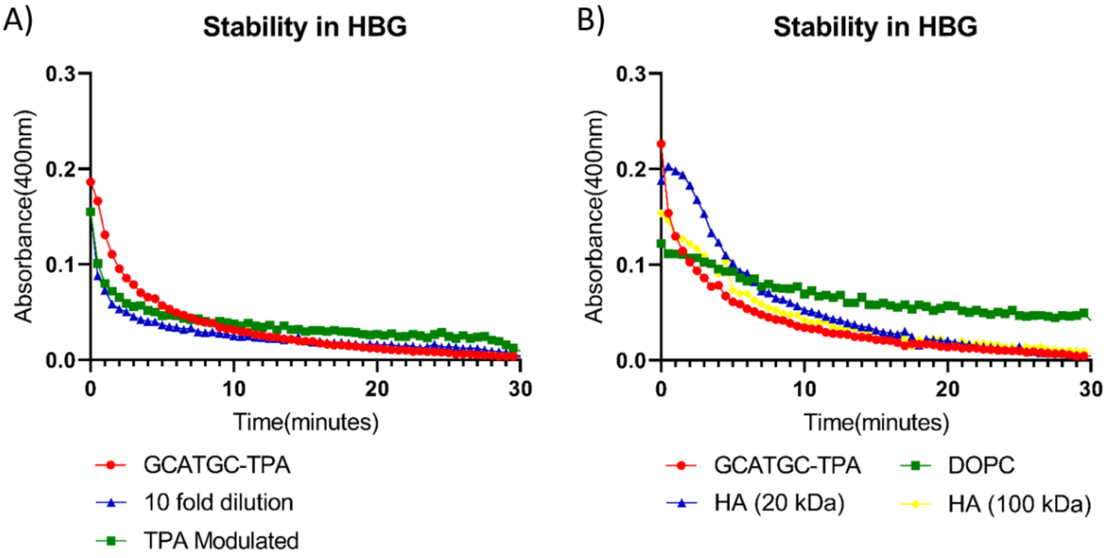

Figure 11 Stability of PNA-Zr particles determined by measurement of optical density (400nm) in HBG **A)** Different particle formation methods. **B)** Different coating methods. GCATGC-TPA linker was used. Different methods and coatings are indicated by colors.

XRD was used to elucidate the presence of crystalline structures in representative PNA-Zr nanoparticles built from double-stranded (palindromic GCATGC-TPA) or single-stranded (non-palindromic PAMBA-CGTGAC-TPA) linkers (Figure 12). In contrast to the characteristic reflections obtained for UiO-66, no indication for crystallinity of PNA-Zr NPs was found by XRD; therefore, rather amorphous structures of PNA-Zr coordination polymers are suggested. Further characterization by nitrogen sorption determined a surface area of 300 m²/g for PNA-Zr NPs built from GCATGA-TPA and 36 m²/g for NPs with PAMBA-CGTGAC-TPA (Table 4) [231]. The absorption isotherm of PAMBA-CGTGAC-TPA showed similarity to a type II absorption isotherm indicating a non-porous or macro-porous structure, whereas GCATGA-TPA could not be assigned to any characteristic type [232, 233].

Table 4 Nitrogen sorption results of PNA-Zr particles. Surface areas of the samples were calculated according to the linearized BET equation.

Linkers	**Correlation coefficient**	**C constant**	**Surface Area (m²/g)**
TPA	r =0.999850	356.95	1260.79
GCATGC-TPA	r = 0.999352	2.68	300.53
PAMBA-GCAGCT-TPA	r =0.999454	28.07	35.84

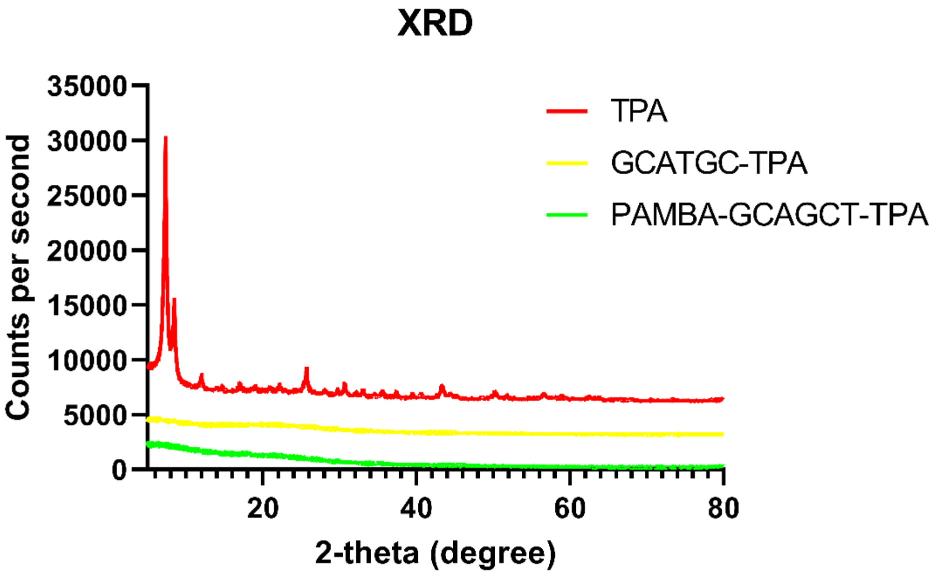

Figure 12 XRD of metal-organic nanoparticles based on different linkers: TPA (red), double-stranded palindromic GCATGC-TPA (yellow) and single-stranded PAMBA-GCAGCT-TPA (green). TPA curve was shifted by 6000 counts, GCATGC-TPA curve by 3000 counts to enable direct comparison.

Next, the Zr content of PNA-Zr particles was determined by inductively coupled plasma atom emission spectrometry (ICP-AES, Figure 13). A content of 52 mg/g Zr was determined for PAMBA-CGTGAC-TPA particles and 31 mg/g Zr for GCATGA-TPA particles. Based on the obtained results and the molecular weights of PNA linkers, the molecular ratio composition of the particles was calculated. Molar ratios of Zr to linker of around 1.2/1 were determined for both representative types of PNA-Zr nanoparticles, which is close to the 1/1 ratio reported for UiO-66 [234].

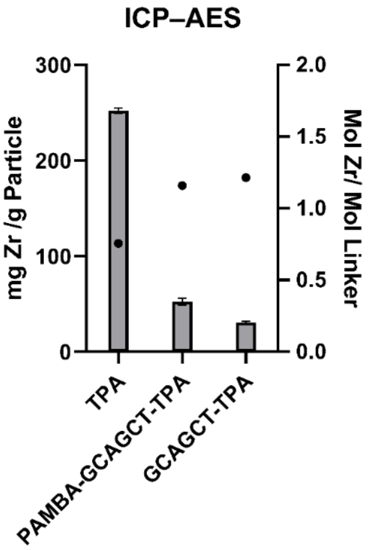

Figure 13 Zr content of PNA-Zr particles determined by ICP-AES and resulting molar ratios calculated under consideration of the molecular weight of the linkers.

3.3 CLSM of calcein loaded particles

The fluorescent dye calcein, which contains Lewis base functions and can form chelates with metal ions, was utilized for labeling of PNA-Zr particles by coordinative interaction [58, 235]. For this, PNA-Zr particles were incubated with an aqueous calcein solution (0.25 mM) at RT. At the end of the labeling procedure, a clear color change from white to orange particles was observed (Figure 14A). Direct comparison of labeled and unlabeled PNA-Zr particles in the established stability assay confirmed that calcein loading did not affect the stability characteristic in HBG (Figure 14B). Calcein-loaded PNA-Zr particles based on GCATGA-TPA, degraded within one hour in HBG, while PAMBA-CGTGAC-TPA particles did not show significant particle disassembly. Subsequent ELS measurement showed that overall charge of the calcein loaded particles were still negative (Figure 15).

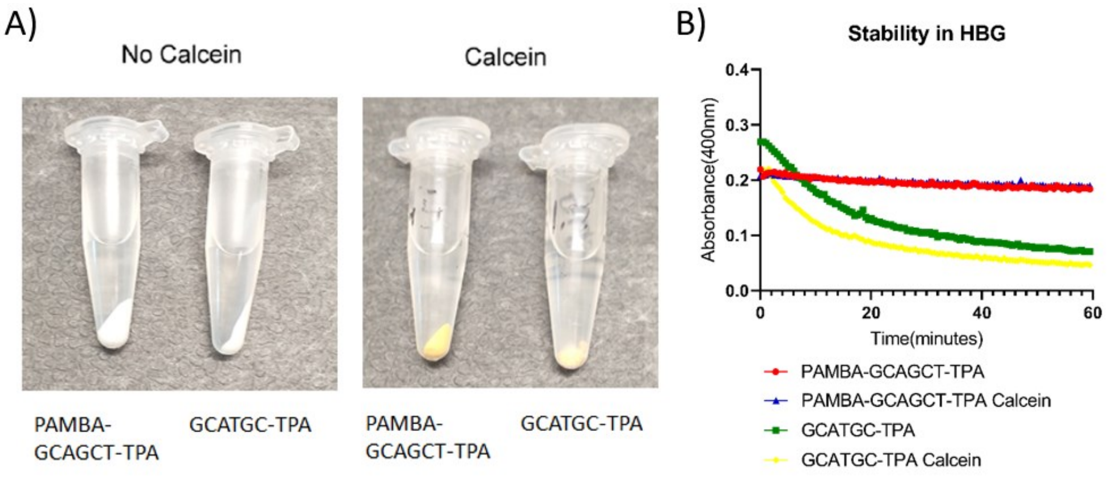

Figure 14 Physical appearance of calcein loaded particles and loaded particle stability. **A)** Representative images of PNA-Zr particles before and after calcein loading. **B)** Stability of calcein loaded and unlabeled PNA-Zr particles in HBG as determined by measurement of optical density (400nm).

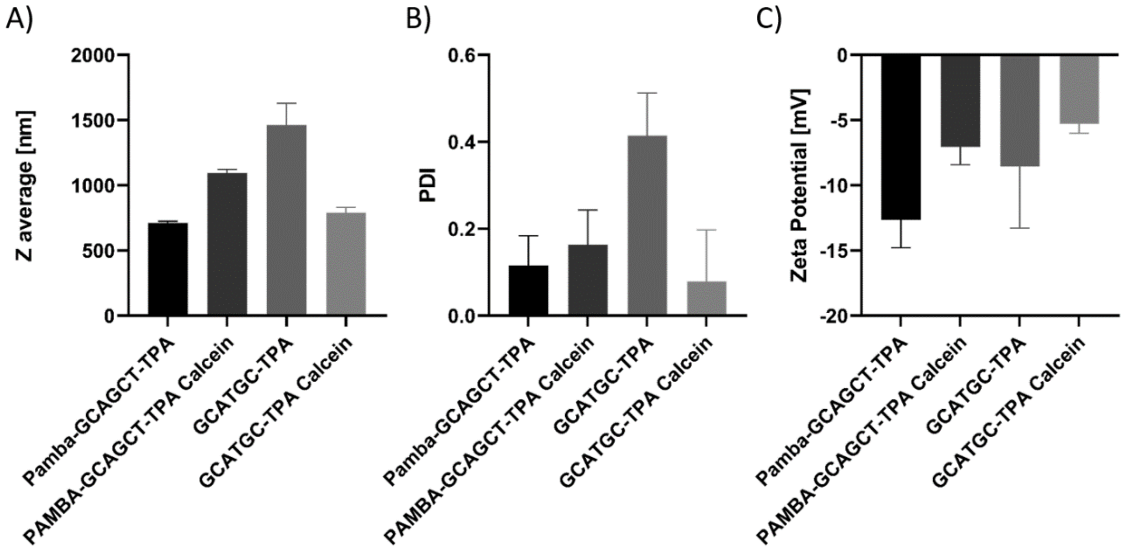

Figure 15 DLS and ELS of calcein loaded PNA-Zr particles. Linkers are specified below each bar. **A)** Z-average in nanometers (measured in water). **B)** Polydispersity index (measured in water). **C)** Zeta potential in millivolt (measured in 10 mM NaCl).

Further, the nanoscopic appearance of labeled and unlabeled PNA-Zr particles was compared by SEM imaging. As seen in Figure 16, calcein loading did not significantly impact the size and shape of the particles.

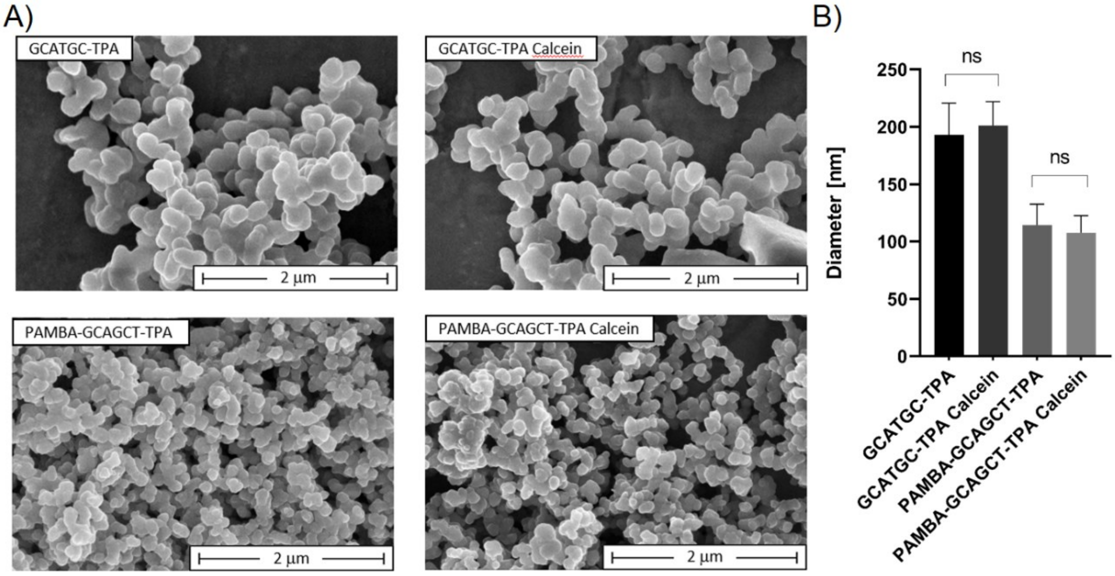

Figure 16 A) Representative SEM images of calcein loaded and unlabeled PNA-Zr nanoparticles. The individual linkers used for particle assembly are stated in the upper left corner of each image (scale bars = 2 µm). Images were taken by Dr. Steffen Schmidt (LMU Munich, Germany). **B)** Evaluation of particles sizes obtained from SEM imaging (diameter, nm). n=30 random particles were evaluated for the determination.

These results showing unaffected particle properties were essential requirements for the following determination of cellular uptake via CLSM imaging of calcein-loaded PNA-Zr nanoparticles (Figure 17). HeLa pLuc/705 cells were incubated for 4 h with labeled particles based on double-stranded palindromic GCATGA-TPA or single-stranded PAMBA-CGTGAC-TPA linkers, followed by a medium change and additional 4 h incubation. CLSM imaging showed that both types of

PNA-Zr nanoparticles were internalized by the cells, whereas free calcein could not be detected intracellularly. As the zeta potential, SEM size and stability characteristics of the calcein loaded particle were similar to normal particles, it is assumed that "naked" PNA-Zr particles behave similarly. This indicates, that PNA-Zr nanoparticles are suitable for the intracellular transport of impermeable compounds and that the particles did not dissociate in the cell culture medium.

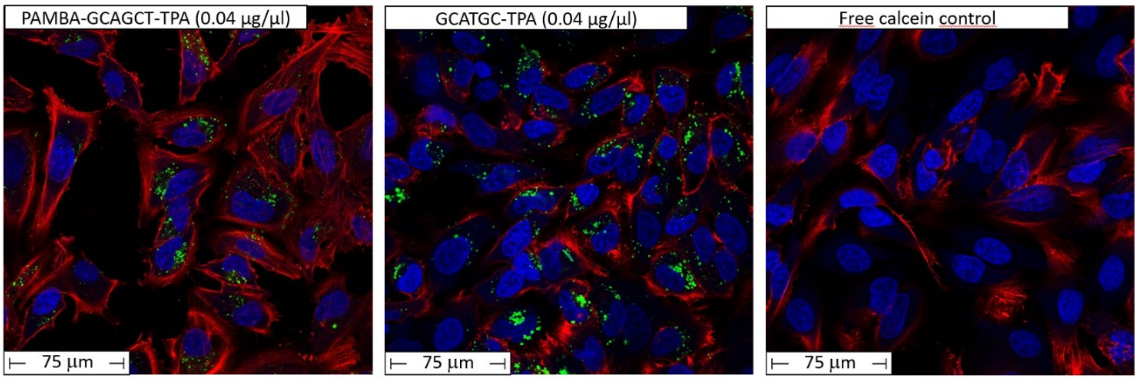

Figure 17 CLSM images of HeLa pLuc/705 cells treated with calcein loaded PNA-Zr particles (left PAMBA-GCAGCT-TPA, middle GCATGC-TPA, right free calcein control). HeLa pLuc/705 cells were incubated for 4 hours with calcein loaded particles (0.04 µg/ µL) or free calcein at the concentration corresponding to the maximal calcein content of particles (0.0005 µg/ µL). Subsequently, the cells were incubated for additional 4 hours with fresh medium before imaging. Staining and imaging done by Miriam Höhn (LMU Pharmaceutical Biotechnology).

3.4 Evaluation of biologically functional PNA-Zr particles

PNAs can strongly bind with high sequence specificity to complementary oligomers of DNA, RNA or PNA. They also have good mismatch sequence discrimination and resistance to nucleases and proteases which make them potential tools for molecular biology [200-204]. Since PNA can be utilized as antisense oligonucleotides which modulate the cellular mRNA splicing process, the capability of the PNA-Zr coordination nanoparticles to transport functional splice-switching PNAs into cells was assessed. Kang et al. generated HeLa cells with stable expression of a luciferase reporter (pLuc/705) for detecting corrections of aberrant β-globin splicing. The cell line contains a luciferase reporter gene that is disturbed by the β-globin intron containing mutation (IVS2-705) resulting in aberrant splicing of luciferase pre-mRNA. Sequence based targeting of the aberrant splicing site corrects the splicing and increases luciferase activity (Figure 18) [213, 214]. Here, we generated PNA-Zr particles containing the PNA sequence against the location of IVS2-705, which is able to induce splicing correction, if delivered into the nucleus of cells. With this test system, successful cellular delivery and splice-switching activity can be detected via bioluminescence due to the induction of functional luciferase expression [214, 219].

A single-stranded PNA linker with the sequence PAMBA-CCTCTTACCTCAGTTACA-TPA (705 SSO) has been used for particle formation via the established two step formation process. HeLa pLuc/705 cells were treated with the PNA-Zr NPs and the occurrence of splice-switching was assessed by determination of luciferase activity via bioluminescence measurements after 48 h. In preliminary experiments, the bare PNA-Zr particles were not able to mediate detectable splicing correction. Since cellular uptake of PNA-Zr particles was demonstrated previously, insufficient endosomal escape, which generally represents a critical hurdle for the delivery of biomacromolecules, was suspected to be responsible. To improve the endosomal escape and enable transport to the intracellular target sight, PNA-Zr particles were coated with a cationic oligomer (Figure 19B). The LP LenA (Y3-Stp2-K-ε[G-K-α,ε(linolenic acid)2]αStp2-Y3-K-ε(N3)) is a sequence-defined cationic oligomer which was previously shown to be a suitable agent for the delivery of splice-switching PMOs into HeLa pLuc/705 cells after covalent conjugation (Figure 19A) [219]. In the previous work, LP LenA was found to mediate a favorable endosomal release of PMO conjugates, presumably due to endosomal membrane interactions of the contained unsaturated linolenic acid residues.

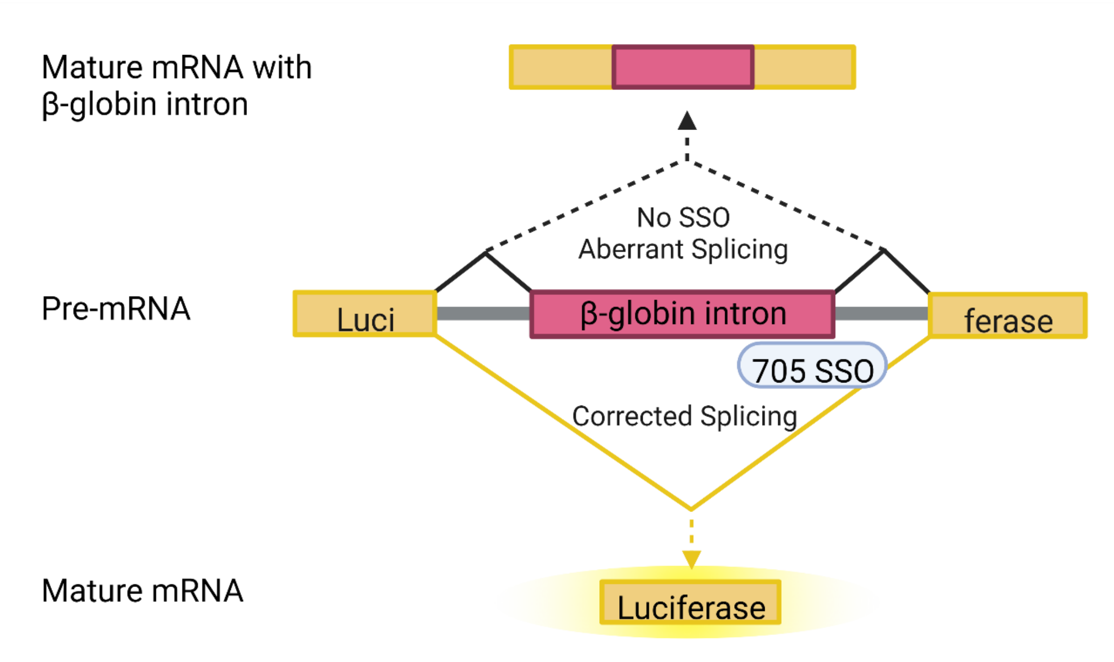

Figure 18 Schematic illustration of PNA assisted splicing correction in HeLa pLuc/705 cells. The pre-mRNA contains a ß-globin intron with a mutation (IVS2-705) resulting in aberrant splicing (indicated by black lines). PNA targeted to the splice site blocks aberrant splicing resulting in functional luciferase mRNA (indicated by yellow line) [213, 214]. Created with BioRender.com (2022).

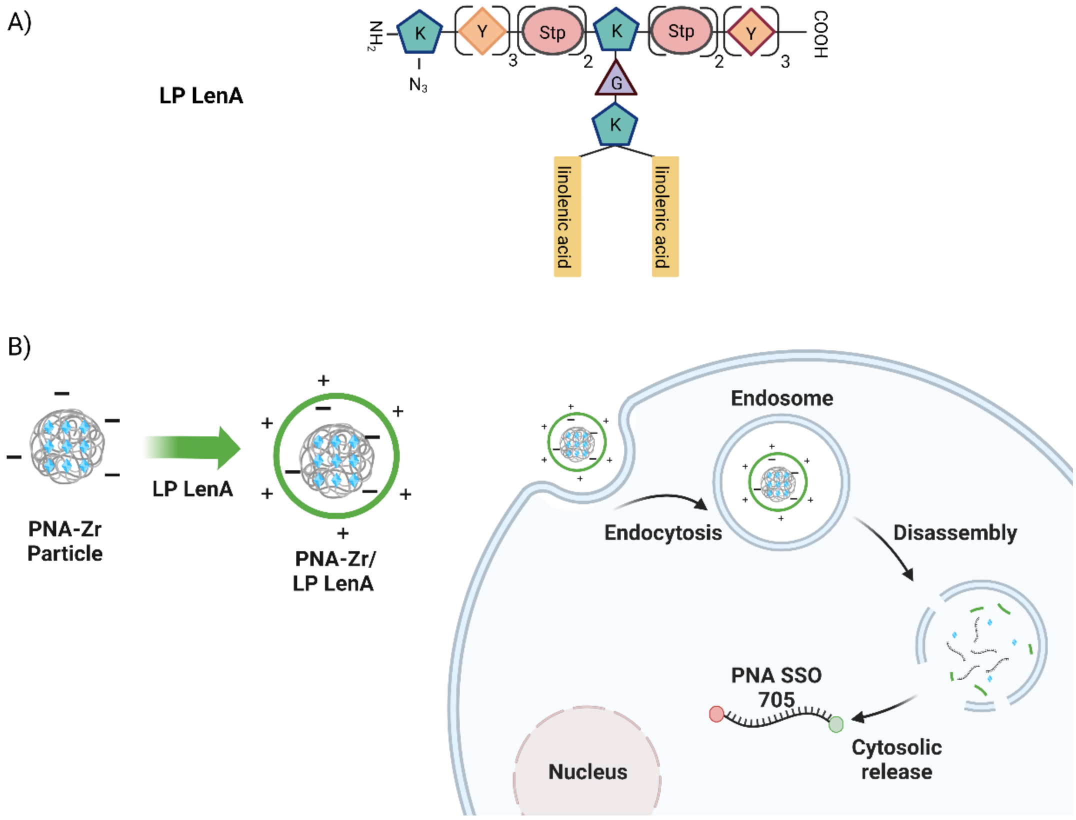

Figure 19 Structure of LP LenA and illustration intracellular delivery process. **A)** Structure of LP LenA composed of: N-terminal azidolysine, tyrosine (Y), lysine (K), succinyl-tetraethylenepentamine (Stp), glycine (G) and linolenic acid [219]. **B)** Schematic illustration of LP-LenA coated PNA-Zr nanoparticles and the intracellular delivery process. Created with BioRender.com (2022).

SEM imaging confirmed, that particles could be successfully assembled with the relatively long PNA linker (Figure 11A). The resulting particles were mostly spherical and exhibited small sizes between 150-250 nm in diameter. After surface coating with LP LenA, the spherical shape was preserved, though a slight increase in size seemed to be observable. The successful modification of the 705 SSO-Zr nanoparticle surface with LP LenA was further confirmed by zeta potential measurements, which determined a distinct shift from negative (-12mV) to positive zeta potential (+28 mV) after coating (Figure 20D).

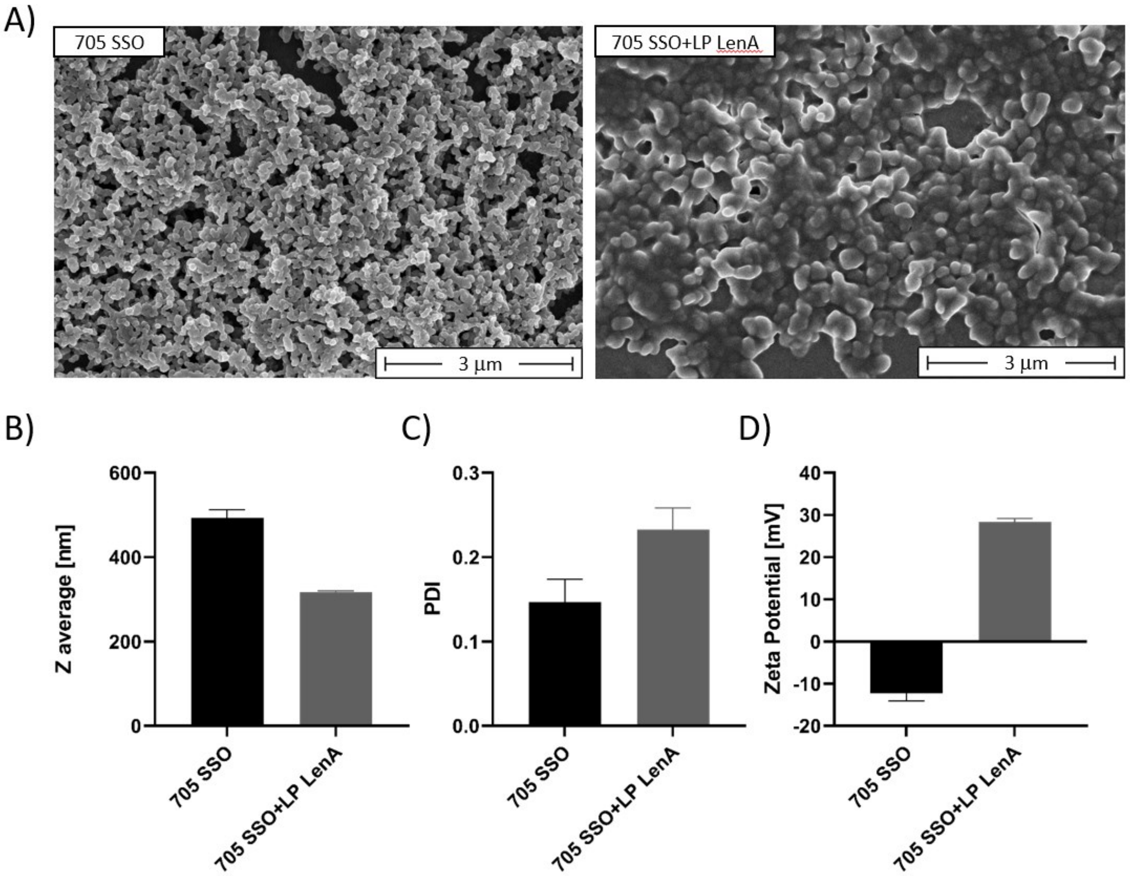

Figure 20 SEM, DLS and ELS of LP LenA coated PNA-Zr particles **A)** Representative SEM images of PNA-Zr particles with 705 SSO linker and without (left) or with (right) LP LenA coating. (Scale bars = 3 µm). Images were taken by Dr. Steffen Schmidt (LMU Munich, Germany). **B-D)** DLS and ELS of 705 SSO-Zr particles with or without LP LenA coating. Linkers are specified below each bar. **B)** Z-average in nanometers (measured in water). **C)** Polydispersity index (measured in water). **D)** Zeta potential in millivolt (measured in 10 mM NaCl).

Splice-switching activity of particles were investigated by using luciferase activity assay with HeLa pLuc/705 cells. The cells were incubated with 705 SSO-Zr particles or free PNA with and without LP LenA for 48 h followed by a luciferase activity assay. To rule out any background luciferase activity of the cell line, luminescence levels were normalized to HBG treated control cells and determined as ‘fold increase in luminescence’ [214, 219]. As shown in Figure 21A, an array of different ratios between PNA and LP LenA (1/0.5, 1/0.75, 1/1, 1/1.25, 1/1.5, 1/2, 1/2.5, 1/3) were used. Cells incubated with 5 µM free 705 SSO PNA did not show increased luciferase activity at any PNA to LP LenA ratio, which suggests that the lipopeptide is not capable of facilitating delivery of the PNA without conjugation. In contrast, LP LenA coated 705 SSO-Zr particles clearly increased luminescence levels at the ratios between 1/0.5 to 1/3. The highest increase in luminescence (125-fold) was achieved at a PNA/LP LenA ratio of 1/1.25, which was determined as optimal coating condition. Dose-titrations with free PNA and PNA-Zr nanoparticles at the optimal PNA/LP LenA ratio of 1/1.25 were carried out in a PNA concentration range between 0.156 µM to 5 µM (Figure 21B). Consistent with the previous results, free 705 SSO/LP LenA did not induce increased luciferase activity at any concentration, whereas PNA-Zr particles increased luminescence over 20- to 120-fold at PNA concentrations between 0.625 to 5 µM.

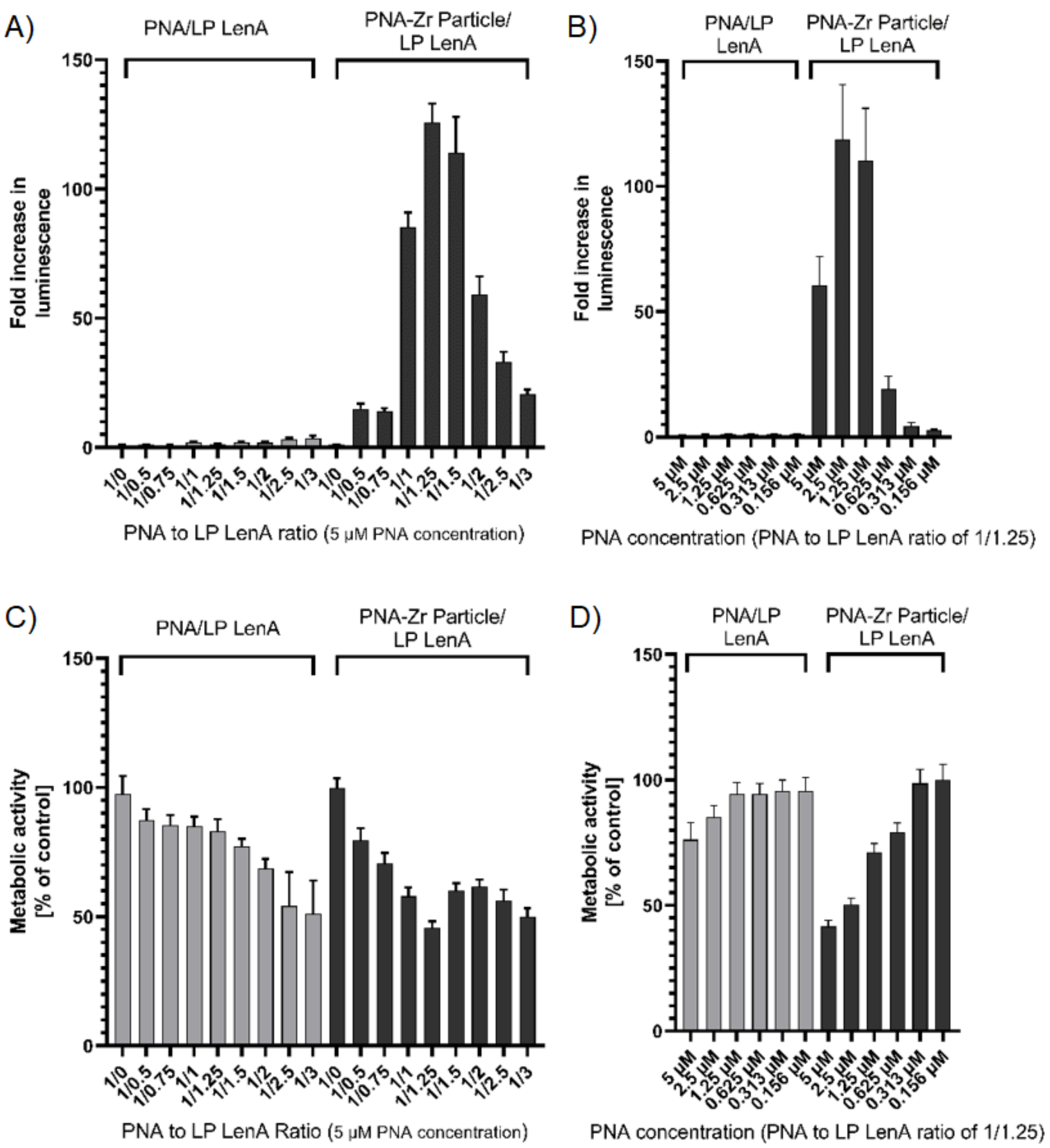

Figure 21 Splice-switching activity and metabolic activity of 705 SSO-Zr nanoparticles **A)** Splice-switching at different PNA/LP LenA coating ratios (fixed concentration of 5 µM PNA) in HeLA pLuc/705 cells. **B)** Splice-switching activity at different PNA concentrations (fixed ratio of 1/1.25 PNA/LP LenA) in HeLA pLuc/705 cells. **C)** Metabolic activity of HeLa wild type cells at different PNA/LP LenA coating ratios (fixed concentration of 5 µM PNA) **D)** Metabolic activity of HeLa wild type cells at different PNA concentrations (fixed ratio of 1/1.25 PNA/LP LenA). All luciferase and metabolic activity assays were carried out in triplicates. Free 705 SSO with or without LP LenA was used as a control.

The impact of incubation time on splice-switching activity was investigated with 705 SSO-Zr/LP LenA particles at the optimal coating ratio (1/1.25). HeLA pLuc/705 cells were incubated with varied doses of PNA-Zr nanoparticles for 12, 24, 36 and 48 hours and the increase of luciferase activity was determined subsequently (Figure 22). After an incubation time of 36 h, over 300-fold increase in luminescence was observed at a concentration of particles corresponding to 2.5 µM of PNA. Overall results indicate that 24 h incubation would be sufficient to detect significant splice switching effects. Moreover, it is suggested that the very low increase of luminescence after 12 h incubation could be the result of a need for cell division to show antisense effect as the average doubling time of HeLa cells is 33 h [236].

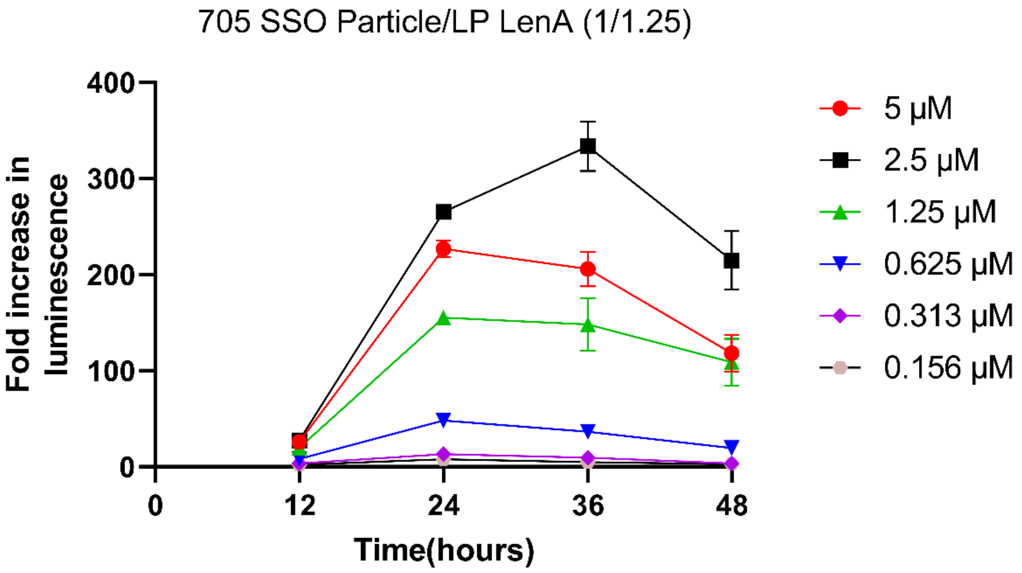

Figure 22 Splice-switching activity of LP LenA coated 705 SSO-Zr nanoparticles in HeLa pLuc/705 cells. Different PNA concentrations indicated with different colors (fixed ratio of 1/1.25 PNA/LP LenA) were used and incubation terminated at different time points. All luciferase activity assays were carried out in triplicates.

To understand whether observed splice-switching activity is caused by the sequence specific effect of the splice-switching antisense PNA, particles composed of PNA linkers with alternative sequences (PAMBA-GAGTATGAGA-TPA and PAMBA-GCAGCT-TPA) were used as controls (Figure 23). The cells were incubated with the control PNA-Zr particles LP LenA coating at 1/1.25 ratio for 48 h followed by a luciferase activity assay. Particles without SSO sequence did not increase luciferase activity indicating, that the observed effect of 705 SSO particles are sequence dependent.

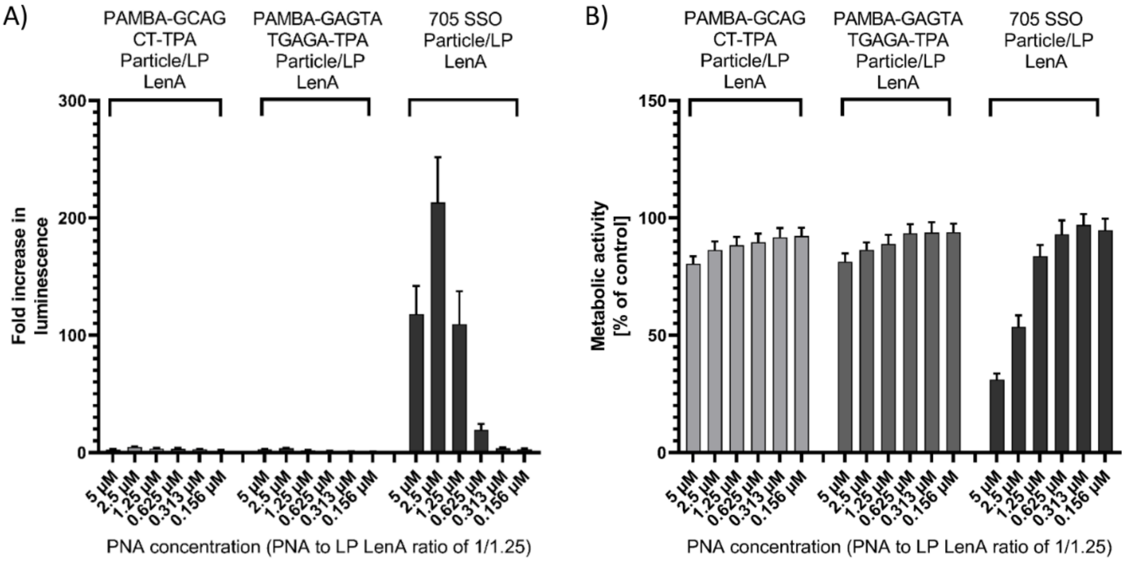

Figure 23 Splice-switching activity and metabolic activity of non-antisense-Zr nanoparticles **A)** Splice-switching activity at different PNA concentrations (fixed ratio of 1/1.25 PNA/LP LenA) in HeLA pLuc/705 cells. **B)** Metabolic activity of HeLa wild type cells at different PNA concentrations (fixed ratio of 1/1.25 PNA/LP LenA). All luciferase and metabolic activity assays were carried out in triplicates. 705 SSO was used as positive control.

To additionally confirm the advantage of PNA-Zr nanoparticle formation for cellular delivery, another control experiment was performed (Figure 24). Phosphate buffer was used to compete with PNA linkers and destabilize Zr-linker interactions. 705 SSO-Zr nanoparticles with LP LenA at optimal ratio of 1/1.25 were disassembled by incubation with PBS. Treatment of HeLa pLuc/705 cells with the obtained solution showed negligible effects on luminescence levels. The results demonstrate, that the initially very efficient PNA-Zr nanoparticles lost their delivery potential upon particle destruction.

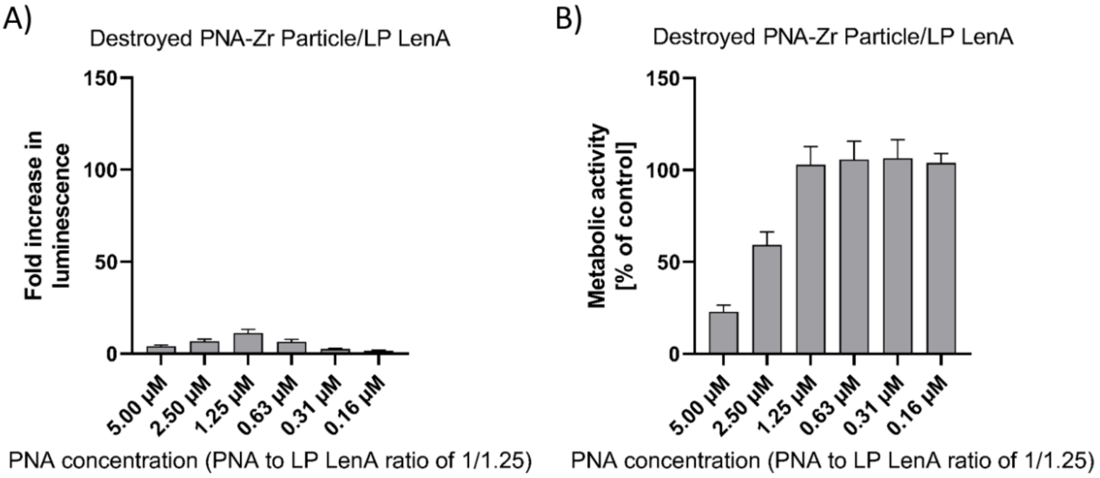

Figure 24 Splice-switching and Metabolic activity of destroyed PNA-Zr particles. **A)** Splice-switching activity of destroyed PNA-Zr particles containing SSO 705 in HeLA pLuc/705 cells. Cells were treated for 48 h with solutions of disassembled particles containing 0.16 to 5 µM SSO 705 and a 1/1.25 PNA to LP LenA ratio before luciferase activity assay. **B)** Metabolic activity was determined by CellTiter-Glo® assay in HeLa wild type cells after 48 h treatment with destroyed particles containing 0.16 to 5 µM PNA and a 1/1.25 PNA to LP LenA ratio. Metabolic activity was determined as percentage of luminescence levels in treated cells normalized to HBG treated control cells.

As mentioned above, particles can be disassembled in phosphate buffer. This observation raised the question, how stable the particles are at phosphate concentration similar to serum (at adults, 1.12 mM to 1.45 mM) [237]. For answering this, particle stability was investigated at different PBS dilutions leading to different phosphate concentrations as well as in 20% filtered (0.2 µm) FBS (Figure 25). Concentration depended stability decrease was observed for the particles in PBS. Similarly, particles also disassociated in FBS over the course of one hour, however coating with LP LenA, clearly increased the serum stability of particles. This suggests, that one advantage of the particle coating is the increase of particle stability.

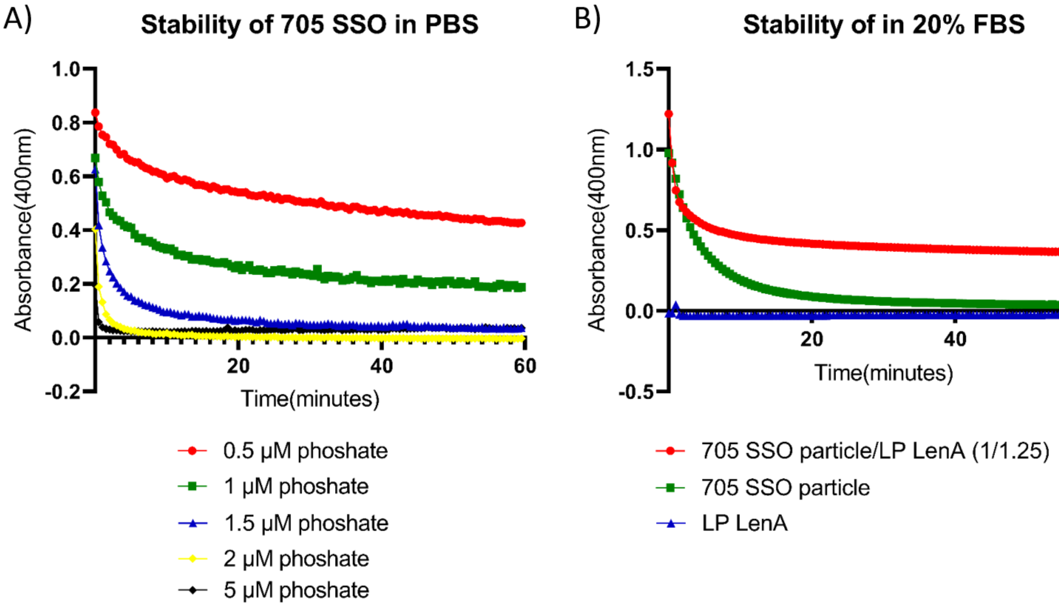

Figure 25 Stability of 705 SSO-Zr particles determined by measurement of optical density (400nm) in PBS and FBS. **A)** Stability of 705 SSO-Zr particles at PBS dilutions leading to different phosphate concentrations indicated by colors. **B)** Stability of 705 SSO-Zr particles (red), LP LenA coated 705 SSO-Zr particles (green) and free LP LenA in 20% filtered FBS.

The intended splice-switch of mutated β-globin intron in the HeLa pLuc/705 model was additionally confirmed by RT-PCR (Figure 26). Total RNA was extracted from HeLa pLuc/705 cells 48 h after the treatment with 705 SSO-Zr/LP LenA at optimal 1/1.25 ratio. Afterwards, the sequence surrounding β-globin IVS2 was amplified by RT-PCR and analyzed via agarose electrophoresis. The single band (268 bp) obtained from HBG treated control cells represents the unchanged aberrant splicing product. In case of 705 SSO-Zr nanoparticle treated cells, a dose-dependent appearance of an additional band (142 bp) could be detected, which corresponds to the product after splicing correction.

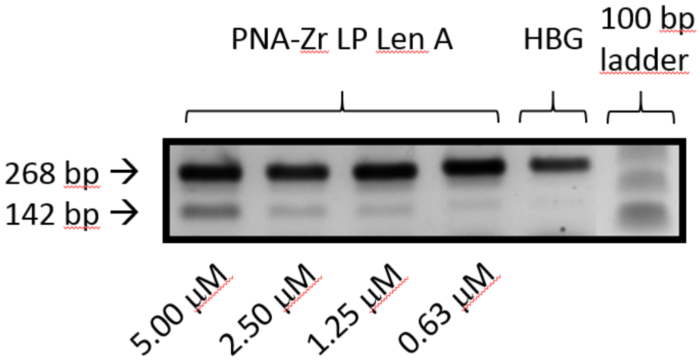

Figure 26 RT-PCR of β-globin IVS2 from HeLa pLuc/705 cells treated with PNA-Zr/LP LenA at ratio 1/1.25. Total RNA was isolated 48 h after treatments and β-globin IVS2 was amplified. Bands at 268 bp represent the aberrant splicing product; bands at 142 bp correspond to the product after splice-switch.

Potential cytotoxicity of the PNA-Zr particles was investigated by CellTiter-Glo® assay with HeLa wild type cells (Figure 21C, D and Figure 22). Analog to the splice-switching experiments, cells were incubated for 48 h with free PNA or PNA-Zr particles at different concentrations and LP LenA ratios. Without LP LenA, neither free PNA, nor PNA-Zr particles mediated effects on metabolic activity at 5 µM, which indicates good tolerability at the relatively high concentration. In combination with LP LenA a dose- and ratio-dependent reduction of metabolic activity became obvious. It is speculated that LP LenA, similar to other potent delivery agents and cationic lipids, is able to impair cellular processes due to pronounced interactions [238, 239]. However, since the 705 SSO-Zr particles were not able to induce substantial splice-switching alone, the combination with the potent LP LenA coating is considered a reasonable measure to boost endosomal release and enhance intracellular PNA delivery. It is suggested, that fine-tuning particle parameters, coating ratios and dosing can lead to a favorable balance between delivery efficiency and tolerability.

As mentioned, calcein loaded PNA-Zr particles were able to be visualized by microscopy indicating cellular uptake of PNA-Zr particles. On their own, PNA-Zr particles may not have enough uptake or have limited endosomal escape ability. When combined with LP LenA these supposed weakness can be solved with cost of effects on cell viability. To be specific, LP LenA changes charge of the construct from negative to positive (Figure 20D) which enables better cell membrane interaction probably by endocytosis like the most of the positively charged carriers. After cellular uptake, nucleic acid containing polyplexes can interact with phospholipids of the endosomal membrane, which destabilize the membrane and release the cargo into the cytosol [240]. Similarly, LP LenA-PMO conjugates were found to facilitate endosomal escape after cellular uptake [219]. Therefore, it is assumed that the addition of LP LenA to PNA-Zr can facilitate endosomal escape of the particles to the cytosol. To confirm this, HeLa mRuby3/gal8 reporter cells were used, which indicate effects on endosomal membrane integrity. HeLa mRuby3/gal8 express a fusion protein of galectin-8 and mRuby3. Galectin-8 is a cytosolic protein that accumulates at damaged endosomes due to binding to glycosylation moieties located on the inner face of endosomal membranes [241]. CLSM imaging of naked 705 SSO-Zr nanoparticles and LP LenA coated 705 SSO-Zr particles were performed. HeLa Gal8 mRuby3 cells were incubated for 8 h with the particles followed by a medium change and additional 4 h incubation. CLSM imaging showed that particles alone did not lead to a redistribution of galectin8, indicating minimal endosomal disruption (Figure 27). On the other hand, LP LenA coated particles clearly disturbed the endosomes, which is visible due to localized mRuby3/gal8 signals. Overall, the results support the hypothesis that LP LenA plays a crucial role for endosomal escape.

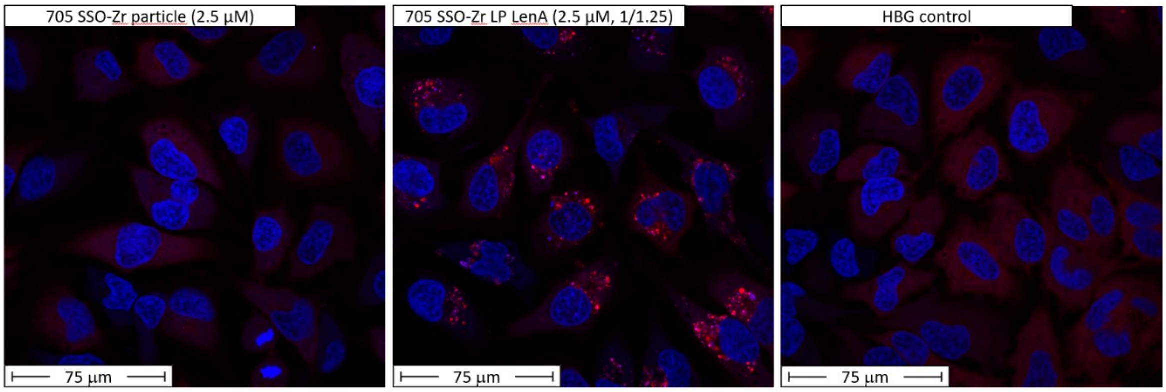

Figure 27 CLSM images of HeLa mRuby3/gal8 cells treated with 705 SSO-Zr particles (left), LP LenA coated 705 SSO-Zr particles (1/1.25 ratio, middle) and HBG control (right). mRuby3/gal8 cells were incubated for 8 hours with particles (2.5 µM PNA content). Subsequently, the cells were incubated for additional 4 hours with fresh medium before imaging. Staining and imaging was done by Miriam Höhn (LMU Pharmaceutical Biotechnology).

4. Summary

Nucleic acid therapeutics such as antisense or splice switching oligonucleotides are an innovative class of biopharmaceuticals. Despite the potential to treat several live threatening, severe diseases, only handful of products are on the market. Main problem faced by nucleic acid therapeutics is safe and efficient intracellular delivery. This much needed delivery is only possible with potent and flexible carrier systems. In this work, a novel delivery strategy based on nanoscale coordination polymers formed by synthetic nucleic acid analog has been developed.

After several trials, a robust coordination nanoparticle formation method has been established. The synthesis requires a two-step procedure by a first preformation of $Zr_6O_4(OH)_4$ nodes and second assembly with PNA linkers at RT. A systematic variation of PNA linker design identified crucial need for two aromatic carboxylic acid functions (PAMBA, TPA) for the coordinative interaction with Zr(IV) nodes. By positioning said carboxylic acid functions into different PNA strands of the double stranded linker, less stable and thermal degradation sensitive particles are generated. Because of melting temperatures of the PNA sequences, particles formed by double-stranded PNA linkers with separated aromatic carboxylic acids on different strands require at least 6-mer sequences. On the other hand, nanoparticles built from PNA linkers with both aromatic carboxylic acids on a single strand exhibit higher stability and thermal resistance. Characterization of the PNA-Zr particles revealed amorphous, spherical nanoparticles featuring an extraordinary PNA loading capacity of > 94 % w/w. Further, PNA-Zr particles showed loading capacity for the fluorescent dye calcein and were readily taken up by cells. The overall negative charge of the PNA-Zr particles, regardless of linker sequence, makes electrostatic interaction with cationic carriers possible. To facilitate endosomal release, coating with a cationic lipopeptide was utilized and resulting particles were able to deliver functional antisense PNAs which show splice-switching activity.

Overall, a highly flexible platform has been established, which combines customizable PNA linker chemistry with coordinative driven self-assembly to generate nanoparticles with imprinted biological activity. The presented bio-active, sequence customizable PNA-Zr nanoparticle platform provides great potential for oligonucleotide based applications, such as antisense or splicing-modifying therapies.

5. Appendix

5.1 Abbreviations

ATP	Adenosine 5′-triphosphate
ACI	Acetic acid
ASO	Antisense oligonucleotide
BET	Brunauer–Emmett–Teller equation
BPEI	Branched PEI
CLSM	Confocal laser scanning microscopy
DAPI	4′,6-diamidino-2- phenylindole
DCM	Dichloromethane
DIPEA	*N,N*-Diisopropylethylamine
DLS	Dynamic light scattering
DMEM	Dulbecco’s modified Eagle’s medium
DMF	*N,N*-dimethylformamide
DNA	Desoxyribonucleic acid
ds	Double-stranded
DOPC	1,2-dioleoyl-sn-glycero-3-phosphocholine
DOTMA	1,2-di-O-octadecenyl-3-trimethylammonium propane
DTT	Dithiothreitol
EDTA	Ethylendiaminetetraacetic acid
ELS	Electrophoretic light scattering
EMA	European Medicines Agency
FBS	Fetal bovine serum
FDA	Food and Drug Administration
FR	Folate receptor
HA	Hyaluronic acid
HBG	Hepes-buffered glucose
HEPES	N-(2-Hydroxethyl) piperazine-N‘-(2-ethansulfonic acid)
HIV	Human immunodeficiency virus
HOBt	1-Hydroxybenzotriazole
ICP-AES	Inductively coupled plasma atomic emission spectroscopy
LP LenA	(Y3-Stp2-K-ε[G-K-α,ε(linolenic acid)2]αStp2-Y3-K-ε(N3))
LP	Lipopeptide
LPEI	Linear polyethylenimine
mM	Millimolar
MOF	Metal organic frameworks
mRNA	Messenger RNA
MTBE	methyl-tert-butyl ether
mV	Millivolt

nm	Nanometer
NMP	N-methyl-2-pyrrolidone
ns	Not significant
PAMBA	para-aminomethylbenzoic acid
PBS	Phosphate-buffered saline
PCR	Polymerase Chain Reaction
PDI	Polydispersity index
pDNA	Plasmid DNA
PEG	Polyethylene glycol
PEI	Polyethylenimine
PFA	Paraformaldehyde
PMO	Phosphorodiamidate morpholino oligomers
PTFE	Pre-fitted polytetrafluoroethylene
PNA	Peptide nucleic acid
PyBOP	benzotriazol-1-yloxy-tripyrrolidinophosphonium hexafluorophosphate
RGD	Arginine–glycine–aspartic acid
RLU	Relative light units
RNA	Ribonucleic acid
RT	Room temperature
RT-PCR	Reverse-transcription PCR
SEM	Scanning electron microscopy
siRNA	Small interfering RNA
ss	Single strand
SPS	Solid-phase synthesis
SSO	Splice-switching oligonucleotides
TBE	Tris-boric acid-EDTA buffer
TFA	Trifluoroacetic acid
TfR	Transferrin receptor
TIS	Triisopropylsilane
TPA	Terephthalic acid
XRD	X-ray diffraction

5.2 Mass Spectrometry Data

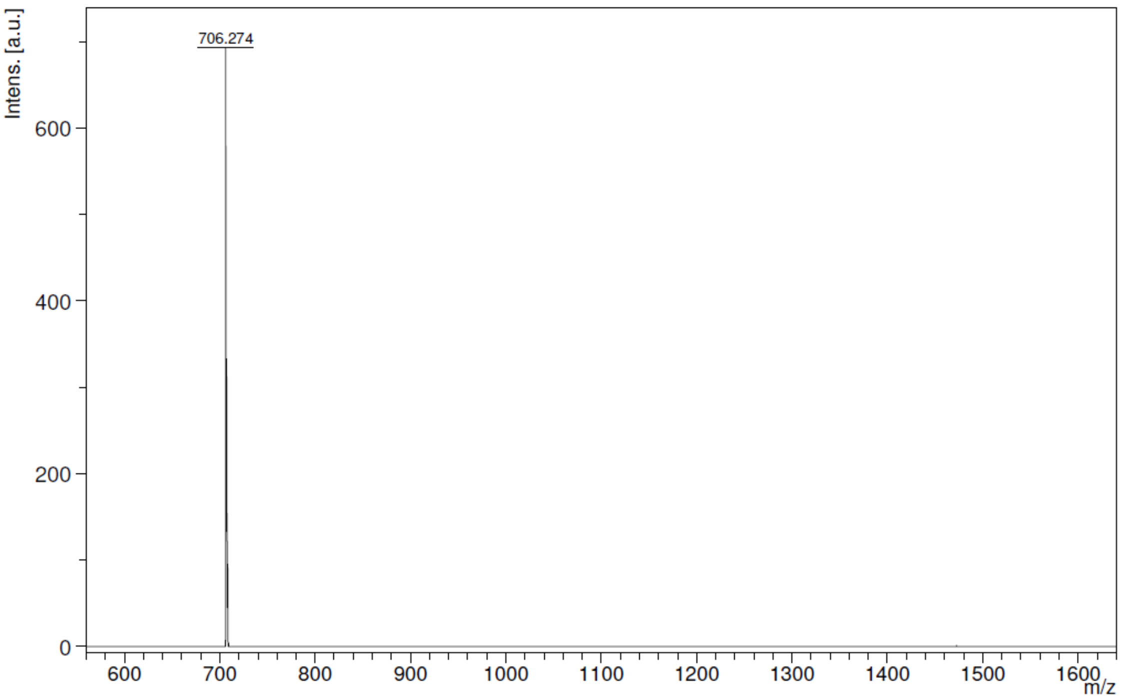

MALDI-TOF-MS spectrum of GC-TPA (calculated 707.5, observed 706.3).

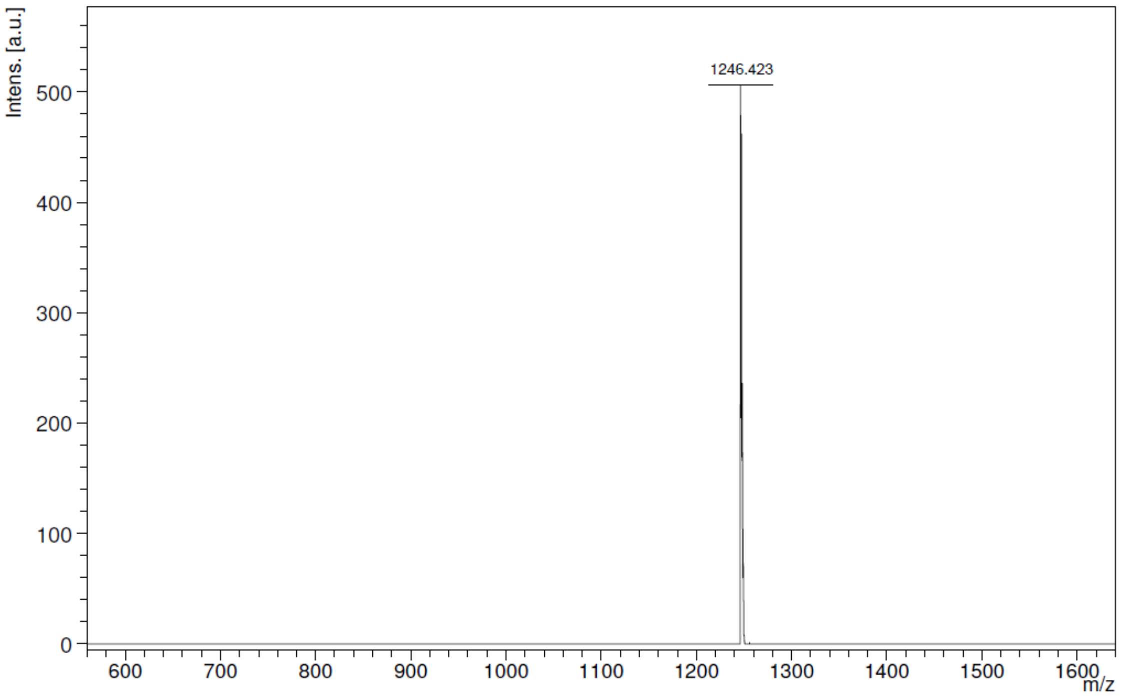

MALDI-TOF-MS spectrum of CATG-TPA (calculated 1249.1, observed 1246.4).

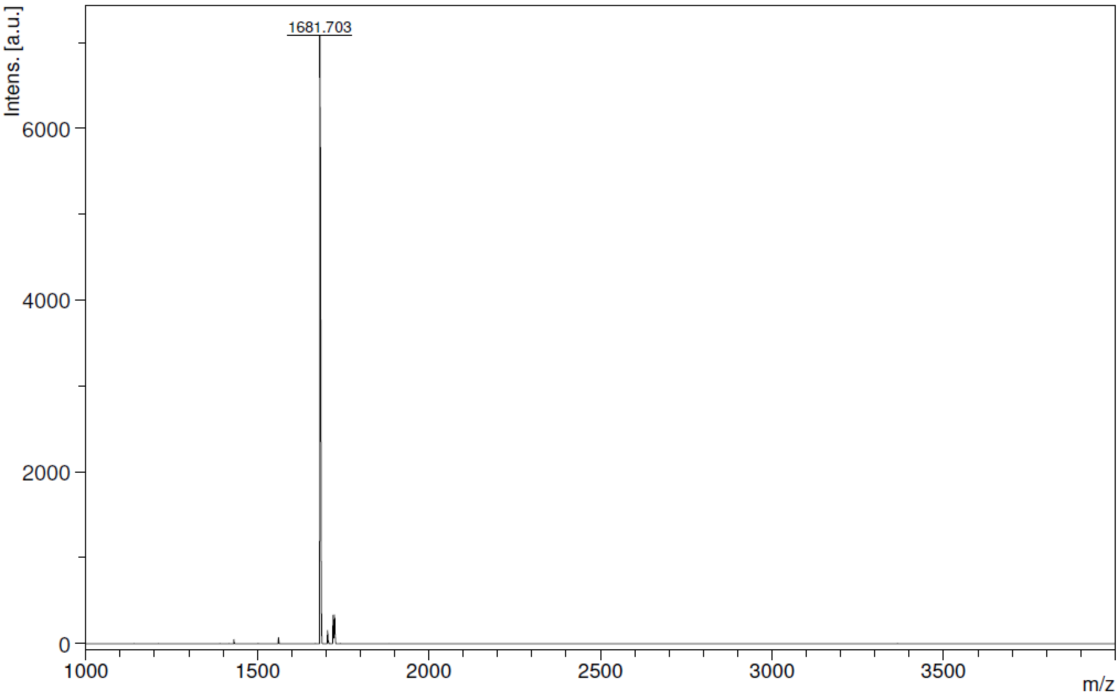

MALDI-TOF-MS spectrum of GCATGC-ACI (calculated 1685.6, observed 1681.7).

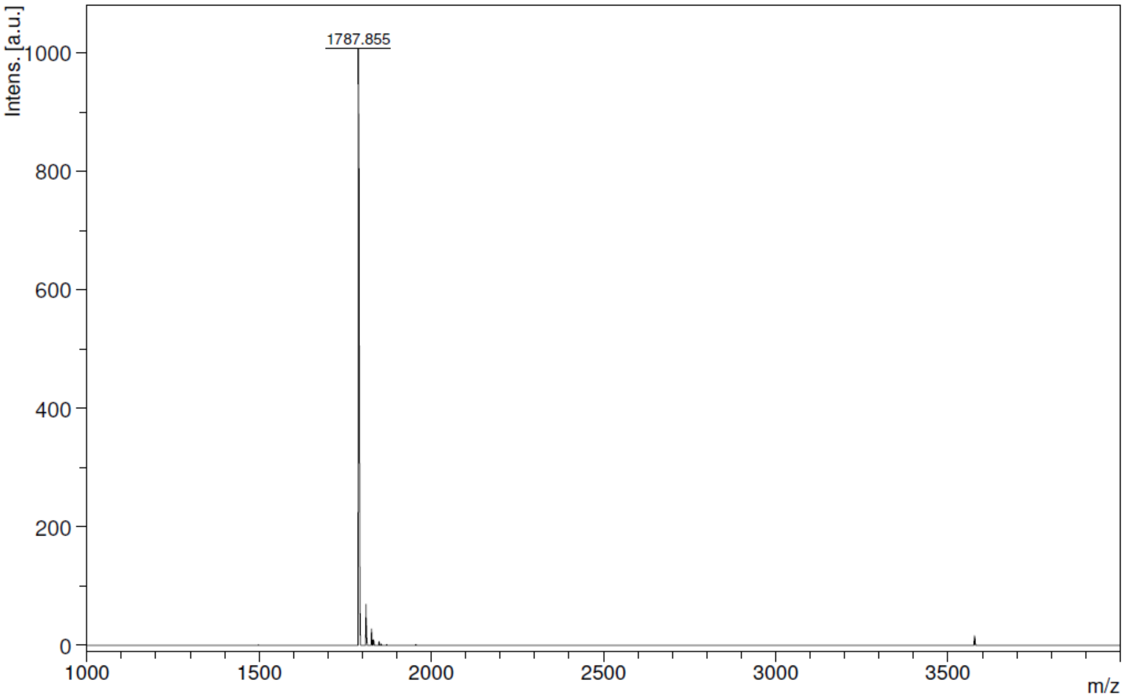

MALDI-TOF-MS spectrum of GCATGC-TPA (calculated 1791.6, observed 1787.9).

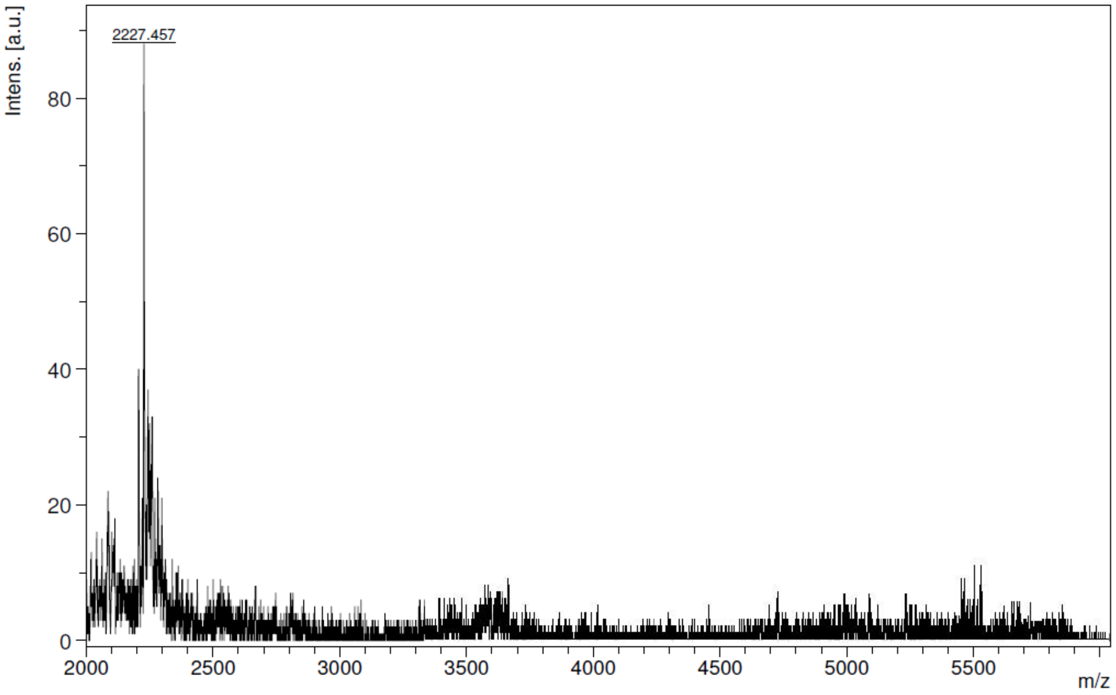

MALDI-TOF-MS spectrum of CAGTACTG-ACI (calculated 2227.1, observed 2227.5).

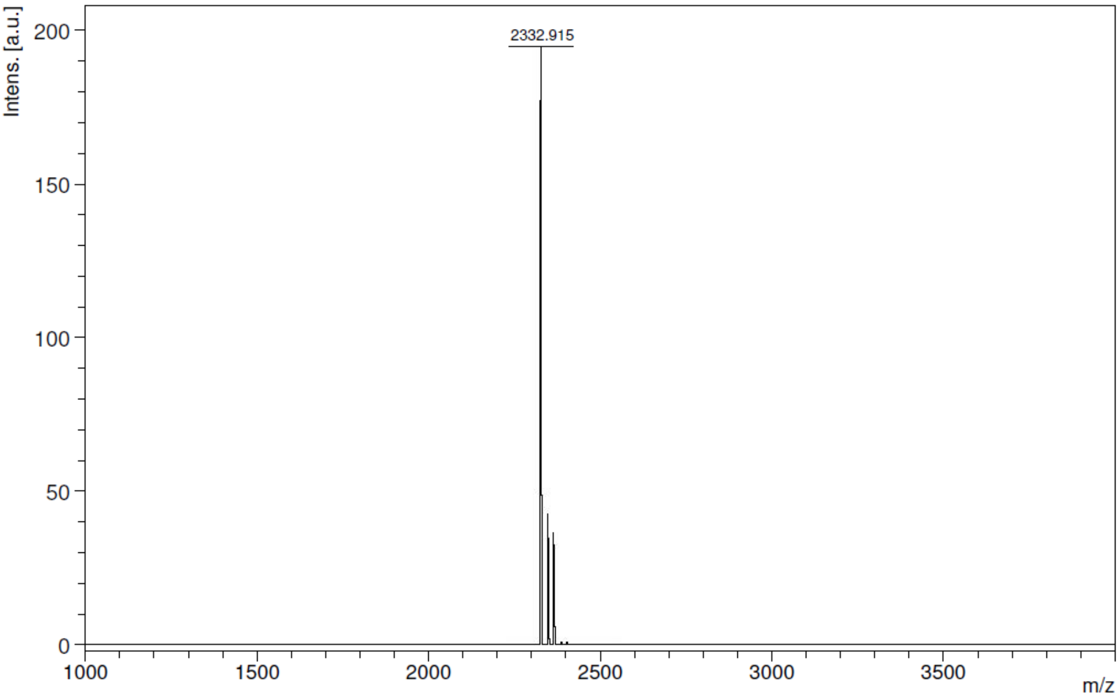

MALDI-TOF-MS spectrum of CAGTACTG-TPA (calculated 2333.1, observed 2332.9).

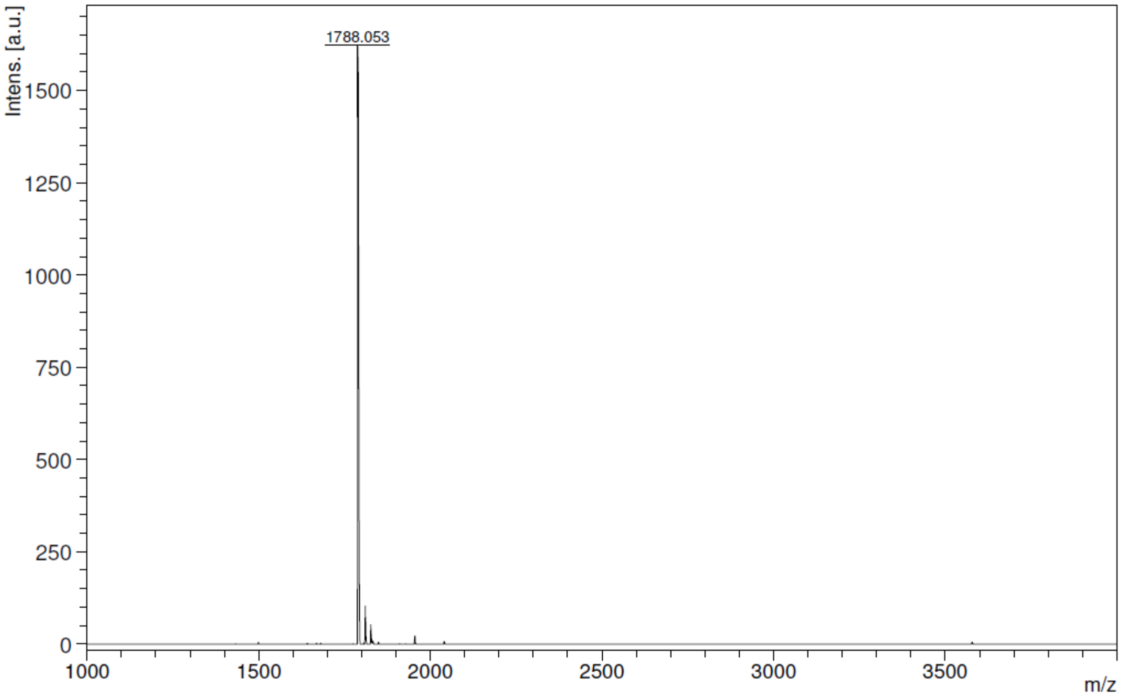

MALDI-TOF-MS spectrum of CGTGAC-TPA (calculated 1791.6, observed 1788.1).

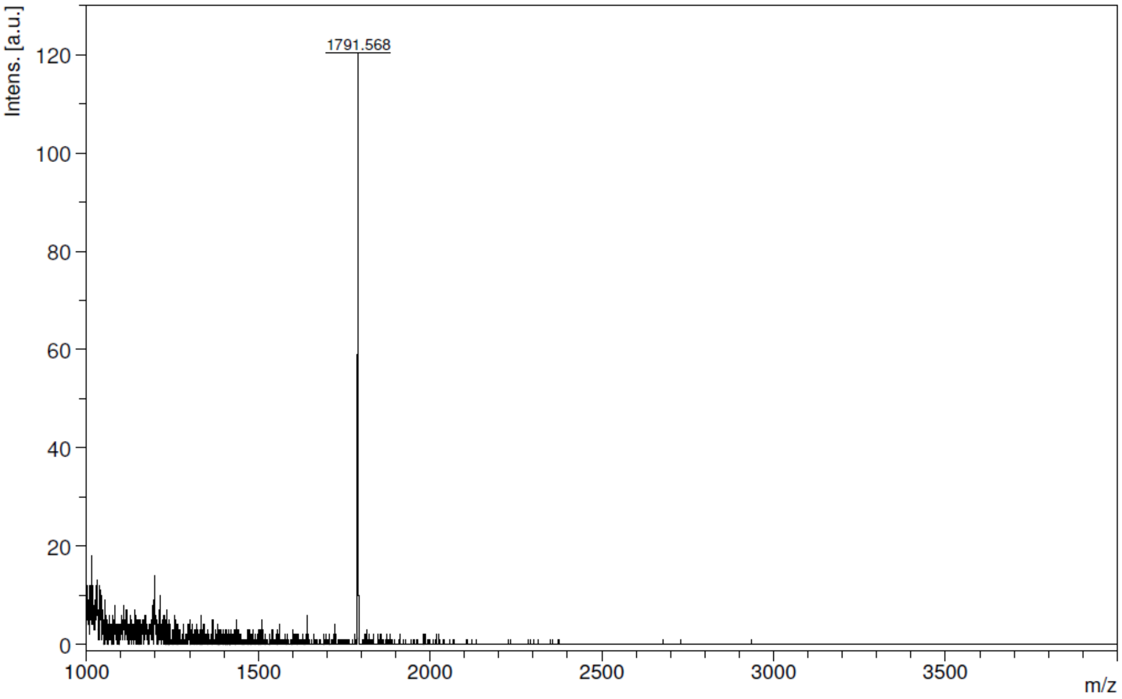

MALDI-TOF-MS spectrum of GTCACG-TPA (calculated 1791.6, observed 1791.6).

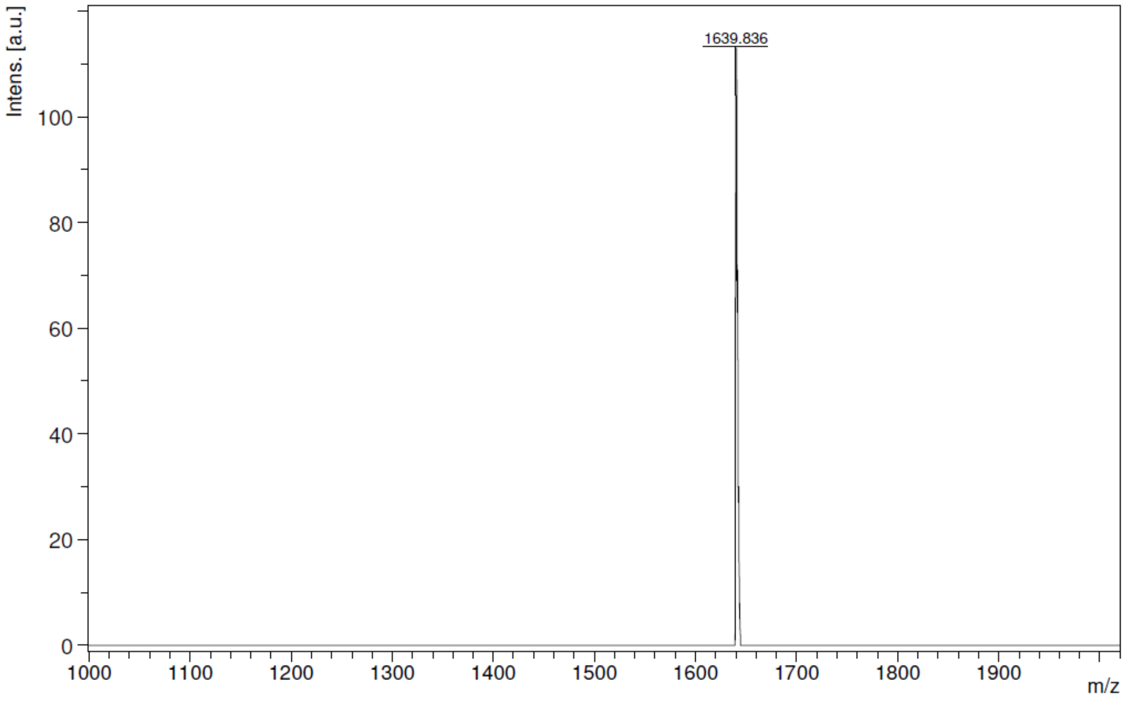

MALDI-TOF-MS spectrum of GTCACG (calculated 1643.6, observed 1639.8).

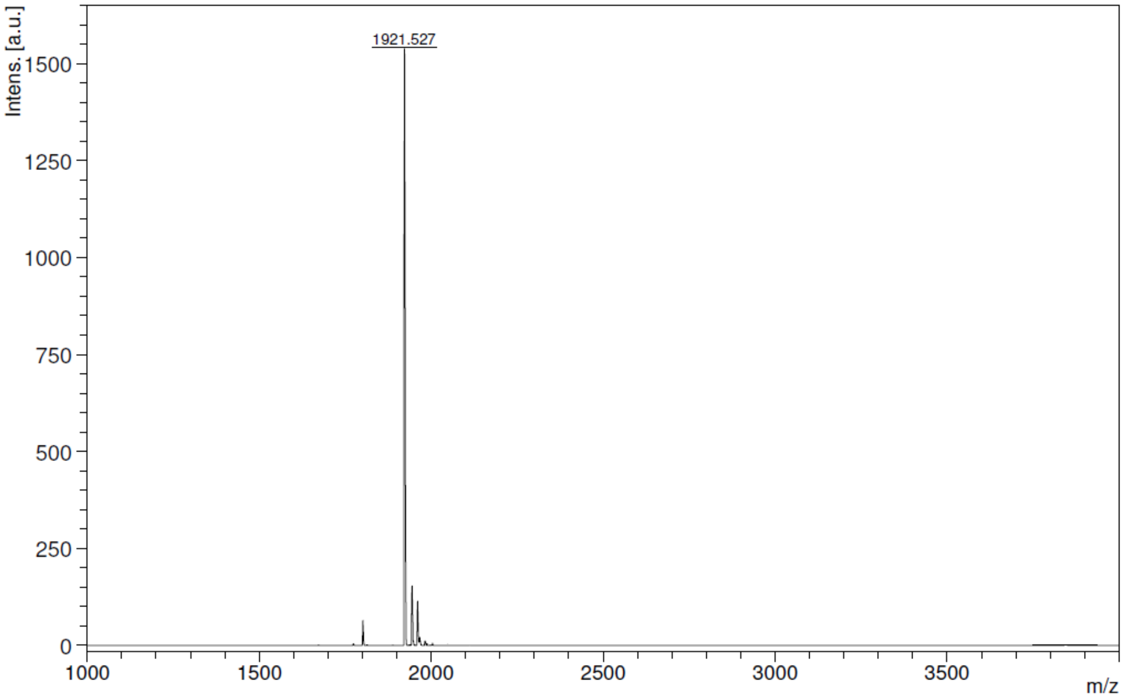

MALDI-TOF-MS spectrum of PAMBA-CGTGAC-TPA (calculated 1924.6, observed 1921.5).

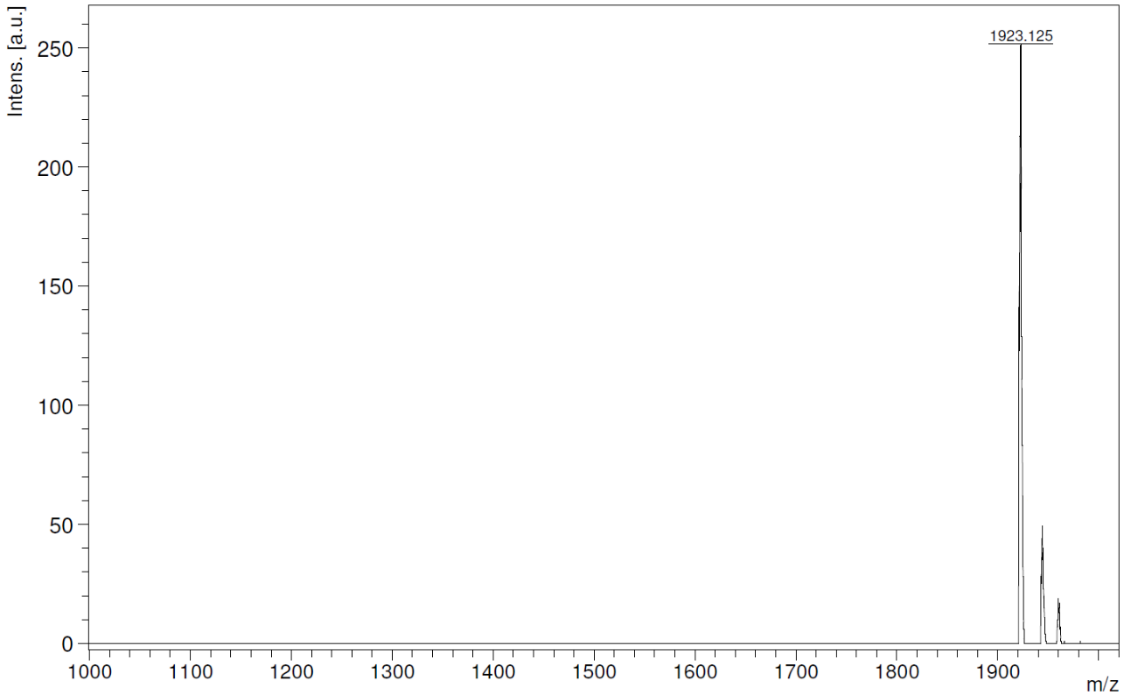

MALDI-TOF-MS spectrum of PAMBA-GCAGCT-TPA (calculated 1924.6, observed 1923.1).

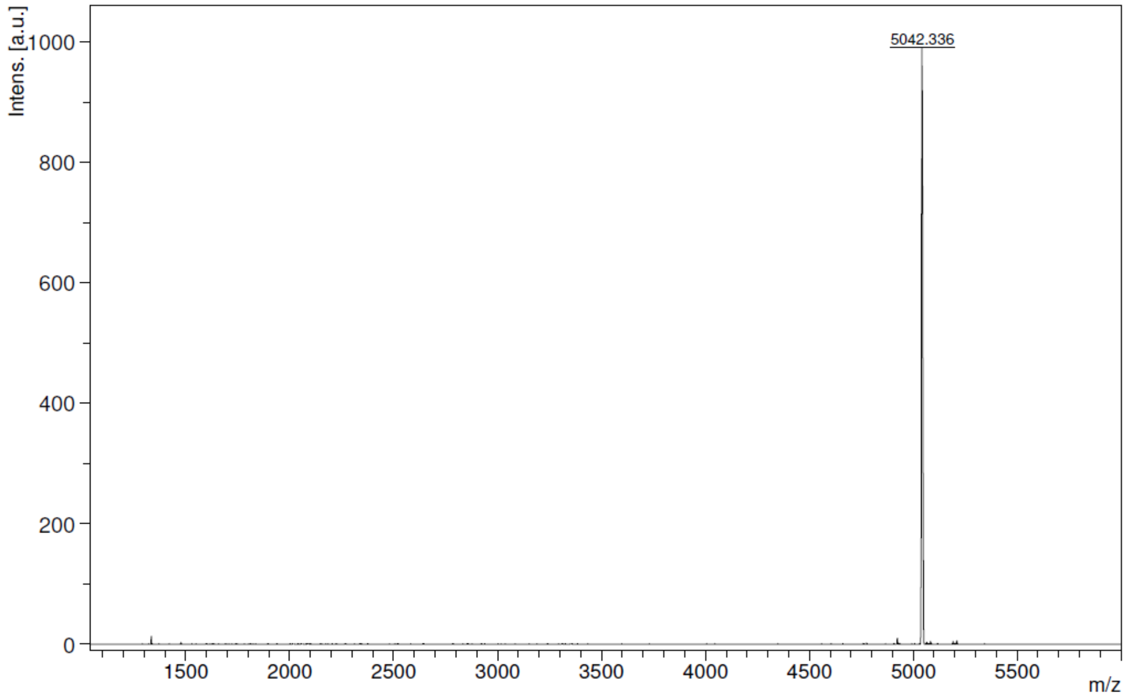

MALDI-TOF-MS spectrum of PAMBA-CCTCTTACCTCAGTTACA-TPA (calculated 5046.6, observed 5042.3).

6. References

1. Yaghi, O.M., et al., *Reticular synthesis and the design of new materials.* Nature, 2003. **423**(6941): p. 705-714.
2. Férey, G., *Hybrid porous solids: past, present, future.* Chemical Society Reviews, 2008. **37**(1): p. 191-214.
3. Kalmutzki, M.J., N. Hanikel, and O.M. Yaghi, *Secondary building units as the turning point in the development of the reticular chemistry of MOFs.* Science Advances, 2018. **4**(10): p. eaat9180.
4. Fonseca, J., et al., *Metal–organic frameworks (MOFs) beyond crystallinity: amorphous MOFs, MOF liquids and MOF glasses.* Journal of Materials Chemistry A, 2021. **9**(17): p. 10562-10611.
5. Wang, S., et al., *A robust zirconium amino acid metal-organic framework for proton conduction.* Nature Communications, 2018. **9**(1): p. 4937.
6. Wißmann, G., et al., *Modulated synthesis of Zr-fumarate MOF.* Microporous and Mesoporous Materials, 2012. **152**: p. 64-70.
7. Chui, S.S., et al., *A chemically functionalizable nanoporous material.* Science, 1999. **283**(5405): p. 1148-50.
8. Gustafsson, M. and X. Zou, *Crystal formation and size control of zeolitic imidazolate frameworks with mixed imidazolate linkers.* Journal of Porous Materials, 2013. **20**(1): p. 55-63.
9. Zhang, G., et al., *A Robust Sulfonate-Based Metal–Organic Framework with Permanent Porosity for Efficient CO2 Capture and Conversion.* Chemistry of Materials, 2016. **28**(17): p. 6276-6281.
10. Ren, J., et al., *Modulated synthesis of chromium-based metal-organic framework (MIL-101) with enhanced hydrogen uptake.* International Journal of Hydrogen Energy, 2014. **39**(23): p. 12018-12023.
11. Lu, K., C. He, and W. Lin, *Nanoscale Metal–Organic Framework for Highly Effective Photodynamic Therapy of Resistant Head and Neck Cancer.* Journal of the American Chemical Society, 2014. **136**(48): p. 16712-16715.
12. Singha, D.K., et al., *A luminescent cadmium based MOF as selective and sensitive iodide sensor in aqueous medium.* Journal of Photochemistry and Photobiology A: Chemistry, 2018. **356**: p. 389-396.
13. Tan, Q.-H., et al., *A gadolinium MOF acting as a multi-responsive and highly selective luminescent sensor for detecting o-, m-, and p-nitrophenol and Fe3+ ions in the aqueous phase.* RSC Advances, 2016. **6**(66): p. 61725-61731.
14. Horcajada, P., et al., *Synthesis and catalytic properties of MIL-100(Fe), an iron(iii) carboxylate with large pores.* Chemical Communications, 2007(27): p. 2820-2822.
15. Katz, M.J., et al., *A facile synthesis of UiO-66, UiO-67 and their derivatives.* Chemical Communications, 2013. **49**(82): p. 9449-9451.
16. Furukawa, H., et al., *The chemistry and applications of metal-organic frameworks.* Science, 2013. **341**(6149): p. 1230444.

17. Ma, M., et al., *A Method for the Preparation of Highly Porous, Nanosized Crystals of Isoreticular Metal−Organic Frameworks.* Crystal Growth & Design, 2011. **11**(1): p. 185-189.
18. Ni, Z. and R.I. Masel, *Rapid Production of Metal−Organic Frameworks via Microwave-Assisted Solvothermal Synthesis.* Journal of the American Chemical Society, 2006. **128**(38): p. 12394-12395.
19. Chalati, T., et al., *Optimisation of the synthesis of MOF nanoparticles made of flexible porous iron fumarate MIL-88A.* Journal of Materials Chemistry, 2011. **21**(7): p. 2220-2227.
20. Moghadam, P.Z., et al., *Development of a Cambridge Structural Database Subset: A Collection of Metal–Organic Frameworks for Past, Present, and Future.* Chemistry of Materials, 2017. **29**(7): p. 2618-2625.
21. Lu, W., et al., *Tuning the structure and function of metal-organic frameworks via linker design.* Chem Soc Rev, 2014. **43**(16): p. 5561-93.
22. Czaja, A.U., N. Trukhan, and U. Muller, *Industrial applications of metal-organic frameworks.* Chem Soc Rev, 2009. **38**(5): p. 1284-93.
23. Tong, P.-H., et al., *Metal–organic frameworks (MOFs) as host materials for the enhanced delivery of biomacromolecular therapeutics.* Chemical Communications, 2021. **57**(91): p. 12098-12110.
24. Rogge, S.M.J., et al., *Metal-organic and covalent organic frameworks as single-site catalysts.* Chem Soc Rev, 2017. **46**(11): p. 3134-3184.
25. He, Y., et al., *Methane storage in metal–organic frameworks.* Chemical Society Reviews, 2014. **43**(16): p. 5657-5678.
26. Adil, K., et al., *Gas/vapour separation using ultra-microporous metal–organic frameworks: insights into the structure/separation relationship.* Chemical Society Reviews, 2017. **46**(11): p. 3402-3430.
27. Abánades Lázaro, I., et al., *Selective Surface PEGylation of UiO-66 Nanoparticles for Enhanced Stability, Cell Uptake, and pH-Responsive Drug Delivery.* Chem, 2017. **2**(4): p. 561-578.
28. Della Rocca, J. and W. Lin, *Nanoscale Metal–Organic Frameworks: Magnetic Resonance Imaging Contrast Agents and Beyond.* European Journal of Inorganic Chemistry, 2010. **2010**(24): p. 3725-3734.
29. Baumann, A.E., et al., *Metal-organic framework functionalization and design strategies for advanced electrochemical energy storage devices.* Communications Chemistry, 2019. **2**(1): p. 86.
30. Dahri, M., et al., *Nanoscale aggregation of doxorubicin-short peptide conjugates for enzyme-responsive delivery with various MOF carriers: In-silico steps towards smart cancer chemotherapy.* Computers in Biology and Medicine, 2022. **144**: p. 105386.
31. Morris, W., et al., *Nucleic Acid–Metal Organic Framework (MOF) Nanoparticle Conjugates.* Journal of the American Chemical Society, 2014. **136**(20): p. 7261-7264.
32. Pinna, A., et al., *A MOF-based carrier for in situ dopamine delivery.* RSC Advances, 2018. **8**(45): p. 25664-25672.
33. Wuttke, S., et al., *Positioning metal-organic framework nanoparticles within the context of drug delivery - A comparison with mesoporous silica nanoparticles and dendrimers.* Biomaterials, 2017. **123**: p. 172-183.
34. Horcajada, P., et al., *Porous metal-organic-framework nanoscale carriers as a potential platform for drug delivery and imaging.* Nat Mater, 2010. **9**(2): p. 172-8.

35. Röder, R., et al., *Multifunctional Nanoparticles by Coordinative Self-Assembly of His-Tagged Units with Metal–Organic Frameworks.* Journal of the American Chemical Society, 2017. **139**(6): p. 2359-2368.
36. Alsaiari, S.K., et al., *Endosomal Escape and Delivery of CRISPR/Cas9 Genome Editing Machinery Enabled by Nanoscale Zeolitic Imidazolate Framework.* Journal of the American Chemical Society, 2018. **140**(1): p. 143-146.
37. Lismont, M., L. Dreesen, and S. Wuttke, *Metal-Organic Framework Nanoparticles in Photodynamic Therapy: Current Status and Perspectives.* Advanced Functional Materials, 2017. **27**(14): p. 1606314.
38. Ni, K., et al., *Nanoscale metal-organic frameworks enhance radiotherapy to potentiate checkpoint blockade immunotherapy.* Nature Communications, 2018. **9**(1): p. 2351.
39. Yang, J., et al., *Zr-Based MOFs Shielded with Phospholipid Bilayers: Improved Biostability and Cell Uptake for Biological Applications.* Chemistry of Materials, 2017. **29**(10): p. 4580-4589.
40. He, C., K. Lu, and W. Lin, *Nanoscale metal-organic frameworks for real-time intracellular pH sensing in live cells.* J Am Chem Soc, 2014. **136**(35): p. 12253-6.
41. Zhang, J.W., et al., *Water-stable metal-organic frameworks with intrinsic peroxidase-like catalytic activity as a colorimetric biosensing platform.* Chem Commun (Camb), 2014. **50**(9): p. 1092-4.
42. Lu, K., et al., *Nanoscale Metal–Organic Frameworks for Therapeutic, Imaging, and Sensing Applications.* Advanced Materials, 2018. **30**(37): p. 1707634.
43. Taylor-Pashow, K.M.L., et al., *Postsynthetic Modifications of Iron-Carboxylate Nanoscale Metal−Organic Frameworks for Imaging and Drug Delivery.* Journal of the American Chemical Society, 2009. **131**(40): p. 14261-14263.
44. Rieter, W.J., K.M.L. Taylor, and W. Lin, *Surface Modification and Functionalization of Nanoscale Metal-Organic Frameworks for Controlled Release and Luminescence Sensing.* Journal of the American Chemical Society, 2007. **129**(32): p. 9852-9853.
45. Moghimi, S.M., A.C. Hunter, and J.C. Murray, *Long-Circulating and Target-Specific Nanoparticles: Theory to Practice.* Pharmacological Reviews, 2001. **53**(2): p. 283-318.
46. Albanese, A., P.S. Tang, and W.C. Chan, *The effect of nanoparticle size, shape, and surface chemistry on biological systems.* Annu Rev Biomed Eng, 2012. **14**: p. 1-16.
47. Ettlinger, R., et al., *Toxicity of metal–organic framework nanoparticles: from essential analyses to potential applications.* Chemical Society Reviews, 2022. **51**(2): p. 464-484.
48. Sajid, M., *Toxicity of nanoscale metal organic frameworks: a perspective.* Environ Sci Pollut Res Int, 2016. **23**(15): p. 14805-7.
49. Redfern, J., et al., *Toxicity and Antimicrobial Properties of ZnO@ZIF-8 Embedded Silicone against Planktonic and Biofilm Catheter-Associated Pathogens.* ACS Applied Nano Materials, 2018. **1**(4): p. 1657-1665.
50. Ruyra, A., et al., *Synthesis, culture medium stability, and in vitro and in vivo zebrafish embryo toxicity of metal-organic framework nanoparticles.* Chemistry, 2015. **21**(6): p. 2508-18.

51. Tamames-Tabar, C., et al., *Cytotoxicity of nanoscaled metal–organic frameworks.* Journal of Materials Chemistry B, 2014. **2**(3): p. 262-271.
52. Wang, H.-S., Y.-H. Wang, and Y. Ding, *Development of biological metal–organic frameworks designed for biomedical applications: from bio-sensing/bio-imaging to disease treatment.* Nanoscale Advances, 2020. **2**(9): p. 3788-3797.
53. Freund, R., et al., *Multifunctional Efficiency: Extending the Concept of Atom Economy to Functional Nanomaterials.* ACS Nano, 2018. **12**(3): p. 2094-2105.
54. Steinborn, B. and U. Lächelt, *Metal-organic Nanopharmaceuticals.* Pharmaceutical Nanotechnology, 2020. **8**(3): p. 163-190.
55. Rieter, W.J., et al., *Nanoscale Coordination Polymers for Platinum-Based Anticancer Drug Delivery.* Journal of the American Chemical Society, 2008. **130**(35): p. 11584-11585.
56. He, C., D. Liu, and W. Lin, *Self-Assembled Core–Shell Nanoparticles for Combined Chemotherapy and Photodynamic Therapy of Resistant Head and Neck Cancers.* ACS Nano, 2015. **9**(1): p. 991-1003.
57. Poon, C., et al., *Self-assembled nanoscale coordination polymers carrying oxaliplatin and gemcitabine for synergistic combination therapy of pancreatic cancer.* Journal of Controlled Release, 2015. **201**: p. 90-99.
58. Steinborn, B., et al., *Core-Shell Functionalized Zirconium-Pemetrexed Coordination Nanoparticles as Carriers with a High Drug Content.* Advanced Therapeutics, 2019. **2**(11): p. 1900120.
59. Anderson, S.L. and K.C. Stylianou, *Biologically derived metal organic frameworks.* Coordination Chemistry Reviews, 2017. **349**: p. 102-128.
60. Sarma, D., et al., *Amino Acid Based MOFs: Synthesis, Structure, Single Crystal to Single Crystal Transformation, Magnetic and Related Studies in a Family of Cobalt and Nickel Aminoisophthales.* Inorganic Chemistry, 2009. **48**(24): p. 11660-11676.
61. Yamauchi, O., A. Odani, and M. Takani, *Metal–amino acid chemistry. Weak interactions and related functions of side chain groups.* Journal of the Chemical Society, Dalton Transactions, 2002(18): p. 3411-3421.
62. Pasini, A. and L. Casella, *Some Aspects of Reactivity of Amino-Acids Coordinated to Metal-Ions.* Journal of Inorganic & Nuclear Chemistry, 1974. **36**(9): p. 2133-2144.
63. Imaz, I., et al., *Metal-biomolecule frameworks (MBioFs).* Chem Commun (Camb), 2011. **47**(26): p. 7287-302.
64. Zhang, J.J., et al., *Two 3D supramolecular polymers constructed from an amino acid and a high-nuclear Ln6Cu24 cluster node.* Chemistry, 2004. **10**(16): p. 3963-9.
65. Anokhina, E.V. and A.J. Jacobson, *[Ni2O(L-Asp)(H2O)2)].4H2)O: a homochiral 1D helical chain hybrid compound with extended Ni-O-Ni bonding.* J Am Chem Soc, 2004. **126**(10): p. 3044-5.
66. Black, D., *Formation of bidentate metal chelates from some related pyridine compounds.* Australian Journal of Chemistry, 1967. **20**(10): p. 2101-2107.
67. Anokhina, E.V. and A.J. Jacobson, *[Ni2O(l-Asp)(H2O)2]·4H2O: A Homochiral 1D Helical Chain Hybrid Compound with Extended Ni−O−Ni Bonding.* Journal of the American Chemical Society, 2004. **126**(10): p. 3044-3045.

68. Anokhina, E.V., et al., *Chiral Three-Dimensional Microporous Nickel Aspartate with Extended Ni−O−Ni Bonding.* Journal of the American Chemical Society, 2006. **128**(30): p. 9957-9962.
69. Imai, H., et al., *Three-dimensional chiral molecule-based ferrimagnet with triple-helical-strand structure.* Angew Chem Int Ed Engl, 2004. **43**(42): p. 5618-21.
70. Anokhina, E.V., et al., *Chiral three-dimensional microporous nickel aspartate with extended Ni-O-Ni bonding.* J Am Chem Soc, 2006. **128**(30): p. 9957-62.
71. Shen, C.-J., et al., *Syntheses, structures, and properties of a series of novel high-nuclear 3d–4f clusters with mixed amino acids as ligands: {Ln6Cu24}(Ln = Gd, Tb, Pr and Sm).* Dalton Transactions, 2015. **44**(14): p. 6510-6515.
72. Perez Barrio, J., et al., *Control of porosity geometry in amino acid derived nanoporous materials.* Chemistry, 2008. **14**(15): p. 4521-32.
73. Martí-Gastaldo, C., et al., *Side-chain control of porosity closure in single- and multiple-peptide-based porous materials by cooperative folding.* Nature Chemistry, 2014. **6**(4): p. 343-351.
74. An, J., S.J. Geib, and N.L. Rosi, *Cation-Triggered Drug Release from a Porous Zinc−Adeninate Metal−Organic Framework.* Journal of the American Chemical Society, 2009. **131**(24): p. 8376-8377.
75. Schnitzer, T., et al., *Peptide–Metal Frameworks with Metal Strings Guided by Dispersion Interactions.* Journal of the American Chemical Society, 2021. **143**(2): p. 644-648.
76. Pelley, J.W., *3 - Protein Structure and Function*, in *Elsevier's Integrated Biochemistry*, J.W. Pelley, Editor. 2007, Mosby: Philadelphia. p. 19-28.
77. Liu, Y., W. Xuan, and Y. Cui, *Engineering homochiral metal-organic frameworks for heterogeneous asymmetric catalysis and enantioselective separation.* Adv Mater, 2010. **22**(37): p. 4112-35.
78. Wright, P.A., *Chemistry. Opening the door to peptide-based porous solids.* Science, 2010. **329**(5995): p. 1025-6.
79. Toshio, T., et al., *Structural Analysis of Cadmium–Glycylglycine Complexes Studied by X-Ray Diffraction and High Resolution 113Cd and 13C Solid State NMR.* Bulletin of the Chemical Society of Japan, 1996. **69**(6): p. 1579-1586.
80. Eriko, U., et al., *New Bioactive Zinc(II) Complexes with Peptides and Their Derivatives: Synthesis, Structure, and In Vitro Insulinomimetic Activity.* Bulletin of the Chemical Society of Japan, 2004. **77**(5): p. 981-986.
81. Lee, H.-Y., et al., *Covalent Metal−Peptide Framework Compounds That Extend in One and Two Dimensions.* Crystal Growth & Design, 2008. **8**(1): p. 296-303.
82. Rabone, J., et al., *An Adaptable Peptide-Based Porous Material.* Science, 2010. **329**(5995): p. 1053-1057.
83. Marti-Gastaldo, C., et al., *Enhanced stability in rigid peptide-based porous materials.* Angew Chem Int Ed Engl, 2012. **51**(44): p. 11044-8.
84. Ingleson, M.J., J. Bacsa, and M.J. Rosseinsky, *Homochiral H-bonded proline based metal organic frameworks.* Chemical Communications, 2007(29): p. 3036-3038.

85. Ranford, J.D., et al., *Thermal conversion of a helical coil into a three-dimensional chiral framework.* Angewandte Chemie-International Edition, 1999. **38**(23): p. 3498-3501.
86. Smaldone, R.A., et al., *Metal-organic frameworks from edible natural products.* Angew Chem Int Ed Engl, 2010. **49**(46): p. 8630-4.
87. Zhang, J.J., et al., *Two 3D supramolecular polymers constructed from an amino acid and a high-nuclear Ln(6)Cu(24) cluster node.* Chemistry-a European Journal, 2004. **10**(16): p. 3963-3969.
88. Zhou, T., et al., *Interfacial metal and antibody recognition.* Proceedings of the National Academy of Sciences, 2005. **102**(41): p. 14575-14580.
89. Emsley, J., et al., *Structural basis of collagen recognition by integrin alpha2beta1.* Cell, 2000. **101**(1): p. 47-56.
90. Stillman, M., *Biological Inorganic Chemistry. Structure and Reactivity. Edited by Ivano Bertini, Harry B. Gray, Edward I. Stiefel and Joan S. Valentine.* Angewandte Chemie International Edition, 2007. **46**(46): p. 8741-8742.
91. Salgado, E.N., R.J. Radford, and F.A. Tezcan, *Metal-Directed Protein Self-Assembly.* Accounts of Chemical Research, 2010. **43**(5): p. 661-672.
92. Sontz, P.A., et al., *A Metal Organic Framework with Spherical Protein Nodes: Rational Chemical Design of 3D Protein Crystals.* Journal of the American Chemical Society, 2015. **137**(36): p. 11598-11601.
93. Bailey, J.B., et al., *Synthetic Modularity of Protein–Metal–Organic Frameworks.* Journal of the American Chemical Society, 2017. **139**(24): p. 8160-8166.
94. Imaz, I., et al., *Metal–biomolecule frameworks (MBioFs).* Chemical Communications, 2011. **47**(26): p. 7287-7302.
95. Trávníček, Z., et al., *Preparation and cytotoxic activity of nickel(II) complexes with 6-benzylaminopurine derivatives.* Transition Metal Chemistry, 2002. **27**(8): p. 918-923.
96. Verma, S., A.K. Mishra, and J. Kumar, *The Many Facets of Adenine: Coordination, Crystal Patterns, and Catalysis.* Accounts of Chemical Research, 2010. **43**(1): p. 79-91.
97. Thomas-Gipson, J., et al., *Unravelling the Growth of Supramolecular Metal–Organic Frameworks Based on Metal-Nucleobase Entities.* Crystal Growth & Design, 2015. **15**(2): p. 975-983.
98. Sivakova, S. and S.J. Rowan, *Nucleobases as supramolecular motifs.* Chemical Society Reviews, 2005. **34**(1): p. 9-21.
99. An, J., S.J. Geib, and N.L. Rosi, *High and Selective CO2 Uptake in a Cobalt Adeninate Metal−Organic Framework Exhibiting Pyrimidine- and Amino-Decorated Pores.* Journal of the American Chemical Society, 2010. **132**(1): p. 38-39.
100. Purohit, C.S., A.K. Mishra, and S. Verma, *Four-Stranded Coordination Helices Containing Silver−Adenine (Purine) Metallaquartets.* Inorganic Chemistry, 2007. **46**(21): p. 8493-8495.
101. García-Terán, J.P., et al., *An Unusual 3D Coordination Polymer Based on Bridging Interactions of the Nucleobase Adenine.* Inorganic Chemistry, 2004. **43**(15): p. 4549-4551.
102. Zhuang, J., A.P. Young, and C.-K. Tsung, *Integration of Biomolecules with Metal–Organic Frameworks.* Small, 2017. **13**(32): p. 1700880.

103. Wang, S., et al., *DNA-Functionalized Metal–Organic Framework Nanoparticles for Intracellular Delivery of Proteins.* Journal of the American Chemical Society, 2019. **141**(6): p. 2215-2219.
104. Kahn, J.S., et al., *Stimuli-Responsive DNA-Functionalized Metal–Organic Frameworks (MOFs).* Advanced Materials, 2017. **29**(6): p. 1602782.
105. Wei, X., et al., *Fluorescence biosensor for the H(5)N(1) antibody based on a metal-organic framework platform.* J Mater Chem B, 2013. **1**(13): p. 1812-1817.
106. Chen, L., et al., *Metal-organic frameworks-based biosensor for sequence-specific recognition of double-stranded DNA.* Analyst, 2013. **138**(12): p. 3490-3.
107. Ye, T., et al., *Metal-organic framework-based molecular beacons for multiplexed DNA detection by synchronous fluorescence analysis.* Analyst, 2014. **139**(7): p. 1721-5.
108. Wu, Y., et al., *Nano metal–organic framework (NMOF)-based strategies for multiplexed microRNA detection in solution and living cancer cells.* Nanoscale, 2015. **7**(5): p. 1753-1759.
109. Winarta, J., et al., *A Decade of UiO-66 Research: A Historic Review of Dynamic Structure, Synthesis Mechanisms, and Characterization Techniques of an Archetypal Metal–Organic Framework.* Crystal Growth & Design, 2020. **20**(2): p. 1347-1362.
110. DeStefano, M.R., et al., *Room-Temperature Synthesis of UiO-66 and Thermal Modulation of Densities of Defect Sites.* Chemistry of Materials, 2017. **29**(3): p. 1357-1361.
111. Smaldone, R.A., et al., *Metal–Organic Frameworks from Edible Natural Products.* Angewandte Chemie International Edition, 2010. **49**(46): p. 8630-8634.
112. Abrahams, B.F., et al., *Channel-containing lanthanide mucate structures.* CrystEngComm, 2003. **5**(55): p. 313-317.
113. Abrahams, B.F., et al., *Zinc Saccharate: A Robust, 3D Coordination Network with Two Types of Isolated, Parallel Channels, One Hydrophilic and the Other Hydrophobic.* Angewandte Chemie International Edition, 2003. **42**(16): p. 1848-1851.
114. Rao, C.N.R., S. Natarajan, and R. Vaidhyanathan, *Metal Carboxylates with Open Architectures.* Angewandte Chemie International Edition, 2004. **43**(12): p. 1466-1496.
115. Dybtsev, D.N., et al., *Microporous Manganese Formate: A Simple Metal−Organic Porous Material with High Framework Stability and Highly Selective Gas Sorption Properties.* Journal of the American Chemical Society, 2004. **126**(1): p. 32-33.
116. Forster, P.M. and A.K. Cheetham, *Open-Framework Nickel Succinate, [Ni7(C4H4O4)6(OH)2(H2O)2]·2 H2O: A New Hybrid Material with Three-Dimensional Ni−O−Ni Connectivity.* Angewandte Chemie International Edition, 2002. **41**(3): p. 457-459.
117. Serre, C., et al., *A Route to the Synthesis of Trivalent Transition-Metal Porous Carboxylates with Trimeric Secondary Building Units.* Angewandte Chemie International Edition, 2004. **43**(46): p. 6285-6289.
118. Thushari, S., et al., *Microporous chiral metal coordination polymers: hydrothermal synthesis, channel engineering and stability of lanthanide tartrates.* Chemical Communications, 2005(44): p. 5515-5517.

119. Crick, F., *Central dogma of molecular biology.* Nature, 1970. **227**(5258): p. 561-3.
120. Minchin, S. and J. Lodge, *Understanding biochemistry: structure and function of nucleic acids.* Essays Biochem, 2019. **63**(4): p. 433-456.
121. Tatiparti, K., et al., *siRNA Delivery Strategies: A Comprehensive Review of Recent Developments.* Nanomaterials, 2017. **7**(4): p. 77.
122. Sana, J., et al., *Novel classes of non-coding RNAs and cancer.* Journal of Translational Medicine, 2012. **10**(1): p. 103.
123. He, L. and G.J. Hannon, *MicroRNAs: small RNAs with a big role in gene regulation.* Nature Reviews Genetics, 2004. **5**(7): p. 522-531.
124. Nissen, P., et al., *The structural basis of ribosome activity in peptide bond synthesis.* Science, 2000. **289**(5481): p. 920-30.
125. Friedmann, T. and R. Roblin, *Gene Therapy for Human Genetic Disease?* Science, 1972. **175**(4025): p. 949-955.
126. Lächelt, U. and E. Wagner, *Nucleic Acid Therapeutics Using Polyplexes: A Journey of 50 Years (and Beyond).* Chemical Reviews, 2015. **115**(19): p. 11043-11078.
127. Opalinska, J.B. and A.M. Gewirtz, *Nucleic-acid therapeutics: basic principles and recent applications.* Nature Reviews Drug Discovery, 2002. **1**(7): p. 503-514.
128. Kulkarni, J.A., et al., *The current landscape of nucleic acid therapeutics.* Nature Nanotechnology, 2021. **16**(6): p. 630-643.
129. Wagner, E., *Biomaterials in RNAi therapeutics: quo vadis?* Biomaterials Science, 2013. **1**(8): p. 804-809.
130. Jeong, J.H., et al., *siRNA Conjugate Delivery Systems.* Bioconjugate Chemistry, 2009. **20**(1): p. 5-14.
131. Wagner, E., *Polymers for siRNA Delivery: Inspired by Viruses to be Targeted, Dynamic, and Precise.* Accounts of Chemical Research, 2012. **45**(7): p. 1005-1013.
132. Li, W. and F.C. Szoka, *Lipid-based Nanoparticles for Nucleic Acid Delivery.* Pharmaceutical Research, 2007. **24**(3): p. 438-449.
133. Terheggen, H.G., et al., *Unsuccessful trial of gene replacement in arginase deficiency.* Z Kinderheilkd, 1975. **119**(1): p. 1-3.
134. Kohn, D.B., et al., *Establishment and characterization of adenosine deaminase-deficient human T cell lines.* The Journal of Immunology, 1989. **142**(11): p. 3971-3977.
135. Zhao, Z., A.C. Anselmo, and S. Mitragotri, *Viral vector-based gene therapies in the clinic.* Bioeng Transl Med, 2022. **7**(1): p. e10258.
136. Lundstrom, K., *Viral Vectors in Gene Therapy.* Diseases, 2018. **6**(2): p. 42.
137. Bulcha, J.T., et al., *Viral vector platforms within the gene therapy landscape.* Signal Transduction and Targeted Therapy, 2021. **6**(1): p. 53.
138. Pack, D.W., et al., *Design and development of polymers for gene delivery.* Nat Rev Drug Discov, 2005. **4**(7): p. 581-93.
139. Yin, H., et al., *Non-viral vectors for gene-based therapy.* Nature Reviews Genetics, 2014. **15**(8): p. 541-555.
140. Wang, D., P.W.L. Tai, and G. Gao, *Adeno-associated virus vector as a platform for gene therapy delivery.* Nature Reviews Drug Discovery, 2019. **18**(5): p. 358-378.

141. Rose, J.A., M.D. Hoggan, and A.J. Shatkin, *Nucleic acid from an adeno-associated virus: chemical and physical studies.* Proceedings of the National Academy of Sciences, 1966. **56**(1): p. 86-92.
142. Naso, M.F., et al., *Adeno-Associated Virus (AAV) as a Vector for Gene Therapy.* BioDrugs, 2017. **31**(4): p. 317-334.
143. Villiger, L., et al., *Treatment of a metabolic liver disease by in vivo genome base editing in adult mice.* Nature Medicine, 2018. **24**(10): p. 1519-1525.
144. Wu, Z., H. Yang, and P. Colosi, *Effect of genome size on AAV vector packaging.* Mol Ther, 2010. **18**(1): p. 80-6.
145. Russell, S., et al., *Efficacy and safety of voretigene neparvovec (AAV2-hRPE65v2) in patients with RPE65-mediated inherited retinal dystrophy: a randomised, controlled, open-label, phase 3 trial.* The Lancet, 2017. **390**(10097): p. 849-860.
146. Rinaldi, C. and M.J.A. Wood, *Antisense oligonucleotides: the next frontier for treatment of neurological disorders.* Nature Reviews Neurology, 2018. **14**(1): p. 9-21.
147. Hammond, S.M., et al., *An RNA-directed nuclease mediates post-transcriptional gene silencing in Drosophila cells.* Nature, 2000. **404**(6775): p. 293-296.
148. Dias, N. and C.A. Stein, *Antisense Oligonucleotides: Basic Concepts and Mechanisms.* Molecular Cancer Therapeutics, 2002. **1**(5): p. 347-355.
149. Doench, J.G. and P.A. Sharp, *Specificity of microRNA target selection in translational repression.* Genes Dev, 2004. **18**(5): p. 504-11.
150. *The Clearance and Degradation of Oligodeoxynucleotides Following Intravenous Injection into Rabbits.* Antisense Research and Development, 1991. **1**(2): p. 153-160.
151. Manoharan, M., *2'-carbohydrate modifications in antisense oligonucleotide therapy: importance of conformation, configuration and conjugation.* Biochim Biophys Acta, 1999. **1489**(1): p. 117-30.
152. *Cholesterol–GalNAc Dual Conjugation Strategy for Reducing Renal Distribution of Antisense Oligonucleotides.* Nucleic Acid Therapeutics, 2018. **28**(1): p. 50-57.
153. Schreiber, A., et al., *Antiviral treatment of cytomegalovirus infection and resistant strains.* Expert Opin Pharmacother, 2009. **10**(2): p. 191-209.
154. Azad, R.F., et al., *Antiviral activity of a phosphorothioate oligonucleotide complementary to RNA of the human cytomegalovirus major immediate-early region.* Antimicrobial Agents and Chemotherapy, 1993. **37**(9): p. 1945-1954.
155. Dana, H., et al., *Molecular Mechanisms and Biological Functions of siRNA.* Int J Biomed Sci, 2017. **13**(2): p. 48-57.
156. Hannon, G.J., *RNA interference.* Nature, 2002. **418**(6894): p. 244-251.
157. Nair, J.K., et al., *Multivalent N-Acetylgalactosamine-Conjugated siRNA Localizes in Hepatocytes and Elicits Robust RNAi-Mediated Gene Silencing.* Journal of the American Chemical Society, 2014. **136**(49): p. 16958-16961.
158. Stockert, R.J., *The asialoglycoprotein receptor: relationships between structure, function, and expression.* Physiol Rev, 1995. **75**(3): p. 591-609.
159. Willoughby, J.L.S., et al., *Evaluation of GalNAc-siRNA Conjugate Activity in Pre-clinical Animal Models with Reduced Asialoglycoprotein Receptor Expression.* Molecular Therapy, 2018. **26**(1): p. 105-114.

160. *GalNAc-siRNA Conjugates: Leading the Way for Delivery of RNAi Therapeutics.* Nucleic Acid Therapeutics, 2018. **28**(3): p. 109-118.
161. Scott, L.J., *Givosiran: First Approval.* Drugs, 2020. **80**(3): p. 335-339.
162. Tenchov, R., et al., *Lipid Nanoparticles─From Liposomes to mRNA Vaccine Delivery, a Landscape of Research Diversity and Advancement.* ACS Nano, 2021. **15**(11): p. 16982-17015.
163. Felgner, P.L., et al., *Lipofection: a highly efficient, lipid-mediated DNA-transfection procedure.* Proceedings of the National Academy of Sciences, 1987. **84**(21): p. 7413-7417.
164. Haider, M., et al., *Nanostructured Lipid Carriers for Delivery of Chemotherapeutics: A Review.* Pharmaceutics, 2020. **12**(3): p. 288.
165. Müller, R.H., K. Mäder, and S. Gohla, *Solid lipid nanoparticles (SLN) for controlled drug delivery – a review of the state of the art.* European Journal of Pharmaceutics and Biopharmaceutics, 2000. **50**(1): p. 161-177.
166. Hajj, K.A., et al., *Branched-Tail Lipid Nanoparticles Potently Deliver mRNA In Vivo due to Enhanced Ionization at Endosomal pH.* Small, 2019. **15**(6): p. 1805097.
167. Gabizon, A., et al., *Systemic administration of doxorubicin-containing liposomes in cancer patients: a phase I study.* Eur J Cancer Clin Oncol, 1989. **25**(12): p. 1795-803.
168. Torchilin, V.P., *Liposomes as targetable drug carriers.* Critical reviews in therapeutic drug carrier systems, 1985. **2**(1): p. 65-115.
169. Deshpande, P.P., S. Biswas, and V.P. Torchilin, *Current trends in the use of liposomes for tumor targeting.* Nanomedicine, 2013. **8**(9): p. 1509-1528.
170. Davis, F.F., *The origin of pegnology.* Advanced Drug Delivery Reviews, 2002. **54**(4): p. 457-458.
171. Hassan, S., et al., *Evolution and clinical translation of drug delivery nanomaterials.* Nano Today, 2017. **15**: p. 91-106.
172. Andresen, T.L., S.S. Jensen, and K. Jørgensen, *Advanced strategies in liposomal cancer therapy: Problems and prospects of active and tumor specific drug release.* Progress in Lipid Research, 2005. **44**(1): p. 68-97.
173. Rahim, M.A., et al., *Recent Advancements in Stimuli Responsive Drug Delivery Platforms for Active and Passive Cancer Targeting.* Cancers, 2021. **13**(4): p. 670.
174. Yatvin, M.B., et al., *<i>p</i>H-Sensitive Liposomes: Possible Clinical Implications.* Science, 1980. **210**(4475): p. 1253-1255.
175. Jayaraman, M., et al., *Maximizing the Potency of siRNA Lipid Nanoparticles for Hepatic Gene Silencing In Vivo**.* Angewandte Chemie International Edition, 2012. **51**(34): p. 8529-8533.
176. Food and D. Administration, *Emergency Use Authorization (EUA) of the Pfizer-BioNTech COVID-19 vaccine to prevent coronavirus disease 2019 (COVID-19).* Food and Drug Administration, Silver Spring, MS, USA, 2019.
177. Food, U. and D. Administration, *Emergency use authorization (EUA) of the Moderna COVID-19 vaccine to prevent coronavirus disease 2019 (COVID-19): fact sheet for healthcare providers administering vaccine*. 2021.
178. Cross, R., *Without these lipid shells, there would be no mRNA vaccines for COVID-19.* Chem Eng News, 2021. **99**(8): p. 144.

179. Hou, X., et al., *Lipid nanoparticles for mRNA delivery.* Nature Reviews Materials, 2021. **6**(12): p. 1078-1094.
180. Freitag, F. and E. Wagner, *Optimizing synthetic nucleic acid and protein nanocarriers: The chemical evolution approach.* Advanced Drug Delivery Reviews, 2021. **168**: p. 30-54.
181. Bloomfield, V.A., *DNA condensation by multivalent cations.* Biopolymers, 1997. **44**(3): p. 269-82.
182. Felgner, P.L., et al., *Nomenclature for synthetic gene delivery systems.* Hum Gene Ther, 1997. **8**(5): p. 511-2.
183. Bloomfield, V.A., *Condensation of DNA by multivalent cations: Considerations on mechanism.* Biopolymers, 1991. **31**(13): p. 1471-1481.
184. Uzgün, S., et al., *PEGylation improves nanoparticle formation and transfection efficiency of messenger RNA.* Pharm Res, 2011. **28**(9): p. 2223-32.
185. Mislick, K.A. and J.D. Baldeschwieler, *Evidence for the role of proteoglycans in cation-mediated gene transfer.* Proc Natl Acad Sci U S A, 1996. **93**(22): p. 12349-54.
186. Suk, J.S., et al., *PEGylation as a strategy for improving nanoparticle-based drug and gene delivery.* Adv Drug Deliv Rev, 2016. **99**(Pt A): p. 28-51.
187. Tockary, T.A., et al., *Rod-to-Globule Transition of pDNA/PEG–Poly(l-Lysine) Polyplex Micelles Induced by a Collapsed Balance Between DNA Rigidity and PEG Crowdedness.* Small, 2016. **12**(9): p. 1193-1200.
188. Vasiliu, T., et al., *In silico study of PEI-PEG-squalene-dsDNA polyplex formation: the delicate role of the PEG length in the binding of PEI to DNA.* Biomater Sci, 2021. **9**(19): p. 6623-6640.
189. Grun, M.K., et al., *PEGylation of poly(amine-co-ester) polyplexes for tunable gene delivery.* Biomaterials, 2021. **272**: p. 120780.
190. Vetter, V.C. and E. Wagner, *Targeting nucleic acid-based therapeutics to tumors: Challenges and strategies for polyplexes.* J Control Release, 2022. **346**: p. 110-135.
191. Schilb, A.L., et al., *Efficacy of Targeted ECO/miR-200c Nanoparticles for Modulating Tumor Microenvironment and Treating Triple Negative Breast Cancer as Non-invasively Monitored by MR Molecular Imaging.* Pharm Res, 2021. **38**(8): p. 1405-1418.
192. Vaidya, A.M., et al., *Systemic Delivery of Tumor-Targeting siRNA Nanoparticles against an Oncogenic LncRNA Facilitates Effective Triple-Negative Breast Cancer Therapy.* Bioconjug Chem, 2019. **30**(3): p. 907-919.
193. Oba, M., et al., *Cyclic RGD peptide-conjugated polyplex micelles as a targetable gene delivery system directed to cells possessing alphavbeta3 and alphavbeta5 integrins.* Bioconjug Chem, 2007. **18**(5): p. 1415-23.
194. Lei, Y., et al., *Glutathione-sensitive RGD-poly(ethylene glycol)-SS-polyethylenimine for intracranial glioblastoma targeted gene delivery.* J Gene Med, 2013. **15**(8-9): p. 291-305.
195. Dohmen, C., et al., *Nanosized multifunctional polyplexes for receptor-mediated siRNA delivery.* ACS Nano, 2012. **6**(6): p. 5198-208.
196. Benli-Hoppe, T., et al., *Transferrin Receptor Targeted Polyplexes Completely Comprised of Sequence-Defined Components.* Macromol Rapid Commun, 2022. **43**(12): p. e2100602.

197. Boussif, O., et al., *A versatile vector for gene and oligonucleotide transfer into cells in culture and in vivo: polyethylenimine.* Proc Natl Acad Sci U S A, 1995. **92**(16): p. 7297-301.
198. Itaka, K., et al., *In situ single cell observation by fluorescence resonance energy transfer reveals fast intra-cytoplasmic delivery and easy release of plasmid DNA complexed with linear polyethylenimine.* J Gene Med, 2004. **6**(1): p. 76-84.
199. Nielsen, P.E., et al., *Sequence-Selective Recognition of DNA by Strand Displacement with a Thymine-Substituted Polyamide.* Science, 1991. **254**(5037): p. 1497-1500.
200. Egholm, M., et al., *PNA hybridizes to complementary oligonucleotides obeying the Watson–Crick hydrogen-bonding rules.* Nature, 1993. **365**(6446): p. 566-568.
201. Wittung, P., et al., *DNA-like double helix formed by peptide nucleic acid.* Nature, 1994. **368**(6471): p. 561-563.
202. Demidov, V., et al., *Sequence selective double strand DNA cleavage by Peptide Nucleic Acid (PNA) targeting using nuclease S1.* Nucleic Acids Research, 1993. **21**(9): p. 2103-2107.
203. Hejazi , M.S., et al., *Development of a Novel Electrochemical Biosensor for Detection and Discrimination of DNA Sequence and Single Base Mutation in dsDNA Samples Based on PNA-dsDNA Hybridization – a new Platform Technology.* Electroanalysis, 2011. **23**(2): p. 503-511.
204. Nielsen, P.E. and G. Haaima, *Peptide nucleic acid (PNA). A DNA mimic with a pseudopeptide backbone.* Chemical Society Reviews, 1997. **26**(2): p. 73-78.
205. Nielsen, P.E., *Peptide nucleic acid: a versatile tool in genetic diagnostics and molecular biology.* Current Opinion in Biotechnology, 2001. **12**(1): p. 16-20.
206. Stender, H., B. Williams, and J. Coull, *PNA fluorescent in situ hybridization (FISH) for rapid microbiology and cytogenetic analysis.* Methods Mol Biol, 2014. **1050**: p. 167-78.
207. Fiandaca, M.J., et al., *Self-reporting PNA/DNA primers for PCR analysis.* Genome Res, 2001. **11**(4): p. 609-13.
208. Pellestor, F. and P. Paulasova, *The peptide nucleic acids (PNAs), powerful tools for molecular genetics and cytogenetics.* European Journal of Human Genetics, 2004. **12**(9): p. 694-700.
209. El-Andaloussi, S., et al., *Induction of splice correction by cell-penetrating peptide nucleic acids.* The Journal of Gene Medicine, 2006. **8**(10): p. 1262-1273.
210. Abes, S., et al., *Peptide-based delivery of nucleic acids: design, mechanism of uptake and applications to splice-correcting oligonucleotides.* Biochemical Society Transactions, 2007. **35**(1): p. 53-55.
211. Imamura, Y., et al., *A Peptide Nucleic Acid to Reduce Type I Collagen Production by Fibroblast Cells.* Open Journal of Medicinal Chemistry, 2015. **Vol.05No.01**: p. 8.
212. Babar, I.A., et al., *Nanoparticle-based therapy in an in vivo microRNA-155 (miR-155)-dependent mouse model of lymphoma.* Proceedings of the National Academy of Sciences, 2012. **109**(26): p. E1695-E1704.

213. Abes, S., et al., *Efficient splicing correction by PNA conjugation to an R6-Penetratin delivery peptide.* Nucleic Acids Research, 2007. **35**(13): p. 4495-4502.
214. Kang, S.-H., M.-J. Cho, and R. Kole, *Up-Regulation of Luciferase Gene Expression with Antisense Oligonucleotides: Implications and Applications in Functional Assay Development.* Biochemistry, 1998. **37**(18): p. 6235-6239.
215. Koppelhus, U. and P.E. Nielsen, *Cellular delivery of peptide nucleic acid (PNA).* Advanced Drug Delivery Reviews, 2003. **55**(2): p. 267-280.
216. Kaihatsu, K., K.E. Huffman, and D.R. Corey, *Intracellular Uptake and Inhibition of Gene Expression by PNAs and PNA−Peptide Conjugates.* Biochemistry, 2004. **43**(45): p. 14340-14347.
217. Janowski, B.A., et al., *Inhibiting transcription of chromosomal DNA with antigene peptide nucleic acids.* Nature Chemical Biology, 2005. **1**(4): p. 210-215.
218. Saarbach, J., P.M. Sabale, and N. Winssinger, *Peptide nucleic acid (PNA) and its applications in chemical biology, diagnostics, and therapeutics.* Curr Opin Chem Biol, 2019. **52**: p. 112-124.
219. Kuhn, J., et al., *Supramolecular Assembly of Aminoethylene-Lipopeptide PMO Conjugates into RNA Splice-Switching Nanomicelles.* Advanced Functional Materials, 2019. **29**(48): p. 1906432.
220. Totsingan, F., R. Marchelli, and R. Corradini, *Molecular computing by PNA:PNA duplex formation.* Artif DNA PNA XNA, 2011. **2**(1): p. 16-22.
221. Wittung, P., P. Nielsen, and B. Nordén, *Observation of a PNA−PNA−PNA Triplex.* Journal of the American Chemical Society, 1997. **119**(13): p. 3189-3190.
222. Hirschle, P., et al., *Exploration of MOF nanoparticle sizes using various physical characterization methods – is what you measure what you get?* CrystEngComm, 2016. **18**(23): p. 4359-4368.
223. Kuhn, H., et al., *Kinetic sequence discrimination of cationic bis-PNAs upon targeting of double-stranded DNA.* Nucleic Acids Research, 1998. **26**(2): p. 582-587.
224. Tomac, S., et al., *Ionic Effects on the Stability and Conformation of Peptide Nucleic Acid Complexes.* Journal of the American Chemical Society, 1996. **118**(24): p. 5544-5552.
225. Bagherzadeh, E., S.M. Zebarjad, and H.R.M. Hosseini, *Morphology Modification of the Iron Fumarate MIL-88A Metal–Organic Framework Using Formic Acid and Acetic Acid as Modulators.* European Journal of Inorganic Chemistry, 2018. **2018**(18): p. 1909-1915.
226. Schaate, A., et al., *Modulated Synthesis of Zr-Based Metal–Organic Frameworks: From Nano to Single Crystals.* Chemistry – A European Journal, 2011. **17**(24): p. 6643-6651.
227. Stock, N. and S. Biswas, *Synthesis of Metal-Organic Frameworks (MOFs): Routes to Various MOF Topologies, Morphologies, and Composites.* Chemical Reviews, 2012. **112**(2): p. 933-969.
228. Huxford-Phillips, R.C., et al., *Lipid-coated nanoscale coordination polymers for targeted cisplatin delivery.* RSC Advances, 2013. **3**(34): p. 14438-14443.
229. Peng, Y., et al., *Nanoscale Copper(II)–Diethyldithiocarbamate Coordination Polymer as a Drug Self-Delivery System for Highly Robust*

and Specific Cancer Therapy. Molecular Pharmaceutics, 2020. **17**(8): p. 2864-2873.

230. Shen, S., et al., *Versatile hyaluronic acid modified AQ4N-Cu(II)-gossypol infinite coordination polymer nanoparticles: Multiple tumor targeting, highly efficient synergistic chemotherapy, and real-time self-monitoring.* Biomaterials, 2018. **154**: p. 197-212.
231. Brunauer, S., P.H. Emmett, and E. Teller, *Adsorption of Gases in Multimolecular Layers.* Journal of the American Chemical Society, 1938. **60**(2): p. 309-319.
232. Ambroz, F., et al., *Evaluation of the BET Theory for the Characterization of Meso and Microporous MOFs.* Small Methods, 2018. **2**(11): p. 1800173.
233. Wu, S.-T., *A Rigorous Justification of the Point B Method for Determination of Monolayer Capacity from a Type II Adsorption Isotherm.* Progress of Theoretical Physics, 1975. **53**(1): p. 21-40.
234. Cavka, J.H., et al., *A New Zirconium Inorganic Building Brick Forming Metal Organic Frameworks with Exceptional Stability.* Journal of the American Chemical Society, 2008. **130**(42): p. 13850-13851.
235. Cabantchik, Z.I., et al., *A Fluorescence Assay for Assessing Chelation of Intracellular Iron in a Membrane Model System and in Mammalian Cells.* Analytical Biochemistry, 1996. **233**(2): p. 221-227.
236. Sato, S., et al., *Single-cell lineage tracking analysis reveals that an established cell line comprises putative cancer stem cells and their heterogeneous progeny.* Sci Rep, 2016. **6**: p. 23328.
237. Bansal, V.K., *Serum Inorganic Phosphorus*, in *Clinical Methods: The History, Physical, and Laboratory Examinations*, H.K. Walker, W.D. Hall, and J.W. Hurst, Editors. 1990, Butterworths. Copyright © 1990, Butterworth Publishers, a division of Reed Publishing.: Boston.

238. Hall, A., et al., *Polyplex Evolution: Understanding Biology, Optimizing Performance.* Molecular Therapy, 2017. **25**(7): p. 1476-1490.
239. Lv, H., et al., *Toxicity of cationic lipids and cationic polymers in gene delivery.* J Control Release, 2006. **114**(1): p. 100-9.
240. Mintzer, M.A. and E.E. Simanek, *Nonviral vectors for gene delivery.* Chem Rev, 2009. **109**(2): p. 259-302.
241. Kilchrist, K.V., et al., *Gal8 Visualization of Endosome Disruption Predicts Carrier-Mediated Biologic Drug Intracellular Bioavailability.* ACS Nano, 2019. **13**(2): p. 1136-1152.

7. Publications

Original articles

Berger, S., Krhač Levačić, A., Hörterer, E., Wilk, U., Benli-Hoppe, T., Wang, Y., **Öztürk, Ö**., Luo, J., Wagner, E. Optimizing pDNA lipo-polyplexes: A balancing act between stability and cargo release. Biomacromolecules. 2021 Mar 8;22(3):1282-1296.

Benli-Hoppe T, Göl Öztürk Ş, **Öztürk Ö**, Berger S, Wagner E, Yazdi M. Transferrin Receptor Targeted Polyplexes Completely Comprised of Sequence-Defined Components, *Macromol Rapid Commun*. 2021 Oct 29:e2100602.

Spellerberg R., Benli-Hoppe T., Kitzberger C., Hageneier M., Schwenk N., **Öztürk Ö.,** Steiger K., Multhoff G., Eiber M., Schilling F., Weber W., Kälin R., Glass R., Nelson P., Wagner E., Spitzweg, C. Dual EGFR- and TfR-targeted Gene Transfer Improves Efficacy of Sodium Iodide Symporter (NIS) Gene Therapy of Glioblastoma. Molecular Therapy – Oncolytics. 2022 (Accepted Manuscript).

Manuscripts in preparation

Öztürk Ö., Lessl A., Höhn M., Wuttke S., Nielsen P., Wagner E., Lächelt, U., Peptide Nucleic Acid – Zirconium Coordination Nanoparticles. Manuscript to be submitted.

8. Acknowledgements

After more than 4 years, my Ph.D. study finally comes to end. It was an unforgettable experience for me. I learnt so much both scientifically and otherwise. Several people contributed to this thesis either directly by collaboration or indirectly by supporting in my personal life. I would like to express my sincere gratitude towards all the people who had supported me.

First of all, I would like to thank Prof. Dr. Ernst Wagner for giving me the opportunity to work in his research group. I am deeply grateful for his wise and careful guidance counsel and sympathetic support and during my Ph.D. I highly appreciate the received trust, guidance, and all the feedback which developed me as scientist.

I also owe simply a lot to Ass. Prof. Dr. Ulrich Lächelt. Foremost I would like to thank him for being excellent mentor for me. Supervision, numerous discussion and good advice I received from him made this work possible. I am so grateful to him for creating a great atmosphere, and baking my scientific sense.

I would like to thank of YLSY fellowships granted by Turkish Ministry of Education for the tremendous economic support to my Ph.D. studies at Ludwig-Maximilians-Universität Munich. I also want to thank General Consul of Turkish Republic Mehmet Günay and Education Attaché Prof. Dr. Mustafa Çakır for their support.

Additionally, I would like to thank Prof. Dr. Stefan Wuttke and Prof. Dr. Peter E. Nielsen for fruitful discussions their feedback helped me a lot and provide new perspectives.

I am also grateful to all my colleagues for their collaborations. I would like to thank Miriam Höhn for her contribution on the thesis with confocal microscopy. I thank Şurhan Göl for great help in cell culture. Many thanks to Anna-Lina Lessl for providing PMO and LP Len A. I also want to thank Steffen Schmidt for SEM measurements. Thanks to Teoman Benli-Hoppe, Simone Berger and Tobias Burghardt M mass spectrometry measurements. Many thanks to Lächelt subgroup members current and old, Benjamin Steinborn, Jasmin Kuhn, Yi Lin and Faqian Shen. Finally, to Wolfgang Rödl for repairing any equipment, Melinda Kiss and Markus Kovac for keeping the everyday life in the lab running and Olga Brück for her organization skills.

Son olarak, beni dünyaya getiren, büyüten ve yetiştiren annem Aynur ve babam Cengiz’e, birlikte büyüdüğüm dünyalar tatlısı kardeşim Elif`e ve beni hem hayatsal hem bilimsel konularda her zaman destekleyen, daima yanımda olan biricik eşim Şurhan’a binlerce kez teşekkür etmek isterim.

Teşekkürler!